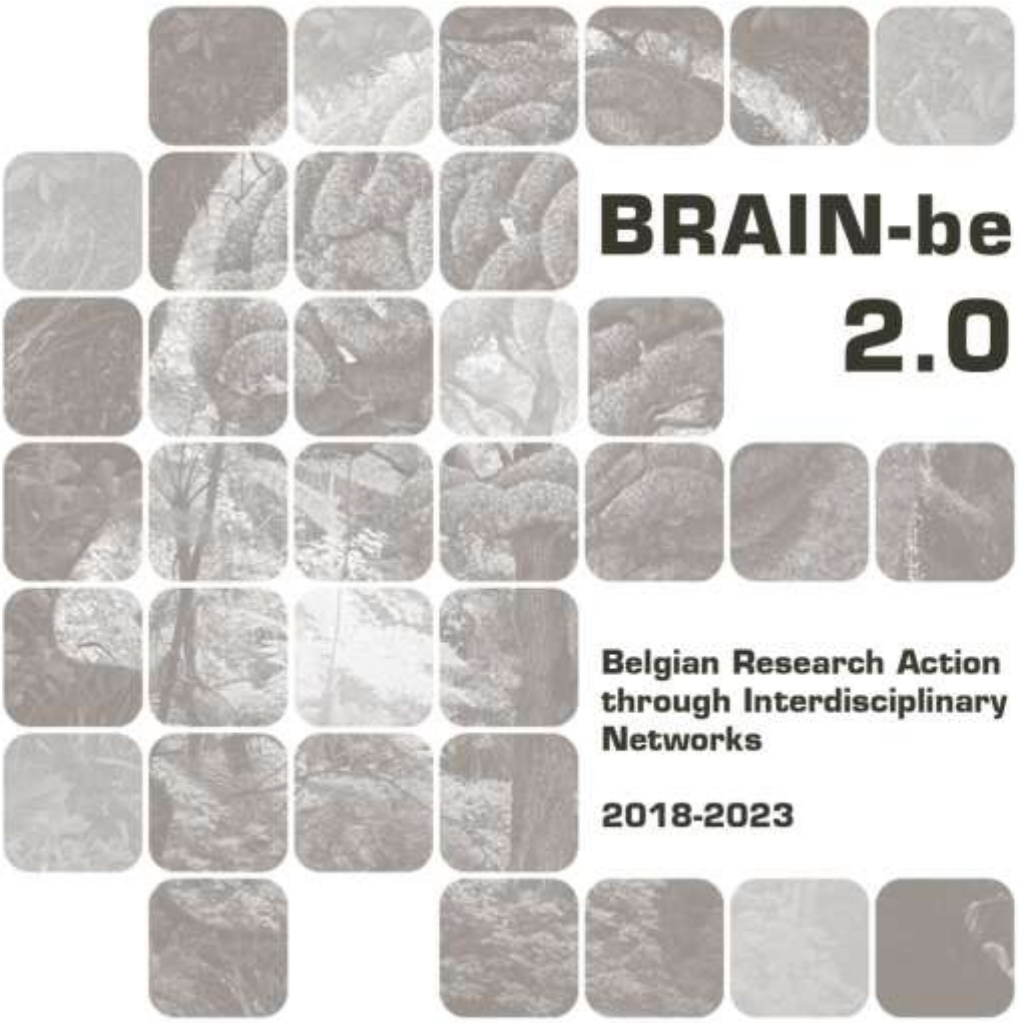

EQUATOR

Emission Quantification of Atmospheric tracers in the Tropics using ObseRvations from satellites

OPACKA BEATA (BIRA-IASB) – STAVRAKOU TRISSEVGENI (BIRA-IASB) – MÜLLER JEAN-FRANÇOIS (BIRA-IASB)

Pillar 1: Challenges and knowledge of the living and non-living world

belspo .be

NETWORK PROJECT

EQUATOR
Emission Quantification of Atmospheric tracers in the Tropics using ObseRvations from satellites

Contract - B2/202/P1/EQUATOR

FINAL REPORT

PROMOTORS: STAVRAKOU TRISSEVGENI (BIRA-IASB) ...

AUTHORS: OPACKA BEATA (BIRA-IASB)
STAVRAKOU TRISSEVGENI (BIRA-IASB)
MÜLLER JEAN-FRANÇOIS (BIRA-IASB)

Published in 2025 by the Belgian Science Policy Office
WTCIII
Simon Bolivarlaan 30 bus 7
Boulevard Simon Bolivar 30 bte 7
B-1000 Brussels
Belgium
Tel: +32 (0)2 238 34 11
http://www.belspo.be
http://www.belspo.be/brain-be

Contact person: Trissevgeni STAVRAKOU
Tel: +32 (0)2 373 67 66

Opacka, B., T. Stavrakou, and J.-F. Müller. ***Emission quantification of atmospheric traces in the Tropics using observations from satellites (EQUATOR)***. Final Report. Brussels: Belgian Science Policy Office 2025 – 71 p. (BRAIN-be 2.0 - (Belgian Research Action through Interdisciplinary Networks)), 2025.

TABLE OF CONTENTS

ABSTRACT 5
1. INTRODUCTION 6
2. STATE OF THE ART AND OBJECTIVES 8
3. METHODOLOGY 10
3.1. BOTTOM-UP BVOCS BASED ON SATELLITE-BASED LCC DATA 10
3.2. CHARACTERISATION OF BIASES IN SATELLITE OBSERVATIONS 12
3.3. TOP-DOWN INVENTORIES OF VOC AND NO_X USING JOINT INVERSION 14
4. SCIENTIFIC RESULTS AND RECOMMENDATIONS 20
4.1. BOTTOM-UP BIOGENIC EMISSION FLUXES ACCOUNTING FOR LAND COVER CHANGES (WP1) 20
4.2. SPACE-BASED VOC EMISSIONS USING OMI HCHO DATA (WP3) 28
4.3. TOP-DOWN INVENTORIES OF VOC AND NO_X IN THE TROPICS (WP 2 & 4) 33
5. DISSEMINATION AND VALORISATION 54
5.1. PHD THESIS 54
5.2. WEBSITES 54
5.3. MEETINGS, WORKSHOPS AND CONFERENCES 54
5.4. DATASETS 56
5.5. OUTREACH 56
6. PUBLICATIONS 58
7. ACKNOWLEDGEMENTS 59
REFERENCES 59
ANNEXES 73

ABSTRACT

Biogenic volatile organic compounds (BVOCs), especially isoprene, play a central role by influencing atmospheric composition and chemistry by contributing to the formation of secondary organic aerosols and influencing tropospheric hydroxyl radical level through depletion or regeneration, thereby altering the oxidative capacity of the atmosphere and the lifetime of methane. Despite their importance, isoprene emissions remain highly uncertain, especially in tropical regions, due to complex biosphere–atmosphere interactions, limited observational constraints, and poorly constrained nitrogen oxides ($NO_X \equiv NO + NO_2$) levels. The EQUATOR project aims to improve the quantification and understanding of isoprene and NO_X emissions, with a focus on the tropics, by combining bottom-up and top-down modelling approaches. Specific objectives include the derivation of a bottom-up isoprene emission inventory using the state-of-the art MEGAN model based on time-dependent, satellite-based land cover maps to assess the impact of vegetation distribution uncertainties on isoprene fluxes and trends. Another key component of the project involves the characterisation of systematic biases in OMI formaldehyde (HCHO) satellite retrievals using independent ground-based and airborne observations. Furthermore, EQUATOR implements a novel two-species inversion framework that simultaneously constrains VOC and NO_X emissions over Africa and South America using TROPOMI HCHO and NO_2 data within the MAGRITTEv1.1 chemistry-transport model and its adjoint to account for coupled NO_x and VOC feedbacks. The study delivers top-down estimates of natural NO_X sources, including soil and lightning emissions, and isoprene emission, and evaluates their robustness through sensitivity analyses and validation against independent datasets.

Keywords: isoprene, land cover changes, NO_X, soil, lightning, inversion, bias, TROPOMI.

1. INTRODUCTION

The tropics play a pivotal role in atmospheric composition, largely due to the high emissions of biogenic volatile organic compounds (BVOCs) (Yáñez-Serrano et al., 2020). BVOCs are central to tropospheric chemistry, influencing atmospheric oxidation capacity, ozone formation, and the production of secondary organic aerosols (Claeys et al., 2004). These compounds are ubiquitous in tropical ecosystems, owing to the high biological productivity and favourable climatic conditions in the tropics. Bottom-up estimates suggest that approximately 80% of the global BVOC flux originates in tropical regions (Guenther et al., 2012a). However, significant uncertainties persist in BVOC emission estimates (Arneth et al., 2011; Messina et al., 2016; Sindelarova et al., 2014), stemming from the region's vast biodiversity, the complex emission mechanisms, and a scarcity of direct observational data—often constrained by logistical challenges in remote areas (Yáñez-Serrano et al., 2020). Among the most poorly constrained aspects are the spatial distribution of BVOC-emitting species and the long-term variability and trends in emissions, particularly in the context of climate change. In addition, tropical forest degradation and loss due to human activities—such as agricultural expansion, urbanisation, logging, and fuelwood extraction—remain poorly quantified, further compounding these uncertainties (Hansen et al., 2013; Hubau et al., 2020).

Of all BVOCs, isoprene (C_5H_8) is by far the most abundant, with annual global emissions estimated at roughly 500 TgC/yr—accounting for around half of total BVOC emissions (Guenther et al., 2012a). Isoprene and other non-methane volatile organic compounds (NMVOCs) are the dominant precursors of formaldehyde (HCHO) over vegetated regions. HCHO, a high-yield product of BVOC oxidation with an atmospheric lifetime of just a few hours, serves as an excellent proxy for NMVOC emissions when observed from space using UV-Visible spectrometers (e.g., GOME, SCIAMACHY, OMI, TROPOMI) (Barkley et al., 2013; Bauwens et al., 2016; Kaiser et al., 2018; Marais et al., 2014; Millet et al., 2008; Palmer et al., 2003; Stavrakou et al., 2009). When combined with inverse modelling techniques, satellite HCHO column data can be used to constrain emissions of isoprene (Palmer et al., 2006) and other reactive NMVOCs (Fu et al., 2007; Stavrakou et al., 2009). However, inferring NMVOC emissions from HCHO observations presents several challenges. A key difficulty lies in the fact that multiple compounds—including isoprene, methanol, and biomass burning products—contribute significantly to HCHO levels, making it difficult to disentangle overlapping emission sources, especially during the tropical dry season when biogenic emissions and fires co-occur. Another major limitation involves systematic biases in satellite HCHO retrievals (Zhu et al., 2016), which must be characterised through independent observations and corrected (Zhu et al., 2020). Further uncertainties arise from chemical mechanisms, such as those governing isoprene oxidation (Müller et al., 2019; Peeters et al., 2014), And from the influence of nitrogen oxides ($NO_X \equiv NO + NO_2$) levels, of which atmospheric abundances are uncertain, especially at remote locations like the Amazon (Liu et al., 2016).

BVOCs and NO_X are intricately linked through their mutual influence on chemical lifetimes and degradation pathways, particularly via modulation of hydroxyl radical (OH) concentrations. While anthropogenic sources dominate global NO_X emissions (Soulie et al., 2024), natural sources such as soil and lightning contribute approximately 30% of the global total and are especially significant in remote tropical regions (Jaeglé et al., 2005). In these areas, natural emissions (vegetation, soil, lightning) are the primary contributors to NMVOCs and NO_X.

VOCs are oxidised through a series of photochemical reactions, ultimately forming CO_2 and H_2O, with HCHO being a key intermediate in this oxidation chain. The initial oxidation of hydrocarbons by OH typically forms organic peroxy radicals (RO_2). Under high-NO_X conditions, these radicals react predominantly with NO, producing HCHO and other carbonyl compounds that undergo further oxidation, leading to additional HCHO production (Atkinson, 2000). Under low-NO_X conditions, alternative pathways dominate, resulting in the formation of organic hydroperoxides (ROOH) and isomerisation products (Peeters et al., 2009). Lower NO_X levels are also associated with reduced OH concentrations, which slow the overall photochemistry and delay HCHO formation (Barkley et al., 2013; Marais et al., 2012). The complex interplay between HO_X, NO_X, and VOCs is thus a linchpin for deriving top-down (TD) isoprene emission estimates from satellite HCHO data. Notably, Marais et al. (2012) found that under low-NO_X conditions (<1 ppbv), errors in inferred isoprene emissions were estimated between 40 % and 90 %.

Accurately understanding and quantifying the magnitude, variability, and impacts of BVOC emissions on the Earth system remains a major scientific challenge. Addressing this challenge requires global-scale observations, complemented by high-quality ground-based and in situ measurements, as well as advanced modelling frameworks that can accommodate ongoing improvements in process understanding. The integration of Earth Observation (EO) data into atmospheric models holds great promise for advancing our knowledge of the atmospheric budget and dynamics of reactive trace gases across scales—from global to regional and local (Millet et al., 2008; Palmer et al., 2006).

2. STATE OF THE ART AND OBJECTIVES

EQUATOR aims to provide **an improved appraisal of the budget and role of emissions of key compounds (isoprene and NO_X) in the tropics**.

The project relies on the combined use of bottom-up (BU) and TD modelling approaches. The BU methodology is based on emission models, whereas the TD approach integrates a chemistry-transport model (CTM) and inverse modelling techniques. We use the in-house CTM of the troposphere, Model of Atmospheric composition at Global and Regional scales using Inversion Techniques for Trace gas Emissions (MAGRITTEv1.1; Müller et al., 2019) and its adjoint . Inverse modelling uses observed concentrations (e.g., from ground-based or satellite measurements) to estimate or optimise source emissions. These inferred emissions are referred to as TD emissions. By combining satellite observations as TD constraints with a priori emission inventories, inverse models refine the spatial and temporal distributions of emissions. This approach has proven invaluable for linking spaceborne HCHO and NO_2 concentrations with VOC and NO_X emissions, respectively. Previous studies have demonstrated the usefulness of spaceborne HCHO data in constraining VOC emissions from various sources, including biogenic (Abbot et al., 2003; Barkley et al., 2013; Fu et al., 2007; Millet et al., 2008; Palmer et al., 2006; Stavrakou et al., 2015), anthropogenic (Kwon et al., 2021; Stavrakou et al., 2017; Zhu et al., 2014), and pyrogenic (Bauwens et al., 2016; Stavrakou et al., 2016) through inversion techniques. Recent advances include the use of satellite measurements of isoprene for validation and as constraints in inverse models (Fu et al., 2019; Wells et al., 2020, 2022). Similarly, satellite NO_2 columns to constrain and optimise NO_X emissions (e.g., Jaeglé et al., 2005; Marais et al., 2014; Martin et al., 2003; Miyazaki et al., 2012; Stavrakou et al., 2013a; Vinken et al., 2014).

Acknowledging the intricate interplay between NO_X and VOCs through the HO_X –NO_X –VOC feedback, we design and apply a novel inversion framework that relies on the concomitant use of HCHO and NO2 satellite observations from the Tropospheric Ozone Monitoring Instrument (TROPOMI; (De Smedt et al., 2018; van Geffen et al., 2022) aboard the Sentinel-5 Precursor (S5P) satellite to simultaneously infer VOC and NO_X emissions from the African and South American continents. Several recent studies have highlighted the importance of incorporating additional constraints in the optimisation of VOC emissions (Souri et al., 2020, 2024; Wells et al., 2020). The adjoint-based optimisations, as in MAGRITTEv1.1, have two main advantages with respect to other inversion methods: they are able to address non-linear problems such the HO_X –NO_X –VOC feedback and can handle any large numbers of control parameters without increase of the computational cost. This makes the adjoint technique the most powerful tool for inferring fluxes from satellite data.

To reach the main objective, a step-by-step approach will be adopted to address the aforementioned issues and uncertainties in the derivation of BVOC emissions from satellites. The **specific objectives** of the project are:

- To properly **account for land cover changes (LCC) in BVOC emission estimates** over the past two decades based on satellite imagery data from MODIS and Landsat's instruments using the state-of-the-art Model of Emissions of Gases and Aerosols from Nature (MEGANv2.1; Guenther et al., 2012) model coupled with the canopy model Model for Hydrocarbon emissions by the CANopy (MOHYCAN; Müller et al., 2008), which is reviewed in Sect. 4.1**Error! Reference source not found.**.

- To **characterise the biases of the satellite data OMI HCHO** using independent ground-based and airborne observations and the global CTM, MAGRITTEv1.1 for the estimation of atmospheric concentrations, which is reviewed in Sect **Error! Reference source not found.**.
- To develop **novel inversion framework for quantifying the BVOC emissions** through a **joint** - simultaneous two-species (VOC and NO_X) - **inversion** of TROPOMI HCHO and NO_2 column data using the adjoint of the MAGRITTEv1.1 regional CTM, which is reviewed in Sect 4.3.
- To **quantify the magnitude of natural VOC and NO_X** (isoprene, lightning and soil NO_x emissions) in two tropical regions, Africa and South America, in 2019 through the joint inversion of TROPOMI HCHO and NO_2 observations.
- To **assess the robustness of the results** through sensitivity inversions.
- To **evaluate the TD inventories** using independent data (ground-based and satellite data)

Key innovations of this work involve (i) the derivation of bottom-up inventories of isoprene emissions that account for satellite-based LCC, (ii) the correction for biases in TROPOMI HCHO retrievals in the estimation of isoprene emissions, and (iii) the simultaneous inference NO_X and VOC emissions in the tropics from TROPOMI observations.

3. METHODOLOGY

3.1. Bottom-up BVOCs based on satellite-based LCC data

In this study, we use the state-of-the-art MEGANv2.1 (Guenther et al., 2012) coupled with the mulit-layer canopy environment model MOHYCAN (Müller et al., 2008) to generate bottom-up emission inventories accounting for satellite-based LCC.

MEGAN estimates the net emission rates into the above-canopy atmosphere. The emission flux, $F = 0.52 \cdot \varepsilon \cdot \gamma_{PT} \cdot LAI \cdot \gamma_{age} \cdot \gamma_{SM} \cdot \gamma_{CO2}$, with ε the emission factor under standard conditions, incorporates response functions to temperature and solar radiation (γ_{PT}), leaf age (γ_{age}), soil moisture stress (γ_{SM}), leaf area index (LAI) and atmospheric CO_2 levels (γ_{CO2}). Emissions are driven by meteorological fields obtained from ERA5 reanalysis (Hersbach et al., 2020). The effects of CO_2 inhibition and soil moisture stress are neglected in the present study unless stated otherwise ($\gamma_{CO2} = 1$ and $\gamma_{SM} = 1$). Monthly LAI distributions at 0.5° × 0.5° resolution (in m^2 m^{-2}) are based on the MODIS dataset (MODIS15A2H collection 6).

The MEGANv2.1 is embedded into the Community Land Model version 4 that generates a modelled vegetation map or is run offline for which users are provided with a static, satellite-based land cover (LC) map available with 16 Plant Functional Types (PFTs). This PFT distribution was based on various satellite products (MODIS, AVHRR, Ramankutty et al., 2008) and hereafter, it is referred to as **CLM**. Since high anthropogenic land use practices (forest to crop or pasture conversion, logging and urbanization) cannot be appraised by models, the present evaluation will rely on remotely sensed LCC products to evaluate this impact in recent years on isoprene emissions. We provide the first isoprene inventories based on spaceborne LC maps.

Global, remotely sensed LCC are generated at annual time steps as follows. As a first step, global, annual tree cover (TC) distributions over 2001-2018 are obtained from the Global Forest Watch (GFW version 1.6, https://www.globalforestwatch.org/) dataset that provides continuous TC field of Hansen et al. (2013) based on 30-m Landsat images. The TC dataset of GFW provides (i) the TC distribution for year 2000, (ii) the tree losses on an annual basis over 2000-2018 and (iii) a cumulative tree gain distribution over 2000-2012. We derived annual maps of GFW TC at pixel level (30-m) by accounting for the TC losses since 2000, and by implementing the 12-year cumulative tree cover gain at 0.5°×0.5° assuming a linear increase over the period, extended until 2018. Global-scale time-dependent LC (including all type of vegetation) maps over 2001-2018 are generated based on satellite-based LC products from the MODIS Land Cover Type Product (MCD12Q1 collection 6, Friedl and Sulla-Menashe, 2019) modified to match the TC distributions from the GFW. The MODIS provides datasets in the PFT classification scheme with 12 classes. The original products had to be converted into MEGAN-compatible LC distributions with 16 PFTs. The conversion from 12 to 16 classes is applied and consists in a PFT differentiation. The PFTs including trees and shrubs were further subdivided into climatic subtypes (tropical, temperate and boreal), and grasses were subdivided according to their photosynthetic pathways (C3 or C4), based on the Köppen-Geiger maps (http://www.gloh2o.org/koppen/) and climatological considerations as described in Poulter et al. (2011), with minor modifications. The final dataset referred to as **GFWMOD** dataset. The schematic representation of the different transformations applied on LC dataset from their original classifications to MEGAN-compatible datasets are shown in **Fig. 1**. Tree covers from GFWMOD were compared against (i) **FAOSTAT**, a United Nations FAO Forest Ressources Assessment database compiling national

inventories (available at https://www.fao.org/faostat/) and two other satellite-based products: (ii) **MODIS**, with the original TC representation and (iii) **ESA** .

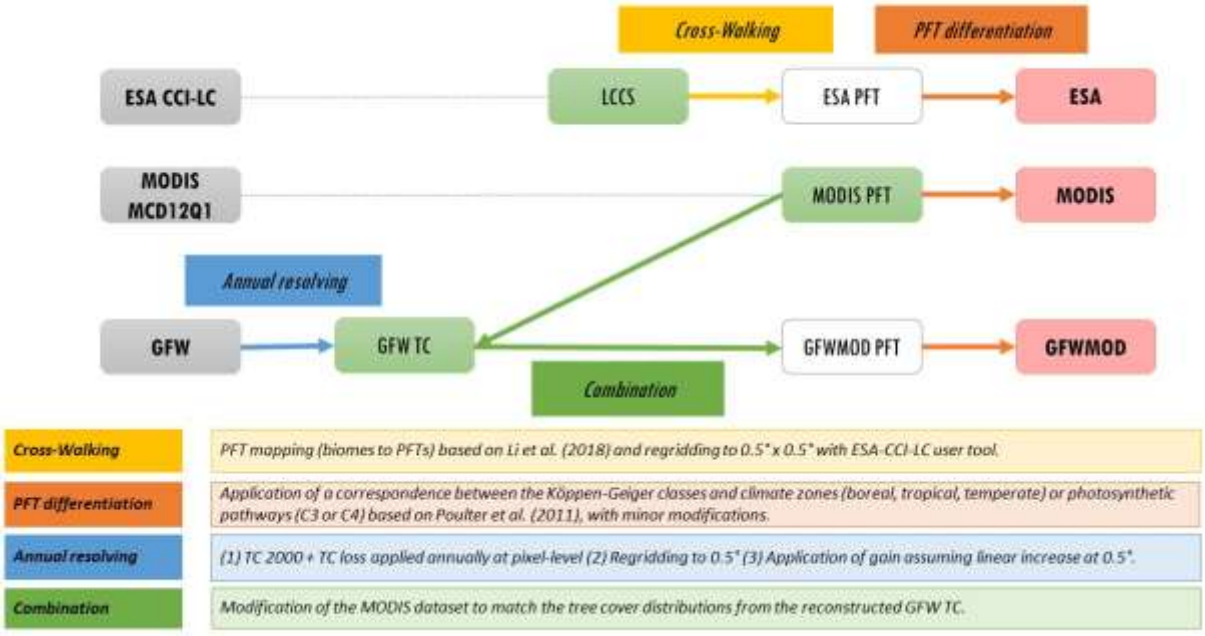

Figure 1: *Schematic representation of the consecutive transformations applied on the original datasets (in grey boxes) to generate annually updated LULC maps comprising 16 PFTs, compatible with the MEGAN model (in red boxes). Initial (annually resolved) and intermediate maps are in green and white boxes, respectively. Transformations are represented by arrows with a short description inset.*

The standard reference on global forest resources is the United Nations FAO FRA published every 5 to 10 years since 1948. It provides the global database of the reported statistics from national reports on forest properties. The latest recommendations are outlined in the FRA 2020 (http://www.fao.org/3/I8661EN/i8661en.pdf). Here we use the latest published datasets (updated in July 2020 at the time of drafting), retrieved from http://www.fao.org/faostat, and hereafter referred to as **FAOSTAT**.

The impacts of this update on the estimated isoprene fluxes over 2001-2016 were quantified with MEGAN-MOHYCAN and verified against the HCHO record. Three sets of isoprene emissions are generated using MEGAN-MOHYCAN, differing only in their LC datasets used as input: (i) **CRTL**, with CLM, the static distribution of the stand-alone version of MEGAN and (ii) **ISOPGFW** with GFWMOD, the time-dependent MODIS LC dataset modified to match the TC distribution from the GFW database, and (iii) **ISOPMOD**, with MODIS. The **ALBERI inventory** provides isoprene emissions from the ISOPGFW simulation based on GFWMOD LC maps (Opacka and Müller, 2021) and is available at https://repository.aeronomie.be/.

The evaluation method used here is based on spaceborne HCHO and a CTM and relies on the high HCHO yield from the oxidation of isoprene. The method has been widely used in past studies (Bauwens et al., 2016; Kaiser et al., 2018; Marais et al., 2012; Millet et al., 2008; Palmer et al., 2006; Stavrakou et al., 2009). The OMI HCHO product used in this study is documented in De Smedt et al. (2015, 2018) and is publicly available at http://www.qa4ecv.eu. Simulations of the atmospheric composition are performed using IMAGESv2 (Intermediate Model of the Global and Annual Evolution of Species), a

global three-dimensional CTM of the troposphere (Bauwens et al., 2016; Müller and Stavrakou, 2005; Stavrakou et al., 2016, 2018).

3.2. Characterisation of biases in satellite observations

Simulations of atmospheric composition are performed using the CTM of the troposphere, MAGRITTEv1.1 (Müller et al., 2019), which is based on the global IMAGES (Intermediate Model of the Global and Annual Evolution of Species; (Bauwens et al., 2016; Müller and Brasseur, 1995; Stavrakou et al., 2015). The chemical mechanism includes a detailed description of VOC oxidation mechanisms. It calculates the concentrations of 170 compounds with a time step of 6 h and a spin-up time of 6 months between the surface and the lower stratosphere, with 40 hybrid sigma-pressure levels in the vertical. MAGRITTE can be run either as a global model, at 2° × 2.5° resolution, or as regional model, at 0.5°× 0.5° resolution.

TD inventories are created using the inverse modelling framework built on MAGRITTEv1.1 and its adjoint. The optimisation method relies on the calculation of the partial derivatives of the cost function J i.e., a scalar metric that quantifies the mismatch between observed and model species concentrations, weighted by observational and model uncertainties. The output are optimised emission fluxes per model grid, month and emission category. Optimised fluxes are calculated using an iterative quasi-Newton minimisation algorithm based on the full adjoint of MAGRITTEv1.1 until convergence is attained, i.e. when the norm of the gradient of the cost function is decreased by a large factor (> 20) with respect to its initial value, which typically requires 30–60 iterations.

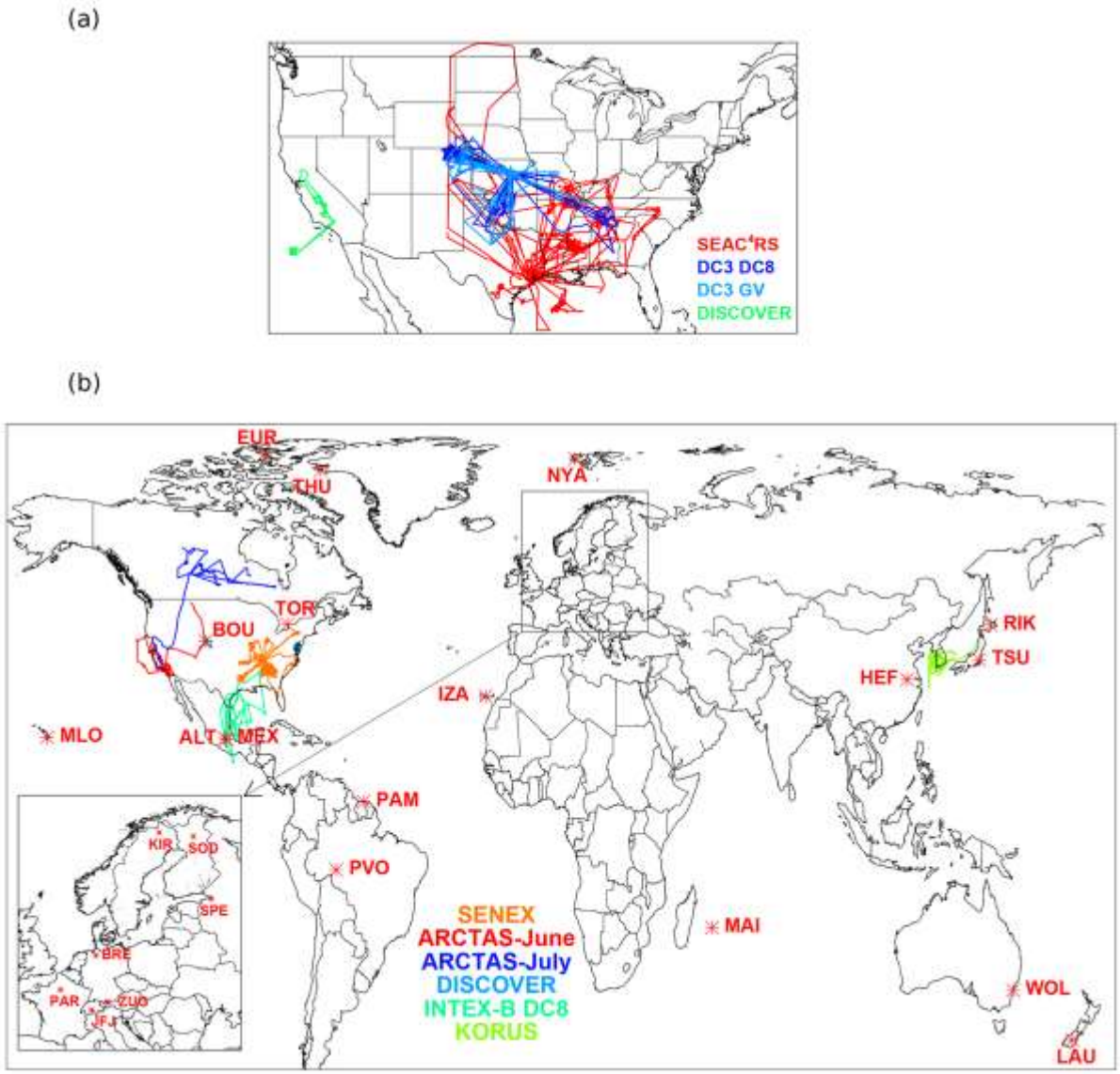

Figure 2: *(a) Flight tracks of the aircraft missions (DC3, SEAC[4]RS, DISCOVER-AQ California) used as constraints in the aircraft-based inversion; (b) flight tracks of the additional aircraft campaigns used for global model evaluation and location of FTIR stations used in this work to evaluate OMI HCHO columns. Note that the stations Garmisch and Saint-Denis are not shown, given their close proximity to the stations Zugspitze (ZUG) and Maïdo (MAI), respectively.*

The inversions and thus, the bias characterisation is performed on the Ozone Monitoring Instrument (OMI), launched in 2004 aboard the Aura satellite crossing the Equator around 13:30 LT (local time). Here, we use the QA4ECV OMI HCHO dataset (v1.2, https://doi.org/10.18758/71021031) that is fully described in Stavrakou et al. (2018). The OMI ground pixel size varies from 13×24 km^2 at nadir to 28 × 150 km^2 at the edges of the swath. For the bias characterisation of OMI HCHO, we used (a) a global network of Fourier-transform infrared (FTIR) measurements and (b) four airborne campaigns. More specifically, 26 harmonized FTIR HCHO retrieval datasets as listed in Table 2 of Vigouroux et al. (2018) and four HCHO datasets from three campaigns conducted during 2012-2013 over the United States are used, namely DC3-DC 8 in 2012 (Weibring et al., 2007), DC3-GV in 2012 (Richter et al., 2015), SEAC^{4}RS in 2013 (Richter et al., 2015) and DISCOVER-AQ in 2013 (Weibring et al., 2007). Those campaigns, as well as seven additional campaigns are used to evaluate the inverse modelling results. Additional campaigns are MILAGRO in 2006 (DC-8, Fried et al., 2008, 2011), ARCTAS-CARB in 2008

(Fried et al., 2008), ARCTAS-B (Fried et al., 2008), DISCOVER-AQ Maryland in 2011 (Weibring et al., 2007), DISCOVER-AQ Colorado in 2014 (Weibring et al., 2007), SENEX in 2013 (Cazorla et al., 2015) and KORUS-AQ in 2016 (Fried et al., 2020; Richter et al., 2015). The flight tracks and locations of FTIR stations are shown in **Fig. 2**.

TD VOC estimates are obtained using an adjoint inverse modelling framework built on the MAGRITTEv1.1 model and OMI HCHO. For the global study, we perform inversions on a $2^\circ \times 2.5^\circ$ grid with monthly temporal resolution covering the 2005-2017 period. Meteorological fields are obtained from the ERA5 ECMWF reanalysis (Hersbach et al., 2020). The *a priori* emission inventories are prescribed as follows. Vegetation fire emissions are provided from GFED4s (van der Werf et al., 2017). Isoprene and monoterpene fluxes are calculated by the MEGAN model embedded in the MOHYCAN canopy environment model (Guenther et al., 2012b; Müller et al., 2008) at $0.5^\circ \times 0.5^\circ$ based on the ERA5 reanalysis meteorological fields and leaf area index (LAI) data from MODIS Collection 6 reprocessed by Yuan et al. (2011). The CO_2 inhibition effect is accounted for by using Possell and Hewitt (2011). The effects of soil moisture stress on BVOCs are neglected. Anthropogenic emissions of CO, NO_x, SO_2 and carbonaceous aerosols are taken from HTAPv2 (Hemispheric Transport of Air Pollution version 2) (Janssens-Maenhout et al., 2015) for 2010. The speciated NMVOC emissions are obtained from EDGARv4.3.2 (Huang et al., 2017) between 2005 and 2012 and are taken to be equal to their 2012 values afterwards.

3.3. Top-down inventories of VOC and NO_X using joint inversion

3.3.1. TROPOMI HCHO and NO_2

For the inversion simulations, we use tropospheric 2019 HCHO and NO_2 vertical column densities (VCD) measured by TROPOMI on board the ESA Sentinel-5 Precursor (S5P) satellite that flies in a low Earth polar orbit with an Equator-crossing time of ~ 13:30 local time. TROPOMI has a 2600 km wide swath and provides near-daily global coverage at a spatial resolution of 3.5 × 5.5 km2 at nadir. The TROPOMI NO2 dataset used in this study is the Products Algorithm Laboratory (PAL) version v2.3.1, which is the intermediate S5P-PAL reprocessing data (Eskes et al., 2021). We select tropospheric NO_2 data with quality assurance values (QA) above 0.75, per product recommendation and screen out TROPOMI NO_2 data with strong biomass burning (BB) influences. TROPOMI NO_2 data are regridded onto the model resolution (0.5°).

Validation studies (Compernolle, 2024; van Geffen et al., 2022; Verhoelst et al., 2021) reported biases in TROPOMI NO_2 columns based on ground-based MAX-DOAS stations. Most of these stations show median columns above 2×10^{15} cm^{-2}, i.e. higher than the typically observed TROPOMI NO_2 levels in Africa. Exceptions are two Japanese sites, Fukue and Cape Hedo, for which very large TROPOMI overestimations (> +60 %) were found (Compernolle, 2024). However, because these stations are maritime ones and the vertical sensitivities of TROPOMI and MAX-DOAS are very different (Oomen et al., 2024), these validation results should be considered with caution. Therefore, in the absence of a robust validation study in low-NO_X areas typical of NO_2 levels in Africa and South America, no bias correction was applied to TROPOMI NO_2 column densities.

For HCHO, we use the Copernicus operational product TROPOMI S5P HCHO columns (Ω_{HCHO}) (De Smedt et al., 2021) with QA > 0.5 gridded onto the model resolution (0.5°). Since the study on inversions began before the publication of the bias characterisation work, the TD estimates are

inferred based on TROPOMI HCHO corrected for bias using the following linear relationship based on Vigouroux et al. (2020):

$$\Omega_{HCHO}^{BC} = 1.587 \cdot \Omega_{HCHO} - 1.857 \times 10^{15}\,\mathrm{molec.\,cm^{-2}},$$

where Ω_{HCHO}^{BC} is the bias-corrected column. This formula is derived from a global-scale validation study of TROPOMI HCHO data using Fourier transform infrared (FTIR) data from 25 stations worldwide.

3.3.2. A priori emissions

Our reference isoprene inventory uses a gridded distribution of the basal emission factor at standard conditions (provided in MEGANv2.1) based on species composition and species-specific emission factors. For the study of the effect of LCC on isoprene emissions and trends, we calculate the emission potential map based on PFT-dependent emission factors (Guenther et al., 2012).

A priori soil NO emissions are obtained from the dataset of Weng et al. (2020) generated with the Harvard-NASA Harmonized Emissions Component (HEMCO) version 2.1 model. Above-canopy fluxes accounting for biological and meteorological drivers are calculated following Hudman et al. (2012). The latter includes (i) an exponential dependence on soil temperature between 0°C and 30°C (constant at T > 30°C), (ii) a Poisson function scaling for soil moisture dependence, (iii) pulsing according to the parameterisation of Yan et al. (2005), (iv) soil nitrogen input from chemical and manure fertilisers (atmospheric N-deposition is not accounted for, as it contributes for only ca. 5% globally, according to Hudman et al. (2012)), and (v) the canopy reduction factor. For this study, we use the monthly global emissions of soil NO_X dataset based on assimilated MERRA-2 meteorology, originally at resolution of 0.5° lat. × 0.625° lon., regridded to 0.5°× 0.5°. Averaged over all years (1980-2017), the global total soil NO_X emissions amount to 9.5 TgN yr^{-1}. As a sensitivity study, we use an alternative dataset, the CAMS-BIO-SOILv2.4 inventory (Simpson et al., 2023; Simpson and Segers, 2024), hereafter referred to as CAMS. This inventory is also calculated following Steinkamp and Lawrence (2011) and Yienger and Levy (1995), with inputs from ERA5 reanalysis (Hersbach et al., 2020). While the global total CAMS emission (9.1 TgN) is very similar to the HEMCO inventory, the spatial distribution and seasonal evolution differ greatly.

The lightning emissions of NO_X in the reference case relies on the parameterisation of Price and Rind (1992) and Martin et al. (2007) with convective cloud top heights derived from the ERA5 reanalysis (Hersbach et al., 2020), assuming a ratio of 0.75 between the NO production per flash due to intra-cloud and cloud-to-ground flashes (Martin et al., 2007). The monthly averaged global distribution of lightning flash density follows the spaceborne climatology of the NASA Optical Transient Detector (OTD) and Lightning Imaging Sensor (LIS) satellite instruments (Cecil et al., 2014). The lightning emissions are distributed vertically according to Pickering et al. (1998). The mid-latitude lightning emissions are scaled up by a factor of 4, following Martin et al. (2007), and the total lightning emission is scaled to 3.4 TgN yr^{-1} globally.

3.3.3. Regional CTM MAGRITTEv1.1, its adjoint and the two-species inversion

For the purposes of this project, **the inversion algorithm will be adapted to perform a two-species simultaneous inversion of VOC and NO_X based on TD constraints provided by TROPOMI HCHO and**

NO_2 tropospheric column concentrations. This setup takes advantage of the constraints provided from both satellite datasets, while accounting for NO_X-VOC chemical interdependencies. The modelled monthly averages are sampled at the times and locations of the TROPOMI monthly means and account for the averaging kernels of the observations. A total of five categories are optimised: anthropogenic NO_X, soil NO_X, lightning NO_X, biogenic VOC, anthropogenic VOC and biomass burning VOC. Since fire scenes are filtered out of TROPOMI NO_2 data, the biomass burning NO_X emissions are not optimised but are scaled as the biomass burning VOC emissions.

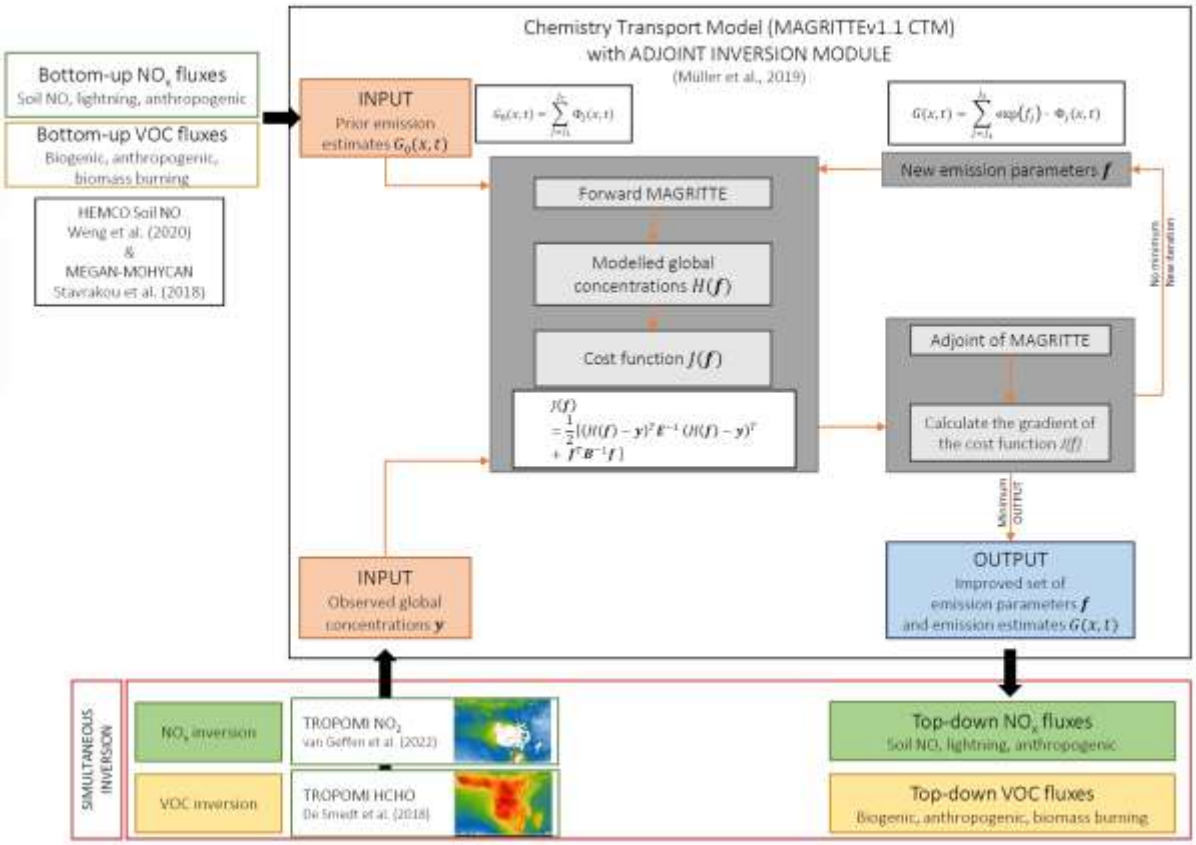

Figure 3: *Schematic flowchart of the inverse modelling approach using the adjoint inversion module of MAGRITTEv1.1 with inputs from bottom-up inventories and satellite observations.*

Two regional simulations are performed for year 2019 that cover African domain delimited by 30°S-17°N latitude and 18°W-56°E longitude and the South American domain that is between 15°N-34°S latitude and 33°-85°W longitude, with a 0.5° × 0.5° horizontal resolution. In regional mode, the boundary conditions are provided offline by the global MAGRITTEv1.1 model. Meteorological fields are obtained from ERA5 analyses (Hersbach et al., 2020). The model uses anthropogenic emissions of NO_X, CO, SO_2, NH_3, and non-methane VOC species from the global CAMS-GLOB-ANTv5.3 inventory (Granier et al., 2019). The biomass burning inventory is provided by the Quick Fire Emissions Dataset (QFED) version 2.4 (Darmenov and Da Silva, 2015; Pan et al., 2020) with emission factors from Andreae (2019). Natural emissions of isoprene, monoterpenes, and methylbutenol as well as natural sources of NO_X are prescribed as detailed in **Sect. 3.3.2**. Biogenic emissions of acetaldehyde and ethanol are parameterised following Millet et al. (2010), biogenic methanol emissions are from the MEGANv2.1 inventory, and biogenic CO emissions are accounted for following Müller and Stavrakou (2005). We

assume a factor of 3 uncertainty on errors in a priori VOC and NO_X emissions and a decorrelation length (500 km).

For the evaluation of TD inventories, we focus on natural emissions of NO_X and VOC (soil, lighting and isoprene). To assess the robustness of our results, sensitivity simulations will be carried out for Africa. The reference inversion was setup using inventories described above and based on our best assumption of errors on a priori emissions (factor of 3 uncertainty) and decorrelation length (500 km). We performed an ensemble of additional inversions, summarised in **Table 1**. Those runs aimed at assessing the sensitivity of the results (for 2019) on (i) the inversion methodology (by performing single-species inversions, labelled SVOC and SNOX), (ii) the bias correction of satellite HCHO data (cf. NOBC), (iii) the a priori isoprene (cf. ALBE) and soil NO (cf. CAMN) emission inventories, and (iv) assumptions regarding inversion parameters, namely the a priori errors (cf. LERR and HERR).

Table 1: *Description of the performed runs, including the standard inversion (STD) and the sensitivity runs.*

Inversion	Description
STD	Two-species optimisation based on TROPOMI HCHO and NO_2
SVOC	Single-compound inversion using TROPOMI HCHO; only VOC fluxes are optimised
SNOX	Single-compound inversion using TROPOMI NO_2; only NO_X fluxes are optimised
NOBC	As STD, but without bias correction on TROPOMI HCHO
INDA	As STD, use INDAAF surface NO_2 as an additional constraint
ALBE	As STD, use the ALBERI isoprene emissions inventory as a priori (Opacka et al., 2021)
CAMN	As STD, use the CAMS-BIO SOILv2.4 soil NO inventory as a priori (Simpson et al., 2023)
LERR	As STD but with lower errors for VOC, NO_X natural emissions (factor of 2 instead of 3)
HERR	As STD but with higher errors for VOC, NO_X natural emissions (factor of 4 instead of 3)

3.3.4. Evaluation data

Satellite-based data: Satellite-based isoprene column products are obtained from the **Cross-track Infrared Sounder (CrIS)**, a Fourier transform spectrometer flying in a sun-synchronous orbit onboard the NASA/NOAA Suomi-NPP satellite launched in October 2011 (Wells et al., 2020, 2022). The instrument features a high spectral performance (0.625 cm^{-1} resolution in the longwave IR 650-1095 cm^{-1}), low noise (e.g., ~0.04 K at 900 cm^{-1} and 280 K) and near-global coverage twice daily (0130 and 1330 local time) with the afternoon overpass corresponding with the peak of isoprene emissions. The isoprene retrieval algorithm relies on the hyperspectral range index (HRI) to quantify column abundances (Franco et al., 2018) retrieved from thermal infrared radiances at the ν_{27} and ν_{28} (from 890-900 cm^{-1}) absorption regions. Monthly distributions at 0.5°×0.625° resolution (regridded onto 0.5°) for year 2019 are used to evaluate the a priori and optimised isoprene columns. Climatological means 2012-2020 of CrIS isoprene columns are available at

https://conservancy.umn.edu/items/4fe84ff6-352c-4d8e-b777-b203aca870ba and 2019 data were provided by D. Millet.

Lightning NO emissions are the dominant direct NO_X source in the upper troposphere (UT) compared to other sources such as aircrafts, deep convective uplifts of boundary layer pollution, and downwelling from the stratosphere (Lamarque et al., 1996; Murray, 2016; Schumann and Huntrieser, 2007). The evaluation of a priori and TD lightning NO_x emission will be conducted using a proxy, the **satellite-based upper troposphere (450–180 hPa) volume mixing ratios (VMR) of NO_2**, obtained via the **cloud-slicing technique** applied to the total columns of NO_2 from TROPOMI (Horner et al., 2024). This technique retrieves the NO_2 VMR using the observed relationship between the cloud top pressure and the column above optically thick clouds developed by Ziemke et al. (2001) for ozone in the free troposphere based on cloud fraction and cloud-top height data from the FRESCO-wide algorithm (Eskes and Eichmann, 2023). Five discrete layers, from the surface to the tropopause, of seasonal averaged NO_2 VMRs are available at 1°×1° averaged between 2018 and 2022 are available at https://maraisresearchgroup.co.uk/datasets.html. After regridding to a finer spatial resolution of 0.5°, the cloud-sliced UT NO_2 was obtained by averaging the two upper tropospheric layers, namely 180-320 and 320-450 hPa. This dataset will be further referred to as cloud-sliced NO_2.

Ground-based data: Figure 4 shows the locations of the ground-based measurements used in the evaluation study over Africa and South America. In particular, we conducted a detailed review of studies published in peer-reviewed journals and extracted data from those publications reporting field measurements of soil NO fluxes over tropics. The compilation accounts for 63 in situ soil NO flux measurements in South America, Africa and Asia from 30 sites. Measurements were performed at either wet or dry seasons in various biomes through various campaigns that took place during the 1985—2006 period. Across Africa, a total of 19 measurements of in situ soil fluxes were collected for this study at 11 sites (Fig. 4(a)) spread across the continent, biomes and seasons as detailed in **Table S1** (cf. Annexes). In South America, the compilation comprises 65 in situ soil NO flux data from 14 sites (Fig. 4(b)) (**Table S2**, cf. Annexes).

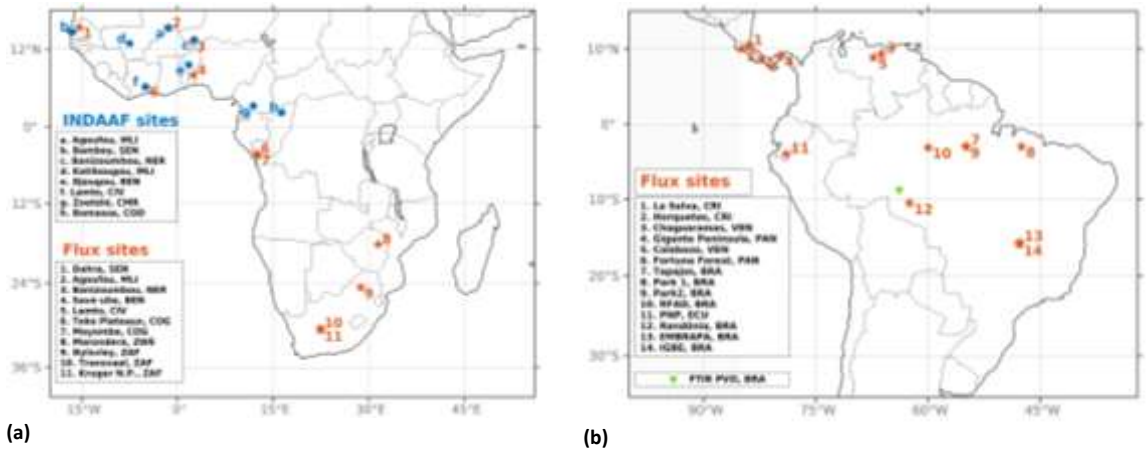

Figure 4: *Map of the ground-based measurements. The map shows the location of (a) in situ soil NO flux measurement sites (orange) as well as NO_2 concentrations sites from the INDAAF network (blue) providing NO_2 mixing ratios in Africa (17°N–30°S, 18°W–56°E), and (b) in situ soil NO flux measurement sites (orange) as well as the FTIR station at Porto Velho (PVO) in South America (15°N–34°S, 33°–85°W with the hashed region is not included in the model domain).*

The International Network to study Deposition and Atmospheric composition in Africa (INDAAF) network provides monthly surface concentrations of SO_2, HNO_3, NH_3, NO_2 and O_3 at 7 sites (**Fig. 4**) located in rural, unperturbed areas in West and Central Africa (Adon et al., 2010; Ossohou et al., 2023). This ground-based network of passive samplers is used for the evaluation of surface NO_2 concentrations. We use a six-year record of observations (2015-2020) except for the Agoufou (2015-2018) and Bambey (2016-2020) sites for which only a shorter period is available. Adon et al. (2010) reports a reproducibility of ca. 10% in the inter-comparison tests between passive and active samplers.

We use isoprene and formaldehyde column measurements from ground-based Fourier Transform InfraRed (FTIR) at Porto Velho (8.77°S, 63.87°W; Vigouroux et al., 2018), a city of 550,000 inhabitants located on the border between the Brazilian states of Rondônia and Amazonas, at the edge of the Amazon rainforest (**Fig. 4(b)**). The ground-based instrument is a Bruker 125M high-resolution (up to 0.006 cm^{-1}) spectrometer previously deployed at Saint-Denis, Réunion Island (Stavrakou et al., 2012; Vigouroux et al., 2009). Since 2016, the instrument has been used at Porto Velho for satellite validation of formaldehyde, methane, and carbon monoxide (Sha et al., 2021; Vigouroux et al., 2020). Measurements in the spectral range needed for isoprene detection started in June 2019 and ended October 2019. These measurements represent the first retrievals of isoprene from ground-based FTIR spectra.

4. SCIENTIFIC RESULTS AND RECOMMENDATIONS

4.1. Bottom-up biogenic emission fluxes accounting for land cover changes (WP1)

The **goal of WP1** was to **implement global space-based observations of LCC to the MEGAN-MOHYCAN model** and validate its predictions against a decadal record of HCHO observations from the OMI instrument.

4.1.1. Introduction

Among the BVOCs emitted by plant foliage, isoprene is by far the most important in terms of both global emission and atmospheric impact. As isoprene is primarily emitted by terrestrial vegetation, with trees being the major contributors, its emission is critically dependent on LC (e.g. tree, shrub, grass, crop). The current isoprene emission inventories are usually based on LC maps that are either modelled and dynamic or satellite-based and static. In this study, we use the state-of-the-art MEGANv2.1-MOHYCAN model to generate bottom-up emission inventories accounting for satellite-based LCC. The MEGANv2.1 is embedded into the Community Land Model version 4 that generates a modelled vegetation map or is run offline for which users are provided with a static, satellite-based LC map available with 16 PFTs. This PFT distribution was based on various satellite products (MODIS, AVHRR, Ramankutty et al., 2008) and hereafter, it is referred to as CLM. Since high anthropogenic land use practices (forest to crop or pasture conversion, logging and urbanization) cannot be appraised by models, the present evaluation will rely on remotely sensed LCC products to evaluate this impact in recent years on isoprene emissions. We provide the first isoprene inventories based on spaceborne LC maps.

The complete study was presented in a peer-reviewed publication in *Atmospheric Chemistry and Physics* (Opacka et al., 2021).

4.1.2. Disparities in tree covers among datasets

The global TC distributions for the year 2001 are depicted in **Fig. 5**. The global TC areas provided therein and listed in **Table 2** range from 30.6×10^6 km^2 for ESA to 52.6×10^6 km^2 for MODIS, with the TC areas of GFWMOD and CLM falling in between with 32.2 and 38.5×10^6 km^2, respectively. MODIS TC stands out as it exhibits extensive patches of high TC densities (> 90 %) in all major forested regions. In contrast, GFWMOD and ESA exhibit lower densities (40 %–80 %) in the Northern Hemisphere. The ESA cover density reaches 90 % in the tropical forests of Central Africa, the Amazon, Southeast Asia, and Oceania. The lowest densities are found in the ESA dataset, e.g. in the eastern US, the West African coast and Indonesia. **Table 2** compares the global satellite-based TC with figures from FAOSTAT based on national reporting. According to FAOSTAT, the global forest area reached 41.5×10^6 km^2 in 2001, which lies well within the satellite-based TC areas.

Table 2: *Global TC areas (in 10^6 km^2) in the year 2001 and trends (in % yr^{-1} and in km^2 yr^{-1}) over 2001–2016 based on FAOSTAT, the static LC map (CLM), and the satellite products (ESA, MODIS, and GFWMOD).*

	Area in 2001	Trends	
	(10^6 km^2)	(% yr^{-1})	(km^2 yr^{-1})
FAOSTAT	41.5	-0.12	-49 727
CLM	38.5	N.A.	N.A.
ESA	30.6	-0.05	-13 968
MODIS	52.6	0.03	18 184
GFWMOD	32.2	-0.26	-83 336

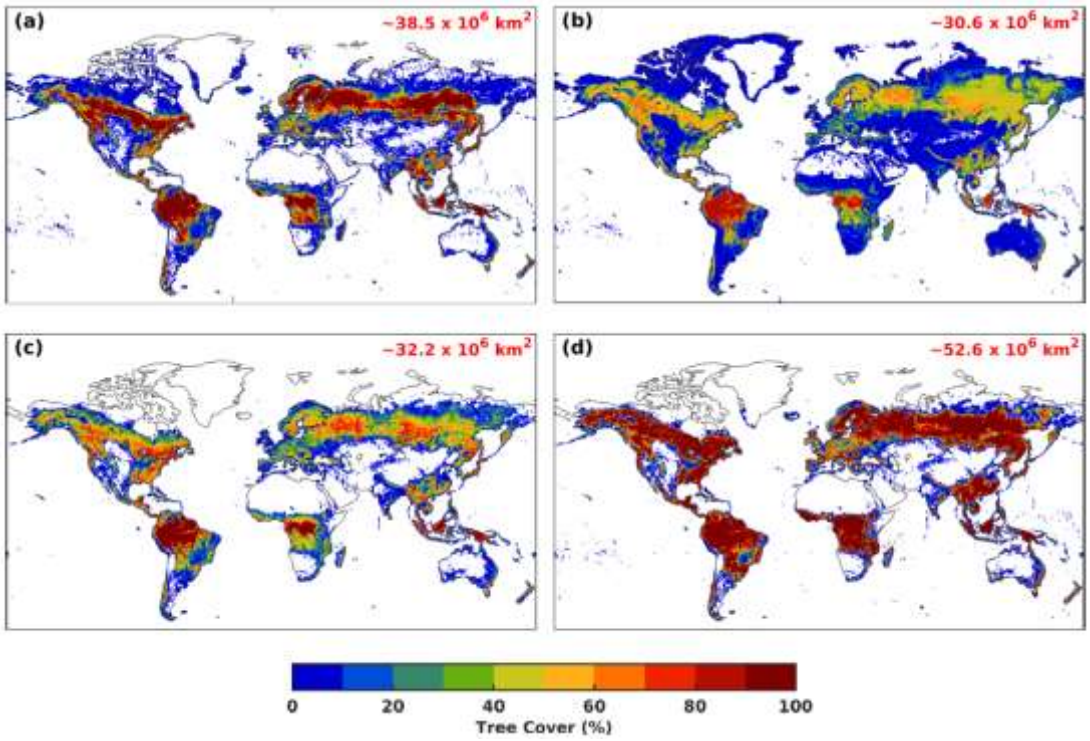

Figure 5*: Spatial distribution of the TC for (a) the static LC map CLM (for the present day) and for the satellite-based datasets ((b) ESA, (c) GFWMOD, and (d) MODIS) for the year 2001. The corresponding global TC areas are provided inset.*

Time series of global TC areas normalised to the 2001 values are displayed in **Fig. 6(a)**, and total global trends are shown in **Fig. 6(b)** for 2001–2016. Of all datasets, GFWMOD exhibits the strongest negative trend, equal to −0.26 % yr^{-1} (ca. −83 500 km^2 yr^{-1}), which is about 3–5 times as fast as the FAOSTAT and ESA trends (**Table 2**). National inventories from FAOSTAT estimate a global negative trend of about -0.12 %yr^{-1} over 2001—2016. According to some local censuses, clear cut areas and seedling or young trees are classified as forest, while satellite-based mappings of trees rely on a minimum height (2 or 5 meters). The ESA dataset shows the lowest variation (ca. −14 000 km^2 yr^{-1}), with a stable phase between 2004 and 2009. While net deforestation is found in both GFWMOD and ESA datasets, the MODIS dataset exhibits a small positive linear trend of ~ 0.03 % yr^{-1}. The MODIS TC declines in 2001–2003 and after 2014 are more than compensated for by the slow increase in 2003–2014 (**Fig. 6(a)**). Of all biomes, tropical trees experienced the greatest net losses according to GFWMOD and ESA datasets. This loss is 3.5 times greater in GFWMOD than in ESA (**Fig. 6(b)**). MODIS also presents a net decline in tropical trees (−14 600 km^2 yr^{-1}), almost entirely located in South America (**Fig. 7**) with little net changes over Africa and Southeast Asia, but it is offset by positive trends in the boreal and especially in the temperate domain. Unlike GFWMOD, which features a net loss in all domains, MODIS

demonstrates net gains at middle and high latitudes of the Northern Hemisphere, with the biggest changes encountered in temperate forests (18 400 km^2 yr^{-1}). As a result, these biomes, with strong trends and covering together roughly 60 % of the total TC area, drive the global net increase found in the MODIS dataset. Compared to the other two datasets, the MODIS distribution shows significant impacts over much larger areas (**Fig. 7)**, mainly in the periphery of major forests of South America, Africa, and the southeastern US. In contrast, GFWMOD displays large net changes within higher-density forest canopies like those in the tropics, the southeastern US, China, and Scandinavia (**Fig. 7**). In the ESA dataset, the net TC changes are sparse and weak, about 1 order of magnitude lower than in the two other satellite-based products, and show the highest values in boreal and temperate regions (**Fig. 6 (b)** and **Fig. 7**). High resolution TC provided by GFW is a great asset for tracking small-scales changes in TC. Unlike South America and Asia where forest losses are mainly commodity-driven (large scale disturbances), forest losses in Africa are due to shifting agriculture (small-scale changes) (Curtis et al., 2018). Other satellite-based LC (MODIS and ESA) were found to be unable to capture small-scale changes over Africa (**Fig. 7**).

The comparison of the three satellite-derived products has shown great discrepancies in their spatial distributions, areas, and trends. The paramount difference between all products is the plurality of definitions of TC based on the criteria of height and canopy density. The differences stem also from various factors leading to uncertainties and inconsistencies: acquisition methods (e.g. missions and sensors), mapping methodology (classification algorithms of spectral reflectance into LC classes), original classification definition related to height and canopy thresholds, and the conversion of the original LC into PFT distribution (Congalton et al., 2014), as well as the spatial resolution. In particular, the often vague or inadequate definition of LC classes in the original products results in much arbitrariness in the cross-walking tables applied to map those LC products onto the CLM4 PFTs. Finally, the spatial resolution also plays a role in the magnitude of changes since finer resolutions can capture disturbances occurring at finer scales. GFWMOD based on 30 m pixels exhibits stronger net changes in the forested areas, whereas in lower resolution datasets, ESA (300 m) and MODIS (500 m), the trends are representative of dominant LCC that are mainly seen at the outskirts of the forested regions, in particular in South America. The ESA dataset shows the lowest net changes because the LC changes were first detected at 1 km resolution and then delineated to a higher resolution of 300 m (ESA-CCI-LC, 2017). The fine resolution of the Hansen et al. (2013) database is a unique asset for tracking LC changes and trends. However, GFWMOD comes with its own shortcomings. It inherits uncertainty and inconsistencies in the trend due to the changes in the mapping methodology of TC losses from year 2011 onwards in the Hansen et al. (2013) dataset. The global forest losses of 2011–2018 used an updated processing for detection, and, at the time of drafting, the dataset was not yet reprocessed prior to 2011.

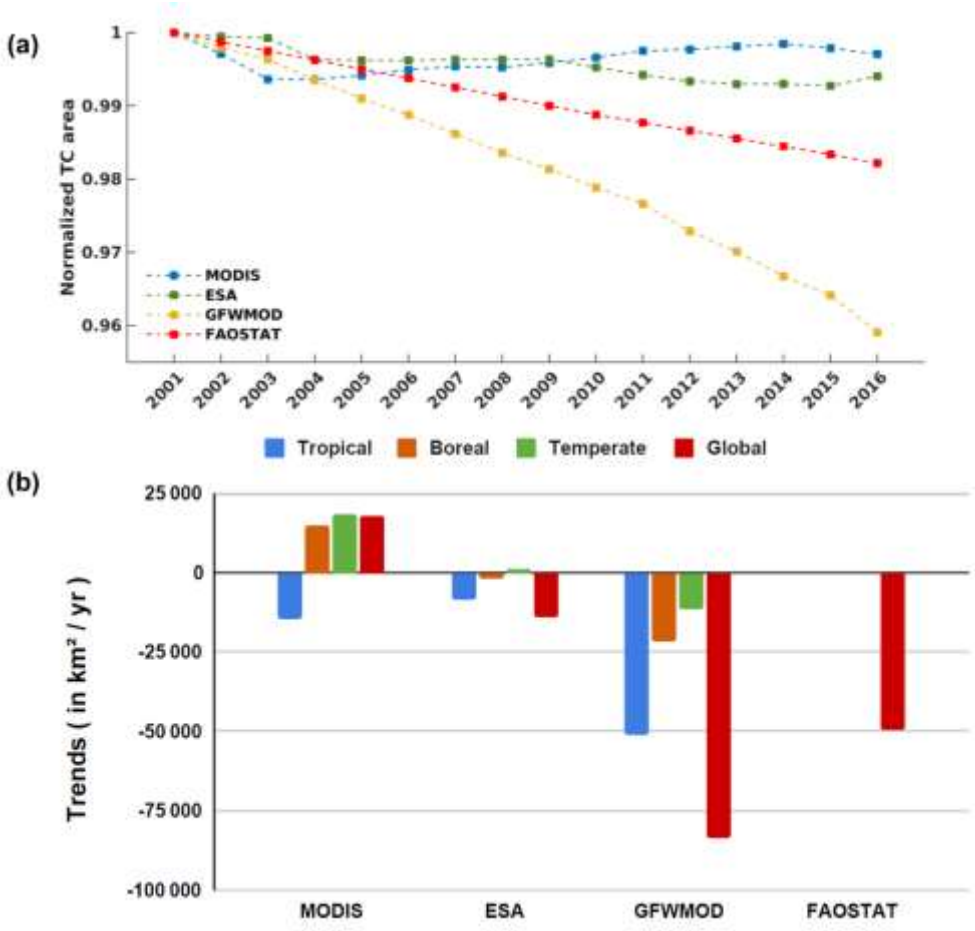

***Figure 6**: TC trends over 2001–2016. (a) Time series of the global net changes in TC areas (normalised to 2001 values) from FAOSTAT, MODIS, ESA, and GFWMOD datasets and (b) total net TC trends at global scale and per climate zone. For the FAOSTAT dataset, TC trends per climate zone are not available.*

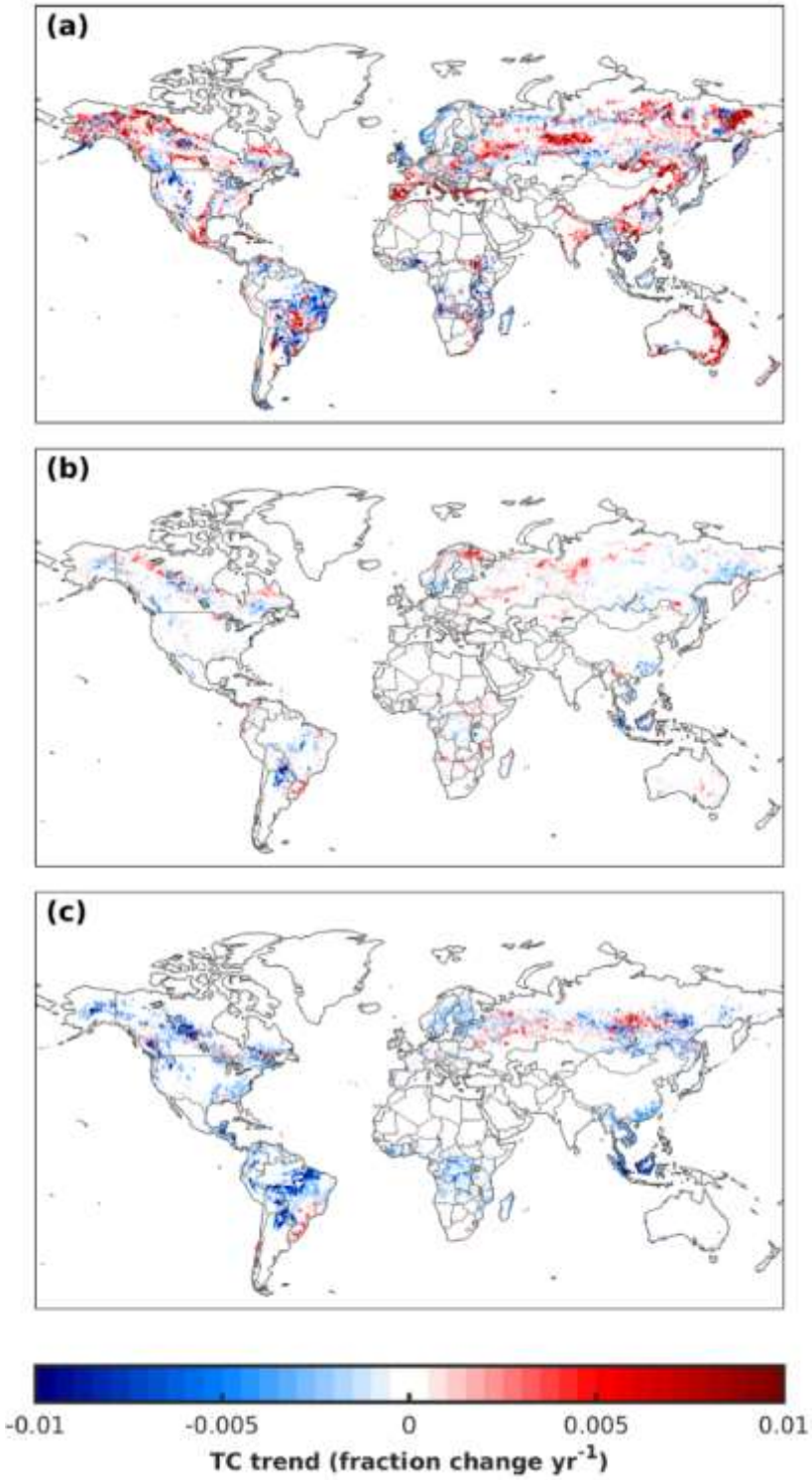

Figure 7: *Spatial distribution of the linear net trend (change in cover fraction per year) in TC for 2001–2016 in the (a) MODIS, (b) ESA, and (c) GFWMOD datasets. The fraction change per year is calculated by dividing the TC trends in each grid cell (expressed in km^2 yr^{-1}) by the corresponding grid area.*

4.1.3. Impact on isoprene emissions

The average annual global isoprene emission is estimated at ca. 420 Tg for the 2001–2016 period in the CTRL simulation (**Table 3**), whereas it is 24 % higher in the ISOPMOD run and 15 % lower in the

ISOPGFW simulation. These figures remain in the range (350–800 Tg yr^{-1}) found in previous estimations with MEGANv2 using various drivers (Guenther et al., 2012a). By comparison, bottom-up inventories such as CAMS-GLOB-BIOv1.1 (Granier et al., 2019; Sindelarova et al., 2014), its predecessor MEGAN-MACC (Sindelarova et al., 2014), and the Royal Belgian Institute for Space Aeronomy (BIRA-IASB) inventory (Stavrakou et al., 2018; https://emissions.aeronomie.be) estimate the mean global annual total of emitted isoprene in the range of 380–590 Tg. The effects of CO_2 inhibition and soil moisture were neglected in those inventories except for MEGAN-MACC, which accounted for CO_2 inhibition (Sindelarova et al., 2014). The inclusion of the CO_2 inhibition effect according to the parameterisation of Possell and Hewitt (2011) in our study would lead to an annual emission decrease of the order of 3 %. Including the soil moisture stress effect (γ_{SM}) based on ERA-Interim soil moisture data would lead to a further decrease of the order of 10 %. Disparities among the inventories are primarily attributed to differences in meteorological fields and emission potential distributions (Arneth et al., 2011), with additional possible contributions of differences in the canopy environment models and in the LAI datasets.

The distribution of isoprene emissions of the ISOPGFW simulation (**Fig. 8**) shows that the highest values are found over Amazonia, the Yucatán Peninsula, West and Central Africa, and Southeast Asia, in particular Borneo. These spatial patterns reflect the warm temperature, high radiation fluxes, and high isoprene emission factors generally found in the tropics. Secondary maxima are found at temperate latitudes during summertime, in particular over the southeastern US and southern China. ISOPMOD predicts higher emissions than the other two simulations (CTRL and ISOPGFW) over many regions as a consequence of its higher TC (**Fig. 5**), in particular over northeastern Brazil, large parts of Africa, South China, and the eastern US (not shown). Regional dissimilarities between the datasets are mainly located in isoprene-rich areas and stem from differences in the canopy coverage (not shown).

***Table 3**: Global mean annual isoprene emissions (in Tg) and trend (% yr^{-1}) for the 2001–2016 period in CTRL, ISOPMOD, and ISOPGFW simulations.*

	Mean (in Tg)	Trend (%yr-1)
CTRL	418	0.94
ISOPMOD	520	0.90
ISOPGFW	354	0.61

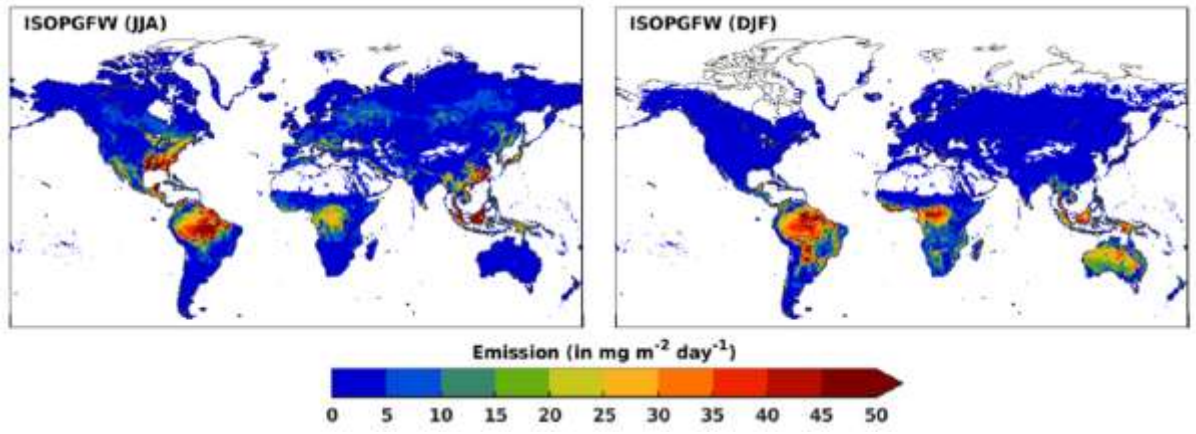

***Figure 8:** Distribution of isoprene emissions (in mg m^{-2} day^{-1}) for (a) June–July–August (JJA) and (b) December–January–February (DJF) in 2001 in simulation ISOPGFW.*

The trend of the global annual isoprene emissions in the CTRL run is estimated at 0.94 % yr^{-1} (**Fig. 9**). Since the PFT distribution and therefore the isoprene emission factors were held constant in this simulation, the interannual variability in emissions in this simulation is essentially due to the interannual variability in meteorological parameters, primarily temperature and visible radiation fluxes. Accounting for LCC with the MODIS and GFWMOD LC maps results in a cutback of the global isoprene emission trends by 0.04 and 0.33 % yr^{-1}, respectively. In ISOPMOD, the deceleration in the global trends pertains to a negative trend of tropical tree cover in MODIS (**Fig. 6**) which more than compensates for the increasing coverage of temperate and boreal trees given the large share of the tropics (80 %) in the global emissions. In ISOPGFW, the significant decline in tree cover in all climate zones explains the strong drop in the global isoprene emission trend, from 0.94 % to 0.61 % yr^{-1}. Note that the CO_2 inhibition effect, not considered in those simulations, would further offset global trends by about 0.5 % yr^{-1} according to the parameterisation of Possell and Hewitt (2011), whereas the soil moisture stress of MEGANv2.1 has little impact on trends. The effect of LAI trends on global emission trends is very small: a positive increment of +0.06 % yr^{-1} was calculated based on an additional sensitivity simulation in which LAI interannual variability was omitted. The interannual variability in isoprene emissions is mainly driven by meteorology and is positively correlated with the Oceanic Niño Index (Lathière et al., 2006; Müller et al., 2008; Naik et al., 2004; Sindelarova et al., 2014). Maxima in isoprene emissions correlate with El Niño events (2002/2003, 2004/2005, 2009/2010, and the 2014–2016), and minima with La Niña episodes in 2007–2009 (NOAA ONI v5, https://origin.cpc.ncep.noaa.gov). This variability is only weakly dependent on the choice of LC dataset. Besides the differences between long-term trends of the emissions from the three simulations, the year-to-year relative changes in emissions are very similar. At regional scales, we find that LCC can drive isoprene emission trends as it is the case, for instance, in Paraguay, Madagascar and Sierra Leone (**Table 4**).

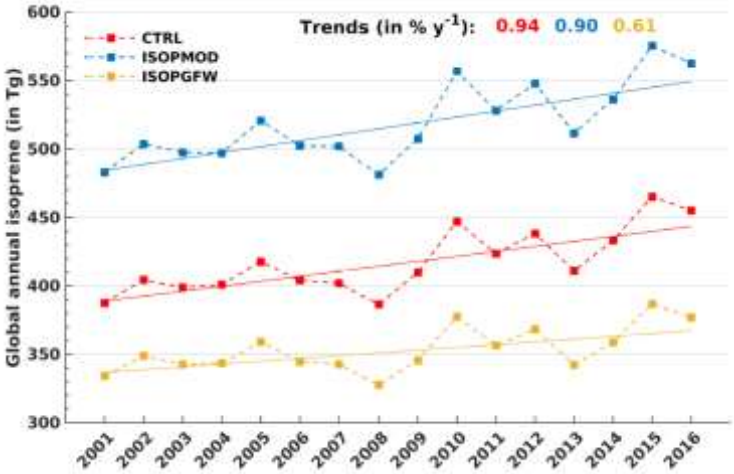

Figure 9: *Time series of global annual isoprene emissions from the CTRL (based on static CLM LC map), ISOPMOD (based on MODIS LC maps), and ISOPGFW (based on GFWMOD LC maps) simulations.*

Table 4: *Isoprene trends in simulations from (i) CTRL, using CLM map and (ii) ISOPGFW, using GFWMOD maps. In CTRL, isoprene trends are mainly driven by temperature and solar radiation. However, ISOPGFW accounts for the impact of both climate variability and LC changes. The effect of LCC on emission trends can be estimated from the differences in trends between the ISOPGFW and the CTRL simulations and is shown in brackets in bold.*

	Annual isoprene trends in % yr^{-1}	
	CTRL	**ISOPGFW**
Brazil	0.9	0.4 (-0.5)
Paraguay	0.6	-0.9 (-1.5)
Indonesia	1.1	0.5 (-0.6)
Malaysia	-1.7	-2.2 (-0.5)
RD Congo	2.5	2.1 (-0.4)
Angola	1.3	0.6 (-0.7)
Madagascar	0.4	-0.3 (-0.7)
Sierra Leone	-0.2	-1.1 (-0.9)

4.1.4. Evaluation with OMI HCHO observations

Three global simulations with the IMAGESv2 model are performed over 2005–2016, using the CTRL, the ISOPMOD and the ISOPGFW emissions; these emissions are described in the previous section, except that the inhibition effect of CO_2 parameterised following Possell and Hewitt (2011) is now taken into account. Although very uncertain, its inclusion is motivated by its substantial effect on isoprene trends, which improves the agreement with OMI HCHO trends.

The interannual variability in seasonally averaged modelled HCHO columns correlates very well with the OMI data, as shown in **Fig. 10** which displays the global distribution of the correlation coefficient of observed and calculated (using the CTRL isoprene emissions) seasonally averaged HCHO columns. In tropical regions, the averages are taken over June–July–August (JJA) for the northern tropics (0–30◦ N) and February–March–April (FMA) for the 0–30◦ S band, corresponding to months with usually minimal biomass burning activity. At extra-tropical latitudes, the seasonal averages are calculated over the summer months, when biogenic emissions and HCHO columns are the highest. High and statistically significant correlation coefficients ($R > 0.8$) are found over most vegetated areas where BVOC emissions are the dominant source of HCHO. This result essentially validates the modelled response of BVOC emissions to short-term meteorological variability (Stavrakou et al., 2018). Whereas the impact of biomass burning on the correlation was mitigated in tropical areas due to the choice of the averaging period the high correlation of modelled and OMI columns in the boreal regions of Canada and Siberia is partly due to the impact of fire activity on HCHO. Nevertheless, even at those latitudes, the interannual variability in biogenic emissions contributes substantially to the correlation with OMI data.

Certain forested regions exhibit positive but relatively low correlations, such as Ivory Coast, South China, and New Guinea, for unclear reasons. Negative or very low coefficients are found in arid and semi-arid regions such as northern Africa, the Middle East, South Africa, Texas, Arizona, northern Mexico, and western Australia. Although this poor agreement might be partly due to a relatively low HCHO signal and low biogenic emissions (e.g. over Sahara), the omission of a soil water stress factor in the parameterisation of biogenic isoprene emissions likely contributes much to the discrepancy. The effect of LCC has little impact on correlations, with changes within the ± 0.1 range (not shown),

indicating that interannual variability in isoprene and HCHO is dominated by meteorological variability, whereas LCCs play only a minor role.

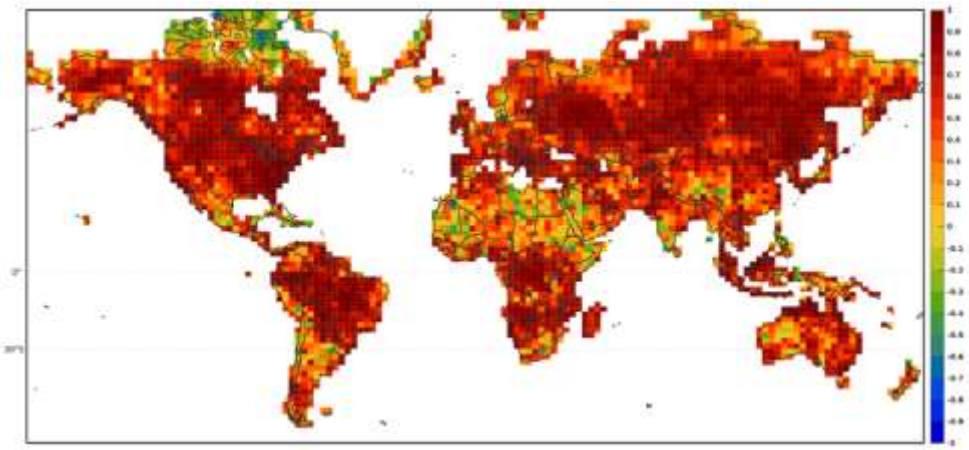

Figure 10: *Pearson's coefficient of correlation between the observed evolution of seasonally averaged HCHO columns during 2005–2016 and the model-calculated values (using CTRL simulation). The seasonal averages are calculated over the months of June–August in the Pearson's coefficient of correlation between the observed evolution of seasonally averaged HCHO columns during 2005–2016 and the model-calculated values (using CTRL simulation). The seasonal averages are calculated over the months of June–August in the Northern Hemisphere (>0°N), February–April in the 0–30° S latitudinal band, and December–February below the 30th parallel. The stippling represents the statistically significant correlation coefficient (p <0.05).*

4.1.5. Recommendations

Although remote sensing is a tool of choice for constraining LC in biogenic emission models, our study casts light on the high uncertainties in the calculation of isoprene emissions associated with the representation of PFTs from satellite-based LC products. Though, overall, our study indicates that the continuous TC fields at fine resolution provided by the GFW database are our preferred choice for constraining in biogenic isoprene emission models.

4.2. Space-based VOC emissions using OMI HCHO data (WP3)

4.2.1. Introduction

This study is motivated by literature that documents the presence of biases in spaceborne HCHO (De Smedt et al., 2021; Vigouroux et al., 2020; Zhu et al., 2020). Acknowledging the potentially important consequences of such biases on TD VOC emission estimates based on spaceborne HCHO columns, **within the framework of WP2, we aim** (i) to **assess the biases of HCHO columns** from a recent OMI retrieval (De Smedt et al., 2018) using both FTIR data and a methodology similar to Vigouroux et al. (2020) and in situ aircraft measurements from several campaigns in the US, and (ii) to investigate **the impact of those biases on TD NMVOC emissions** based on OMI data.

The complete study was presented in a peer-reviewed publication in *Atmospheric Chemistry and Physics* (Müller et al., 2024).

4.2.2. OMI HCHO bias characterisation

Overall, we find that both FTIR and aircraft comparisons show that **OMI underestimates high columns and overestimates low columns**.

Due to the relatively high noise of OMI data (compared to TROPOMI), we use monthly means of coincident pairs to derive a robust linear relationship between OMI and FTIR columns with a co-location distance of 50 km and within 3 h of the OMI overpass. The scatter plot of the coincident monthly-averaged FTIR and OMI columns is shown in **Fig. 11.** The comparison of monthly means shows a correlation coefficient of 0.67. The linear regressions of OMI and FTIR data columns give

$$\Omega_{OMI} = 0.659\,\Omega_{FTIR} + 2.02\ \times 10^{15}\ \mathrm{molec.\,cm^{-2}}$$

where Ω_{OMI} and Ω_{FTIR} are the HCHO columns (molec. cm^{-2}) from OMI and FTIR, respectively. The regression yields a positive OMI constant bias (intercept of $2.02\ \times 10^{15}\ \mathrm{molec.\,cm^{-2}}$) and a negative OMI proportional bias (slope of 0.659). The positive OMI bias for clean sites and negative bias for polluted sites is similar as for TROPOMI validation (Vigouroux et al., 2020). We tested alternative choices for the co-location distance: a higher value (100 km instead of 50 km) degrades the correlation and yields a slightly lower slope (0.63) than the reference regression. Shorter distances (e.g., 20 km) lead to an excessively low number of OMI pixels to be averaged ($\ll$10) and therefore to poor correlation with FTIR.

To evaluate the OMI data against aircraft in situ measurements, we use the MAGRITTE model as transfer standard. The linear regression of OMI and aircraft-based columns gives very similar results to the regression that was inferred using FTIR columns:

$$\Omega_{OMI} = 0.651\,\Omega_{airc} + 2.95\ \times 10^{15}\ \mathrm{molec.\,cm^{-2}}$$

where Ω_{airc} is the HCHO columns from aircraft-constrained model simulations. The slopes of the two regressions are almost identical, but the FTIR-based fit has a smaller intercept and suggests a larger negative bias of high OMI columns than the aircraft-based evaluation. The OMI bias depends on the magnitude of the column but likely also on other parameters. In absence of additional information, we adopt a bias-correction of OMI data based on both aircraft and FTIR data. The **bias-corrected columns ($\boldsymbol{\Omega_{OMI,BC}}$) are calculated by**

$$\boldsymbol{\Omega_{OMI,BC} = \left(\Omega_{\mathrm{OMI}} - 2.5\ \times 10^{15}\right)/0.655}$$

The results of the VOC optimised emissions on simulated HCHO concentrations constrained with $\boldsymbol{\Omega_{OMI,BC}}$ are shown in **Fig. 12** and **13**.

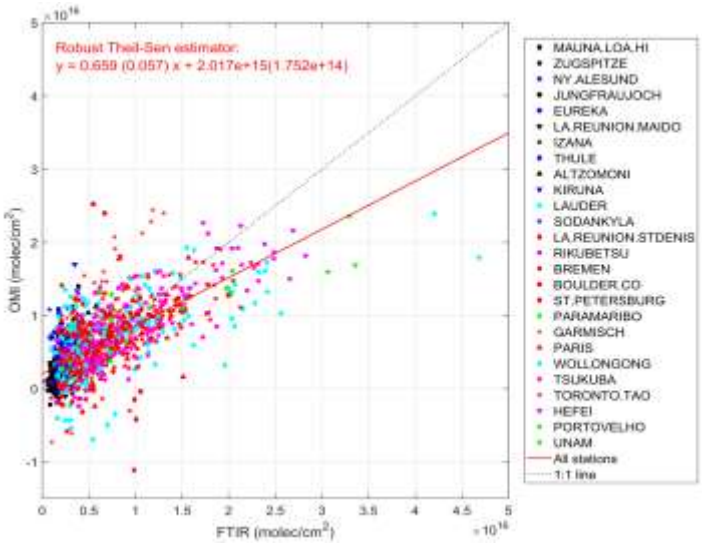

***Figure 11**: Scatter plot of co-located OMI and FTIR HCHO monthly columns over 2005–2017. The red line represents the Theil-Sen regression. Its slope and intercept (their 1σ errors between brackets) are given in red.*

The optimisation reproduces very well the vertical profile shape of HCHO mixing ratios for all campaign datasets, as seen in **Fig. 12**. While panels (a)–(d) display the campaign-averaged profiles for the datasets used in the emission inversion, **Fig. 12(e)** shows the profiles for the SENEX campaign which took place in 2013 but was not used as constraint in the inversion. Although the observed profile shape is correctly simulated by the model, the overall agreement is significantly lower for this campaign (−22 *%* bias) than for the campaign datasets used in the inversion. Given the significant overlap of the SENEX and SEAC^{4}RS spatial coverages, the underestimation of SENEX HCHO by the model suggests a shift of the summertime biogenic VOC emission peak towards spring, since SENEX and SEAC^{4}RS were conducted (primarily) in June and August, respectively.

For the campaigns used in the inversion, a regression of the observed and simulated optimised HCHO column densities yields a slope of almost 1 and a correlation coefficient of 0.93 (**Fig. 13(a)**). In contrast with this, **Fig. 13(b)** shows that the OMI HCHO columns are significantly biased with respect to co-located columns calculated using the optimised model distributions. **High OMI HCHO columns (>12×10^{15} cm^{-2}) are underestimated by up to ca. 20 *%*, whereas low columns (<8×10^{15} cm^{-2}) are generally overestimated.** This underestimation of high columns is relatively similar with the slight underestimation (12 *%*) of OMI HCHO columns from the BIRA V14 product (De Smedt et al., 2015) against SEAC^{4}RS HCHO data determined by Zhu et al. (2016). The underestimation of high columns is also qualitatively consistent with the mean OMI bias of −17 *%* derived by Boeke et al. (2011) for OMI columns (>5×10^{15} cm^{-2}), based on comparisons with several aircraft campaigns conducted in 2008.

The bias correction results in an enhancement of columns above ~7×10^{15} cm^{-2} and a decrease in columns below that value. The contrasts between high- and low-emission regions will therefore be strengthened by the bias correction. The scatter plots of **Figs. 12** and **14** show a large dispersion for low columns, indicating high uncertainty in the bias correction. For this reason, the optimisation results should be considered with caution in low-column areas.

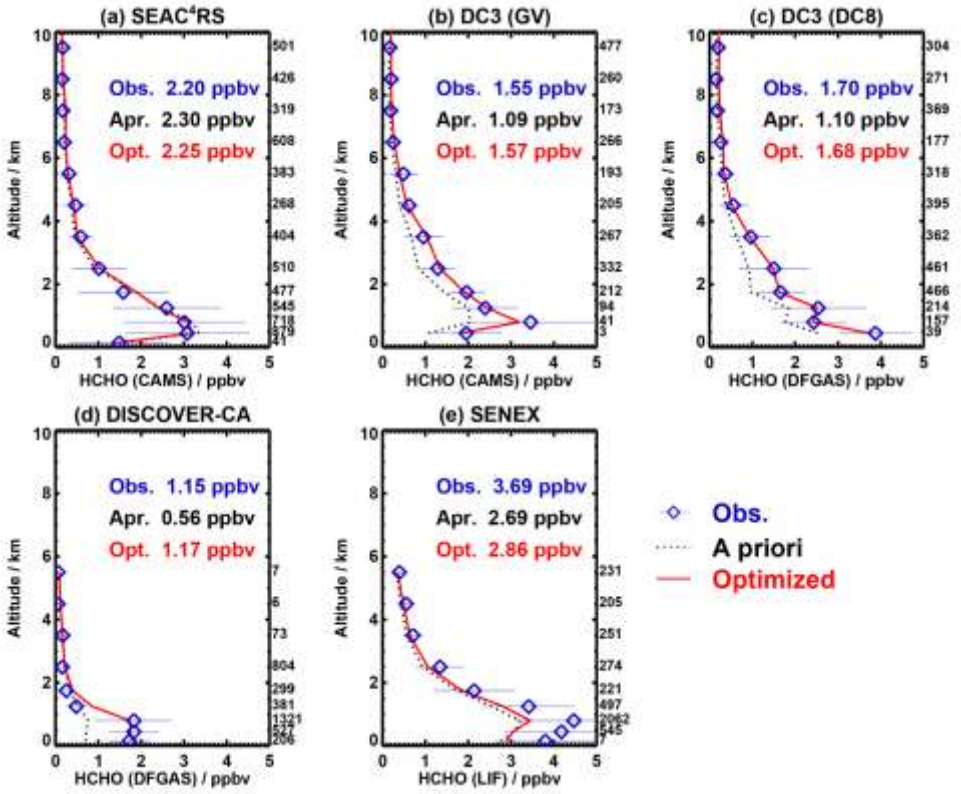

Figure 12: *Measured and modelled profiles of HCHO mixing ratios over land (in ppbv) for (a) SEAC4RS, (b) DC3 (GV), (c) DC3 (DC-8), (d) DISCOVER-AQ California and (e) SENEX. The averaged measured and modelled (a priori and optimised) mixing ratios below 4 km altitude are given for each dataset. The number of observations is given to the right of each plot. The boundaries of the altitude bins are 0, 0.3, 0.6, 1, 1.5, 2, 3, 4, 5, 6, 7, 8, 9 and 10 km. The error bars represent the standard deviation of the measurements.*

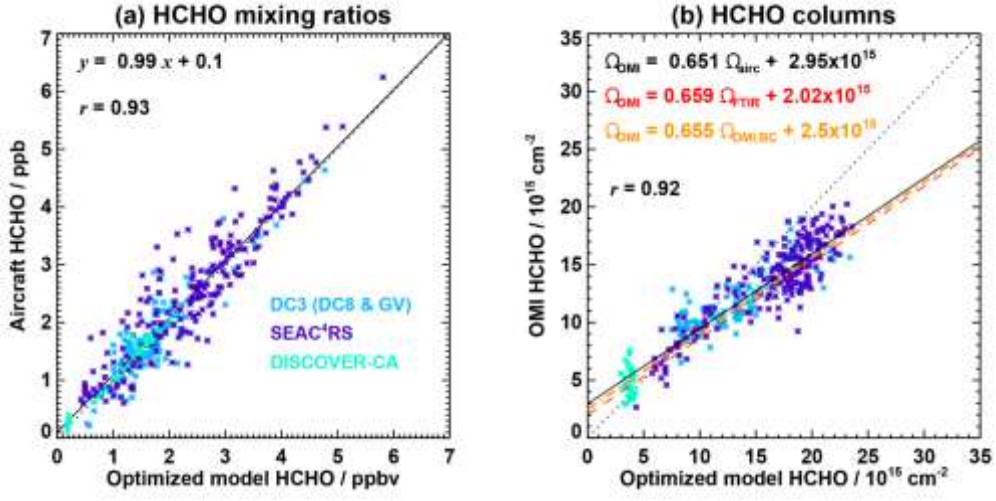

Figure 13*: Scatter plots of (a) modelled and observed HCHO mixing ratios (daytime, below 4 km altitude) from three aircraft campaigns (DC3, SEAC⁴RS and DISCOVER-AQ California) and (b) modelled and OMI total HCHO columns at the same model pixels as in panel (a). The modelled values are constrained by the aircraft measurements through an emission optimisation as described in the main text. The correlation coefficient and regression parameters using the Theil-Sen estimator are given in each panel (black font) and shown as a solid black line. The slope and intercept of the regression of OMI columns vs. FTIR data are given in panel (b) (red font) and shown as a dashed red line. The adopted bias correction (relationship between OMI columns Ω_{OMI} and bias-corrected columns $\Omega_{OMI,BC}$) are also given (orange) and shown as the dash-dotted orange line.*

4.2.3. Top-down VOC emission estimates from bias-corrected OMI HCHO

Figure 14 displays the distribution of the emission ratios (optimised flux/a priori flux) per emission category (biomass burning, anthropogenic, biogenic) for both optimisations, with or without the bias correction on OMI HCHO columns (2011–2017 average). The mean annual emission totals in tropical regions are given in **Table 5** for bias-corrected optimisation averaged over 2005–2017.

Over 2011-2017, the optimised global total emissions for the different categories (**Table 5**) are estimated at 87 Tg yr^{-1}, 451 Tg yr^{-1} and 192 Tg yr^{-1}, for biomass burning, isoprene and anthropogenic emissions, respectively, which represents a change of +13%, +25% and -10% with respect to the VOC optimised emissions with no bias correction. **The bias correction of OMI columns has thus a large impact on the inferred TD emissions, especially for the biogenic emission category**, which is the dominant contribution to HCHO columns over continental regions (Stavrakou et al., 2009). Without bias correction, global isoprene emissions are decreased from 430 Tg yr^{-1} in the a priori from MEGAN to 362 Tg yr^{-1} in optimisation with no bias correction (i.e., a 16 *%* decrease), whereas optimisation with bias-correction increases those emissions by about 5 *%* to 451 Tg yr^{-1} over the 2011–2017 period. The TD global isoprene emissions from the optimisation with bias correction (445 Tg yr^{-1} for 2005–2013) are a factor of 1.64 higher than the TD emissions derived by inverse modelling of OMI data by Bauwens et al. (2016) (272 Tg yr^{-1}). Note that our a priori (MEGAN) emissions are also higher than in Bauwens et al. (2016), especially over Australia and Africa, due to the soil moisture stress impact that was accounted for by Bauwens et al. (2016) but not in our study. The bias correction of OMI data applied in this work explains only a part (factor 1.25) of the large discrepancy between the TD estimates. The main reason for the remainder is the different OMI retrieval (BIRA-V14) (De Smedt et al., 2015) used as constraint in Bauwens et al. (2016). We found that QA4ECV columns are typically higher than the V14 product by 10 %–50 % over continents, and by up to 80 *%* in parts of southern Africa.

The impact is strongest over south Asia (+43 *%* difference) and over Africa (almost +30% difference) (**Fig. 14**). Over South America, the bias correction leads to optimised isoprene emissions (125.9 Tg yr^{-1}) that are about 17% higher than optimised emission with no correction (107.6 Tg yr^{-1}) for 2011-2017. **OMI-based optimisation shows that bottom-up isoprene emissions are overestimated in particular over South America but underestimated in SH Africa and South Asia by a factor of 1.73 and 1.35.** Regarding pyrogenic emissions, changes with respect to a priori emissions are mainly located in Africa with a small decrease in the NH from 16 to 13 Tg and the largest increase in from 26 to 30 Tg in the SH. The optimisation leads to little changes in a priori anthropogenic emissions in tropical regions (**Fig. 14** and **Table 5**). Overall, the optimisation shows that that the largest changes with respect to a priori inventories are found in SH Africa due to rises in both biogenic and pyrogenic emissions.

4.2.4. Recommendations

Given the improved agreement between modelled HCHO distributions and both aircraft and FTIR observations, we recommend the use of bias-corrected satellite HCHO column densities in inverse modelling frameworks. Applying this correction leads to optimised global isoprene emissions that are approximately 25% higher than those derived without correction, underscoring its significant impact. These updated emission estimates also show good consistency with recent values derived from spaceborne isoprene columns retrieved by the CrIS sensor.

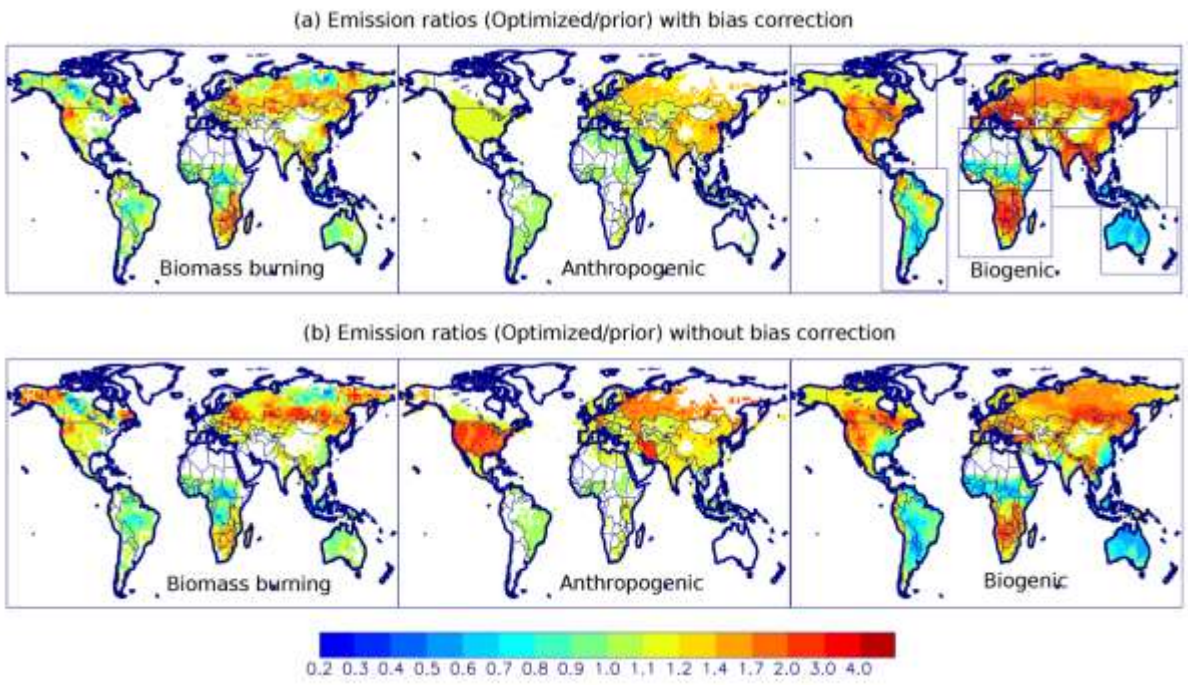

Figure 14: *Ratios of TD emissions to a priori emissions (2011–2017 average) for biomass burning VOCs (left panel), anthropogenic VOCs (middle) and biogenic VOCs (right) for optimisations (a) constrained by bias-corrected columns, and (b) constrained by uncorrected columns. Pixels with very small emission changes (< 1 %) are left blank. The regions used for calculation of total emissions given in Table 1 are shown as boxes on the top right panel.*

Table 5: *Mean a priori and optimised emission estimates (Tg yr^{-1}) per source category for different tropical regions. Regions are defined in* ***Fig. 14****. The means are taken over 2005-2017. NH: Northern Hemisphere; SH: Southern Hemisphere.*

	South America	NH Africa	SH Africa	South Asia
Biomass burning NMVOC emissions				
A priori	15	16.3	25.6	14.4
Optimised	12.5	12.7	30.2	12.4
Isoprene emissions				
A priori	149	85	44	39
Optimised	129	77	76	53
Anthropogenic NMVOC emissions				
A priori	12.6	39.4	11.8	52.2
Optimised	11.5	34.8	12.8	59.8
Total NMVOC emissions				
A priori	176	141	82	106
Optimised	154	128	120	126

4.3. Top-down inventories of VOC and NO_X in the Tropics (WP 2 & 4)

The **objective of WP2 and WP4** is t**o derive TD inventories of natural emissions: nitrogen oxides (NO_X) from soils and lightning (WP2), and isoprene emissions in the Tropics (WP4).** These inventories are then assessed against independent observational data.

In this project, we derive emissions at a 0.5° spatial resolution over Africa and South America for the year 2019, using a two-species inversion framework described in Sect. 3.3.3. To evaluate the robustness of the results over the African domain, we conducted a series of sensitivity inversions as defined in Sect. 3.3.3. The main tasks include: (i) compiling independent observational datasets, (ii) configuring the inversion system, conducting chemistry-transport model simulations, and performing the emission inversions, and (iii) evaluating the TD emissions. A key deviation from the original project plan is the use of NO_2 and HCHO columns in the two-species inversion, instead of HCHO and satellite-derived isoprene columns from the CrIS instrument (Wells et al., 2022). The satellite isoprene data are now used solely for evaluation purposes.

4.3.1. Introduction

Nitrogen oxides play a major role in tropospheric chemistry through their impact on ozone and OH distributions. Whereas anthropogenic NO_X emissions are dominant globally, natural sources from soil and lightning are responsible for ca. 30 % of the total global emissions into the atmosphere. They contribute for even a greater share in remote environments; the impact of lightning is mostly limited to the middle- and upper-troposphere. Both sources are a major source of uncertainty in models: global estimates for lightning range from 1.3 to 6.6 TgN/yr (Murray, 2016) and from 4 to 34 Tg N/yr (Steinkamp and Lawrence, 2011; Yan et al., 2005) for soils. Moreover, the Tropics contribute for about 80% to the global total emissions of biogenic VOCs due to the favourable environmental conditions and the widespread presence of broadleaved trees. Given the intricate interplay between NO_x and VOCs through the NO_x-HO_x-VOC feedback, we design and test a novel inversion setup relying on a concomitant use of HCHO and NO_2 satellite observations in order to optimise both VOC and NO_x emissions.

The complete study for Africa was presented in a peer-reviewed publication in Atmospheric Chemistry and Physics (Opacka et al., 2025).

4.3.2. Top-down VOC and NO_X emissions over Africa

Results on HCHO and NO_2 columns: To evaluate the results of the optimisation, we first evaluate HCHO and NO_2 columns before (a priori) and after the optimisation (STD inversion) with TROPOMI column densities. As expected, the optimisation leads to a better agreement of modelled HCHO and NO_2 column densities. Over land, the domain-averaged MAGRITTE a priori NO_2 columns (0.55×10^{15} molec. cm^{-2}) showed a relatively large initial bias of -29.2% in NO_2 columns with respect to annual average TROPOMI NO_2 columns (~0.74×10^{15} molec. cm^{-2}) that was further reduced to 0.3% after optimisation (**Fig. 15**). The a priori model underestimation is ubiquitous in Africa and is most pronounced in eastern Africa (ca. -30%) and above the rainforest (ca. -40%). These large biases are largely reduced after inversion. Discrepancies still persist, however, in the South African Highveld region, where the annual TROPOMI NO_2 columns reach their highest value over the domain (ca. 14×10^{15} molec. cm^{-2}). This hotspot stems from the strong anthropogenic emission sources located in the Highveld region, i.e. the densely populated cities of Johannesburg and Pretoria, several unregulated large coal power plants, and highly concentrated, energy-intensive industrial facilities in the Mpumalanga region (Matandirotya and Burger, 2021). HCHO column estimated at 9.7×10^{15} molec. cm^{-2} is increased after the optimisation to about 10.8×10^{15} molec. cm^{-2}, thereby reducing the average bias in HCHO columns from -12% to -2% (**Fig. 16**). The a posteriori columns match the bias-corrected HCHO

data south of 8° S very well, where the large negative bias of the a priori simulation (ca. −30 %) is largely reduced as a result of the strong enhancement of isoprene emissions (see **Fig. 19**), as discussed further on. The a priori model overestimation over the Central African Republic and South Sudan gives way to excellent agreement after the inversion, which is realized by strongly reducing the biogenic and biomass burning emissions in these areas (see **Fig. 19** and **20**).

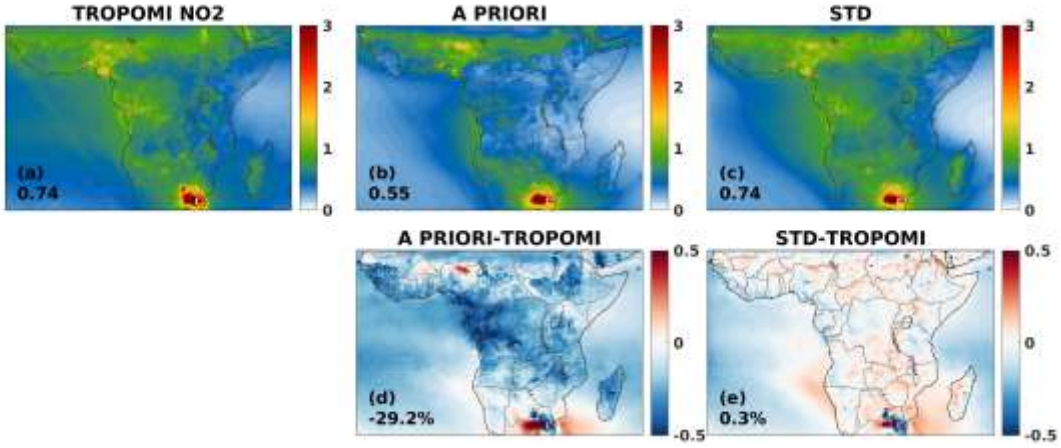

Figure 15: *Annually averaged NO_2 column (in 10^{15} molec. cm^{-2}) in 2019 from TROPOMI, MAGRITTE a priori and the standard inversion (STD; top row) and absolute differences (in 10^{15} molec. cm^{-2}) in annual columns between the model and TROPOMI (bottom row). The mean average column over land and bias (in %) between modelled and TROPOMI columns is given in the bottom left corner of each plot.*

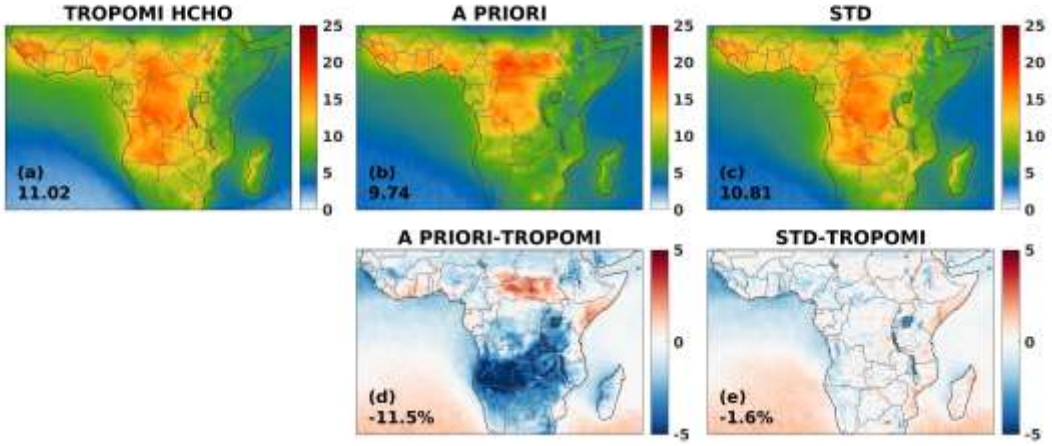

Figure 16: *Annually averaged HCHO column (in 10^{15} molec. cm^{-2}) in 2019 from TROPOMI, MAGRITTE a priori and the standard inversion (STD; top row) and absolute differences (in 10^{15} molec. cm^{-2}) in annual columns between the model and TROPOMI (bottom row). The mean average column and bias (in %) over land between modelled and TROPOMI columns is given in the bottom left corner of each plot.*

Optimized fluxes: The optimisation based on TROPOMI HCHO and NO_2 suggests an increase in natural fluxes compared to BU inventories by +30%, +300% and +30% for soil, lightning and isoprene emissions, respectively (**Table 6**). The satellite data indicate decreases in soil emissions in the Northern Hemisphere and a strong enhancement along the eastern coast of the continent (**Fig. 17(b)** and **(f)**). Higher soil NO_X emissions (up to a factor of 4) are inferred by the STD optimisation in eastern Africa (between Tanzania and the Horn of Africa), moderate decreases (up to 30 %) over the Congo rainforest, where a priori emissions are very low, and a decrease (up to 80 %) in the largest part of northern Africa in the Sahel region.

A good general consistency was found between the results of the different sensitivity inversions, although several inversions stand out. CAMN led to the highest TD soil NO_X (3.1 TgN) and lowest TD lightning NO_X (1.5 TgN) emissions. The single-species inversion SNOX leads to the same total annual soil NO flux as the STD inversion of 2.4 TgN (**Table 6**). However, a higher emission reduction is found by the SNOX inversion in southern Congo and Angola compared to the base inversion (**Fig. 17(c) and (g)**), whereas a soil emission increase is derived over Gabon, where a decrease was found by STD. This difference can be explained by the two opposing effects of isoprene emissions on the lifetime of NO_X due to its impact on OH levels and the formation on organic nitrates that will not be discussed here. Changes in the a priori emission errors (LEER and HEER) are found to have little influence on the top-down results and therefore will not be discussed further.

TD lightning emissions in STD are increased by a factor of 4 in the STD case relevant to the a priori estimate (0.54 TgN). The changes are ubiquitous as seen in **Fig. 18** but the highest fluxes are found in the equatorial region and in western Africa. Note that the inversion with the highest soil NO emissions (CAMN) has the lowest optimised lightning fluxes among all the inversions. The sum of soil and lightning NO_X emissions inferred by the standard and sensitivity inversions is consistently close to ca. 4 TgN, which is 67 % higher than the a priori estimates used in the inversion (2.4 TgN).The relative share of lightning emissions increases from 21 % of the total natural NO_X flux in the a priori inversion to 45 % in the standard inversion, at the expense of soil emissions. This underscores the inherent difficulty in separating their relative contributions to the total column over Africa, where both sources are important.

The bias-corrected TROPOMI data indicate an increase in the annual isoprene fluxes from 125 Tg in the a priori inversion to 165 Tg in the benchmark STD inversion, whereas the range of optimised emissions extends from 61 Tg for the NOBC inversion, for which no bias correction is applied, to 185 Tg in SVOCs, where only VOC fluxes are optimised. In the STD inversion, the isoprene decrease north of the Equator occurs mainly in August with a substantial drop suggested by TROPOMI, while in the equatorial region there is a moderate increase in the annual basis (**Fig. 19**). Most prominently, the distributions show strong emission enhancements in southern Africa, i.e. a factor of 2 or more and a factor of up to 5 locally. The ALBE inversion leads to slightly lower annual isoprene emissions (135 Tg) compared to the base inversion estimate (165 Tg), which is due to the lower a priori total isoprene emissions of the ALBERI inventory (83 Tg, vs. 125 Tg in the a priori of STD) and the lower tree cover in this inventory (Opacka et al., 2021). Finally, the inferred isoprene flux from the SVOC run is 14 % higher than in the standard inversion (SVOC/STD: 185/165). This is attributed to chemical feedbacks, i.e. the influence of NO_X on OH levels and the yield of HCHO from VOC oxidation. More specifically, the overall higher TD natural NO_X emissions from the STD inversion (4 TgN compared to 2.4 Tg in the a priori result in higher modelled HCHO, and therefore relatively lower isoprene fluxes are required to match the observations compared to the SVOC case.

Although the TD biomass burning VOC emissions (**Fig. 20** and **Table 6**) remain close to the a priori estimates, important changes are found in the spatial patterns. Relevant to the a priori inventory (QFED), fluxes are reduced by a factor of 3 over western Africa, the Central African Republic, southern Congo, and Angola and are strongly enhanced in Mozambique, South Africa, and Madagascar (factors of 4–6), whereas moderate increases are derived above Nigeria (a factor of less than 2).

Table 6: *Summary results for TD emission of soil and lightning NO_X (in TgN), isoprene (in Tg) and fire VOC (TgVOC) obtained from the a priori and STD inversion in year 2019, and the change (%) is calculated between the a priori and the STD inversion. The fifth and sixth column provide the emission estimates from single-species inversions (SNOX or SVOC) and the range of emissions from the sensitivity inversions, respectively (**Table 1**).*

Categories	A PRIORI	OPTIMISED (STD)	Change (%)	Single-species SNOX/SVOC	Sensitivity inversions
Soil NO_X (TgN)	1.9	2.4	+26	2.4	2.2-3.1
Lightning NO_X (TgN)	0.5	2.0	+300	2.0	1.5-2.1
Isoprene (Tg)	125	165	+32	188	63-188
Fire VOC (Tg VOC)	36	33	-8	39	26-39

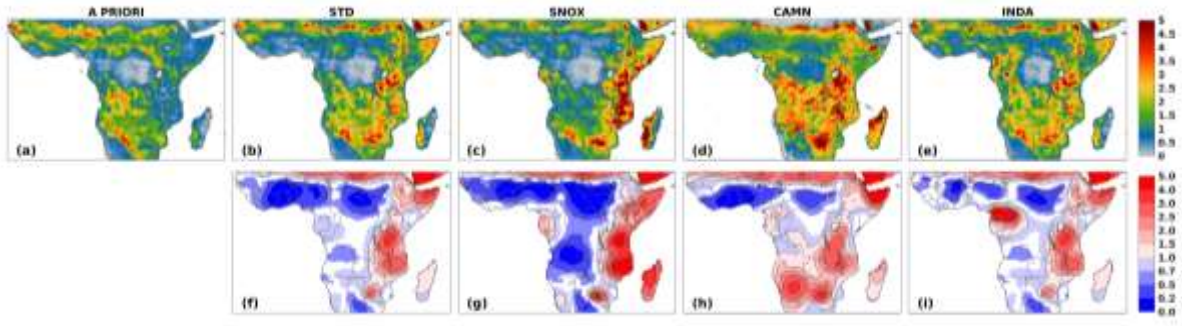

Figure 17: *Annual soil NO_X emissions (top row; 10^{10} molec. cm^{-2} s^{-1}) from the BU inventory (A PRIORI) and TD inventories obtained from different inversions (STD, SNOX, CAMN and INDA, see **Table 1**) and scaling factor (bottom row) obtained by the optimisation that is to be applied on the a priori.*

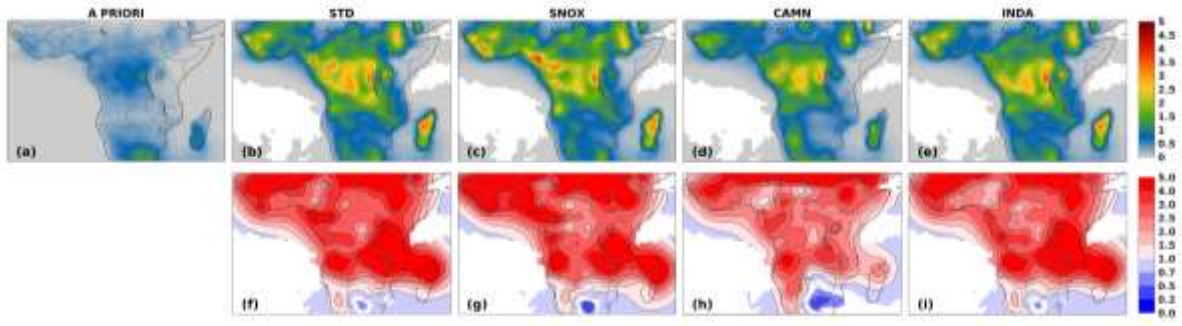

Figure 18: *Same as **Fig. 17**, for annual lighting NO_X emissions.*

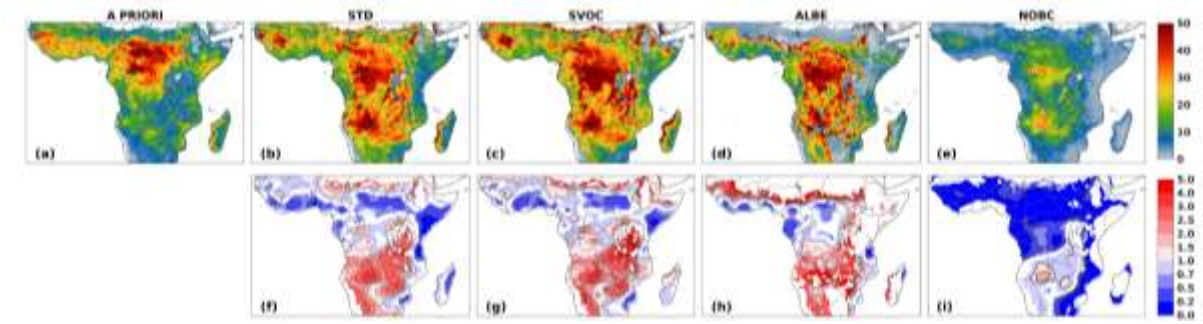

Figure 19: *Annual isoprene emissions (top row; 10^{10} molec. cm^{-2} s^{-1}) from the BU inventory (A PRIORI) and TD inventories obtained from different inversions (STD, SVOC, ALBE and NOBC described in* ***Table 1****) and multiplying factor (bottom row) obtained by the optimisation that is to be applied on the a priori.*

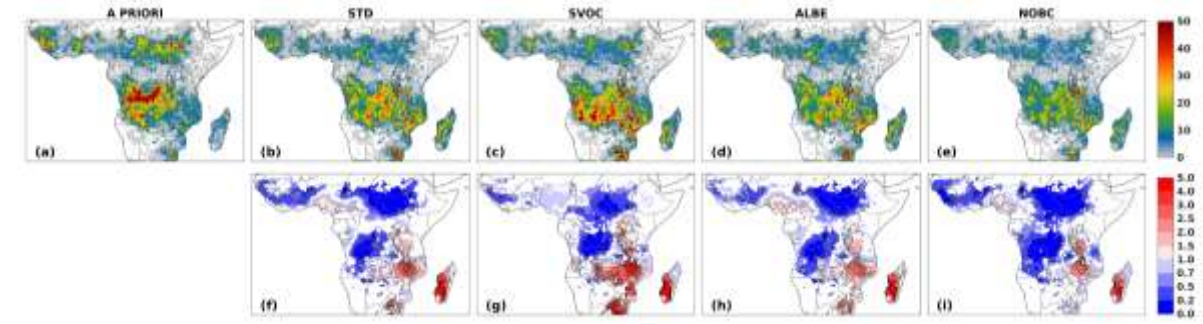

Figure 20: *Same as* ***Fig. 19****, for annual fire VOC emissions.*

4.3.3. Evaluation of optimised fluxes

Here, we present an evaluation of the optimisation against the INDAAF NO_2 mixing ratios, in situ soil NO flux measurements, the satellite-based dataset of upper-tropospheric NO_2 mixing ratios, and isoprene columns of the spaceborne CrIS instrument.

Figure 21 displays monthly surface concentrations of NO_2 (ppb) measured at the INDAAF sites in 2019 (**Fig. 4**), the average during 2015–2020, and the modelled concentrations from the a priori, the STD inversion, and three sensitivity tests (SNOX, CAMN, and INDA).

The principal sources of near-surface NO_X at the INDAAF sites are biomass burning and biogenic soil emissions, except for Bambey and Djougou, which have an urban influence. Overall, the STD optimisation and sensitivity inversions do not depart much from the a priori ones, except for the INDA case, which shows a significant improvement as a result of the use of INDAAF data as additional constraints in the inversion.

The highest NO_2 levels are observed in the dry savannas of Niger and Mali (Agoufou, Banizoumbou, and Katibougou sites) that also exhibit a marked seasonal cycle with two peaks. The average 2015–2020 data show a large standard deviation in Agoufou, and most of the observed variability can be attributed to NO emissions from soils (Adon et al., 2010). However, the a priori and optimised NO_2 surface concentrations (STD, SNOX, and CAMN) show very little monthly variability, and the average mixing ratios are underestimated by factors of 2–3 in comparison to the 2019 measured values in Banizoumbou and Katibougou. In Agoufou, the annual measured surface concentration (1.40 ppb) is 3 times higher than the model and a factor of 6 higher at the June peak (3 and 0.5 ppb). The INDA

inversion suggests that soil NO emissions should increase by factors of 3 and 1.5 on average in May–June–July compared to the 2019 measurements at Banizoumbou and Katibougou, respectively. At the wet savanna sites, Lamto and Djougou, the a priori and optimised NO_2 levels are in overall good agreement with the observations but with a moderate underestimation at Lamto (40 %) in the standard inversion. Optimised NO_2 concentrations from the INDA inversion at Lamto and Djougou agree very well with the observations in terms of both magnitude and correlation. This match is realized by a doubling of the bottom-up soil NO fluxes over the entire year. Finally, the Zoetelé and Bomassa forested sites exhibit similar seasonalities with maxima recorded in February–March, corresponding to the biomass burning season (Adon et al., 2010). On average, surface concentrations in the a priori and optimised models are largely underestimated (a factor of 4 in Zoetelé and a factor of 6 in Bomassa). According to the INDA results, the soil NO fluxes should be increased by factors of 7 and 9 in Bomassa and Zoetelé, respectively, during the wet season (May–November) in order to match the observed surface NO_2 concentrations.

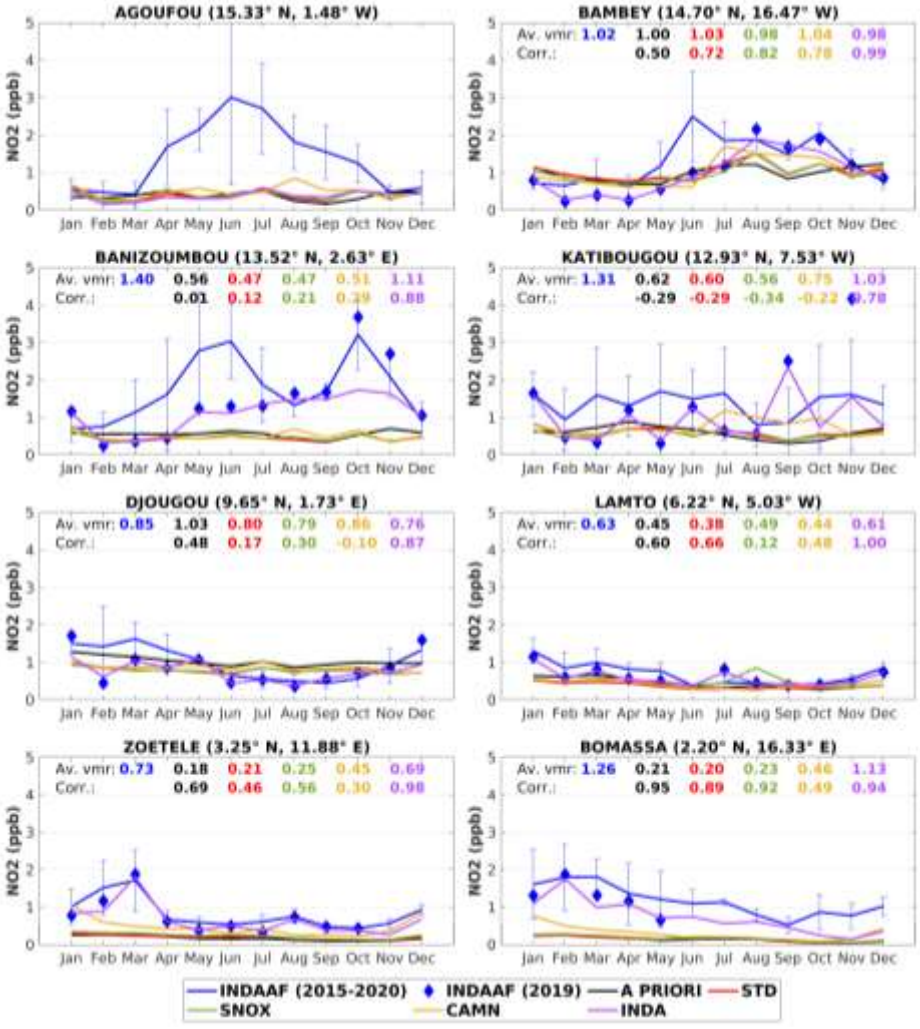

Figure 21: *Monthly surface volume mixing ratios of NO_2 (ppb) for the 2019 measurements (blue diamonds), the average measurement for the 2015–2020 period (blue), and modelled concentrations from the a priori run (black) and the inversions STD, SNOX, CAMN, and INDA. The average volume mixing ratios (Av. vmr; ppb) and correlation are provided as insets and are calculated with respect to the INDAAF 2019 measurements. The vertical bars denote the standard deviation of the 2015–2020 measurements.*

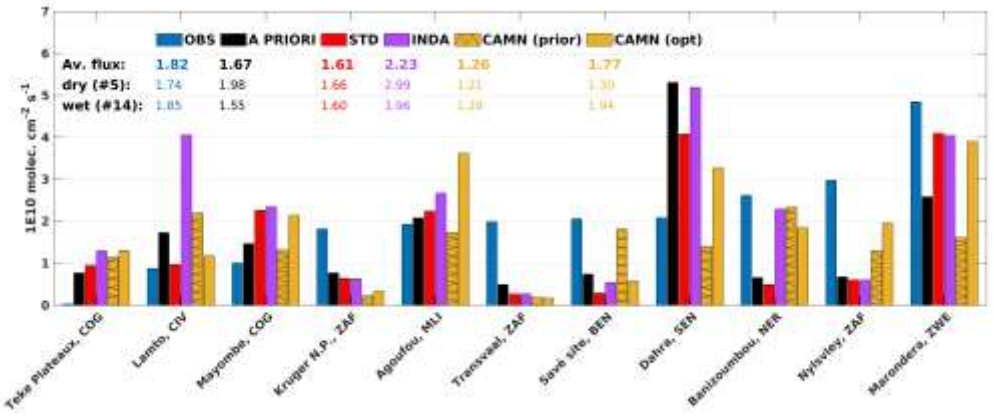

Figure 22: *Average soil NO flux measurements (10^{10} molec. cm^{-2} s^{-1}) from the compilation of* ***Table S1*** *and* ***Fig. 4****. In situ observations are shown in blue, the a priori model in black, and the inversion results in red (STD), magenta (INDA), and orange (CAMN). The a priori CAMN model is shown in hatched orange. The average fluxes (provided inset) are calculated based on the means for all the data over the wet and dry seasons (****Table S1****). The numbers in parentheses denote the number of available data.*

Figure 22 shows the average observed soil NO fluxes at 11 different locations, the corresponding values from the STD and CAMN a priori runs, and the STD, INDA, and CAMN inversions. The a priori and optimised soil NO fluxes from the STD inversion show a slight overall underestimation of about 10 % with respect to the observed all-site average of 1.82×10^{10} molec. cm^{-2} s^{-1}. Despite the relatively good overall agreement of optimised fluxes with respect to the measurements, we observe that the model tends to overestimate the low observed fluxes ($<1 \times 10^{10}$ molec. cm^{-2} s^{-1}) and underestimate the high ones ($> 2 \times 10^{10}$ molec. cm^{-2} s^{-1}), except at Dahra. Large discrepancies are found at both Congo sites, Teké Plateau and Mayombe, where the inferred soil NO fluxes are strongly overpredicted. On average for all of the sites, the STD inversion yields a satisfactory agreement in both the dry and wet seasons, whereas the INDA results overpredict the observations, especially during the dry season. All of the inversions, however, underestimate the fluxes at the southern African sites Kruger N.P., Transvaal, and Marondera, independent of the season.

Several limitations in these comparisons should be acknowledged. First, the TD estimates of soil NO fluxes are derived for 2019, whereas the in-situ data were collected for the 1991–2016 period, which complicates the comparisons because of the high temporal variability of soil NO fluxes. Moreover, the spatial representativeness of the model at 0.5° horizontal resolution with respect to in situ measurements is another issue. An additional limitation lies in the comparison at forested sites because of the canopy uptake of NO_2. Indeed, in situ flux measurements are taken at the soil level, whereas TD inventories provide above-canopy fluxes that are generally lower than the above-soil fluxes. Bottom-up inventories account for this NO_2 uptake by applying a canopy reduction factor that is a highly uncertain parameter. Considering those shortcomings, the good performance of the optimised model regarding the average flux for all the sites gives some confidence in the corresponding soil NO fluxes in Africa.

Figure 23 shows seasonally averaged mixing ratios of upper-tropospheric NO_2 mixing ratios between 180 and 450 hPa derived from TROPOMI NO_2 data averaged over two of the five layers (320–180 and 450–320 hPa) and for 2018–2022, in comparison with the MAGRITTE a priori run and the STD inversion. According to the cloud-sliced NO_2 data, the average UT NO_2 mixing ratio throughout the

year is about 50 pptv and is relatively constant from season to season with a maximal seasonal spread of 20 %, ranging from 45 to 54 pptv.

The inferred STD UT NO_2 mixing ratios display a higher seasonal variation (30–45 pptv) with a maximal seasonal difference of 70%. The optimisation strongly reduces the negative model bias with respect to the average values, from more than 70 % in the a priori run to ranging from ca. −35 % to −17 % in the STD run, depending on the season. Regarding the spatial distribution, the optimised UT NO_2 distribution exhibits a stronger west–east gradient than the observations. Within the latitudinal band 15° S–10° N, the negative bias after optimisation is significantly lower (< 25 %) in the western part than in the eastern part (~50 %). This feature suggests an underestimation of lightning NO emissions in either the eastern part of the Congo Basin or the vicinity of the Horn of Africa and/or long-range transport of NO_X from other regions, particularly oceans. Indeed, emissions over oceans are not optimised, and the LIS or OTD climatology used in the lightning parameterisation might underestimate the flash rate over oceans (Luhar et al., 2021). Despite the uncertainties and remaining biases, the above comparisons support the large increase in lightning NO emissions suggested by the TROPOMI NO_2 data and indicate that an even greater lightning source would be required to match the UT NO_2 measurements.

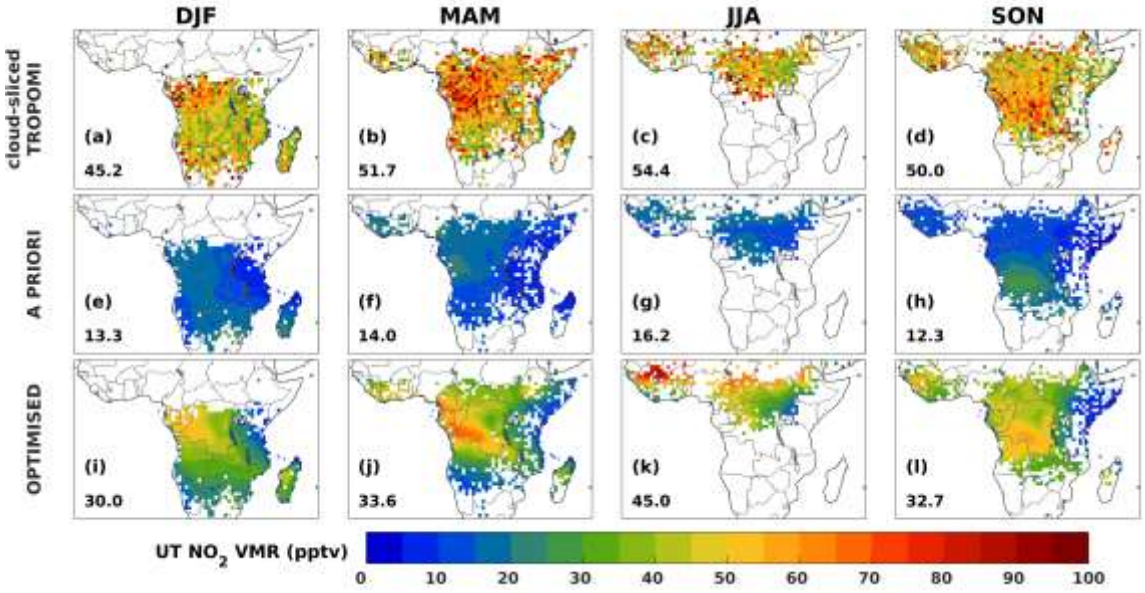

Figure 23: *Seasonal distributions of upper-tropospheric NO_2 volume mixing ratios (pptv) in DJF, MAM, JJA, and SON for cloud-sliced TROPOMI NO_2 (Horner et al., 2024) (a–d), the a priori (e–h), and after the STD inversion (i–l). The blanks are grid cells without cloud-sliced retrievals due to a lack of optically thick clouds over regions of subsidence.*

The annually averaged isoprene columns from CrIS show high values over forested areas in Congo (RDC), in Angola, along the coast of the Gulf of Guinea (5–7 × 10^{15} molec. cm^{-2}), and, to a lesser extent, along the Indian Ocean south of the Equator (**Fig. 24(a)**). The retrieved columns show low values over grassland, shrub, and bare-soil regions, like Namibia and the Horn of Africa, but the gradients are relatively weak over vast regions of moderate fluxes such as the Sahel. The spatial patterns of the a priori model are more contrasted, with a strong hotspot centred on the border between the two Congos (> 15 × 10^{15} molec. cm^{-2}) and much lower columns over much of the rest of Africa (<3 × 10^{15} molec. cm^{-2}). The optimisation based on HCHO and NO_2 data (STD) leads to much improved agreement

with CrIS, as shown by the bias reduction in annually averaged columns over the entire domain, from −33 % in the a priori to −10 % after inversion, and also in the a posteriori spatial distribution of isoprene columns (**Fig. 24(b) and (c)**). The reduction in the isoprene fluxes over the Central African Republic and the emergence of high isoprene levels over Angola, Zambia, and RDC after inversion are fully corroborated by the CrIS data, lending good confidence to the TD estimate.

The single-compound SVOC inversion, which is only constrained by HCHO data, worsens the agreement with CrIS and results in an increase of 42 % in the domain-wide isoprene columns compared to the STD case (**Fig. 24(d)**). This is explained by the higher NO_X emissions derived in STD compared to the a priori, leading to higher OH levels and therefore shorter isoprene lifetimes. Higher OH concentrations also promote HCHO formation from the oxidation. of many precursor VOCs, including methane and isoprene (Marais et al., 2012; Wolfe et al., 2016), thereby leading to overall lower isoprene emissions and columns. The ALBE inversion yields similar results (**Fig. 24(e)**), but the inferred domain-averaged columns are lower than with STD as a result of the lower TD isoprene emissions derived from this inversion (135 and 165 Tg in STD). Not applying a bias correction in TROPOMI HCHO columns in the NOBC inversion results in very low isoprene abundances about 4 times lower than the CrIS yearly average over the studied domain (**Fig. 24(f)**), thereby providing strong evidence of the need to account for biases in satellite HCHO data in the inversions.

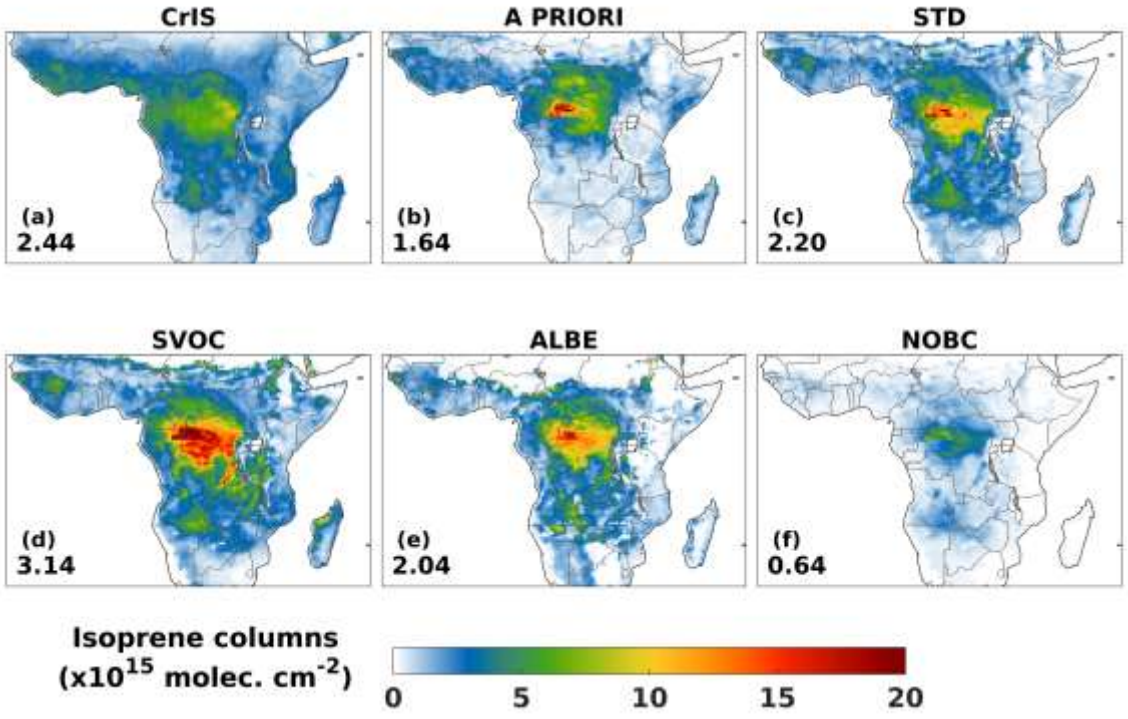

Figure 24: *Spatial distribution of annual isoprene columns (10^{15} molec. cm^{-2}) (a) from a CrIS-based product and (b)–(f) modelled in the a priori and inversions (STD, SVOC, ALBE, and NOBC). The average column over the entire continental domain is provided as an inset (10^{15} molec. cm^{-2}).*

4.3.4. Top-down VOC and NO_X in South America

The annual average of TROPOMI NO_2 columns over the domain is equal to 0.56×10^{10} molec.cm^{-2} after the filtering of fire scenes (**Fig. 25**). Predicted columns are underestimated over the continent by 25%

by the forward simulation and lie much closer to the observations after inversion. Modelled NO_2 columns are mainly enhanced above the forested regions, such as regions 1 and 2 of **Fig. 26** where the bias is strongly decreased from -50% to -20%. The model-data discrepancy occurs all year round except in September-November where the agreement is the best. Locally high columns (3×10^{15} molec.cm^{-2}) are observed above densely populated regions such as Sao Paulo and Rio de Janeiro on the south-eastern coast of Brazil or Caracas in northern part of Venezuela. Over Brazil, the inversion reduces the columns in the northwest of Sao Paulo from 1.5-2 molec.cm^{-2} to 1-1.5 molec.cm^{-2}. Intermediate levels (~1 molec.cm^{-2}) are observed in Caatinga and Cerrado savannas, which are underestimated by the a priori model (**Fig. 25(b)**). For instance, the region 3 in **Fig. 26** shows that the underprediction of columns mainly occurs from January to April and is significantly improved after inversion.

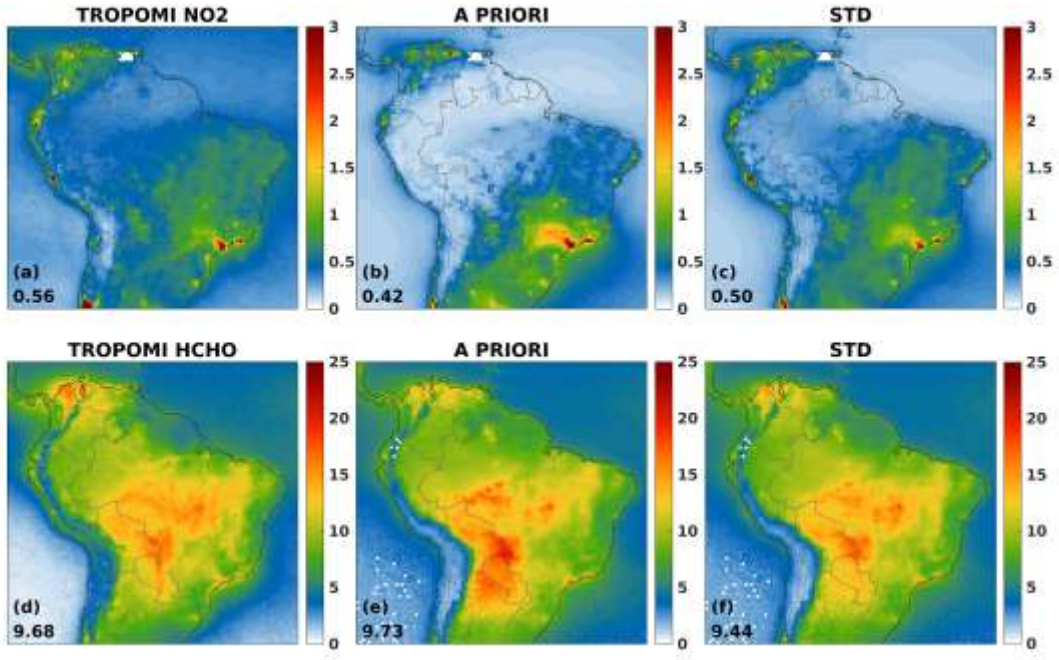

Figure 25: *Spatial distribution of annual NO_2 (top row) and HCHO (bottom row) columns (in 10^{15} molec.cm^{-2}) of TROPOMI ((a) and (d)), a priori model ((b) and (e)) and the STD inversion ((c) and (f)). Average annual column values over land are provided inset.*

TROPOMI HCHO columns exhibit two highly emitting regions (>15-20×10^{15} molec. cm^{-2}s^{-1}), at the Venezuela/Colombia border, the Cerrado and the Pantanal/Chaco region. The high values in the latter region stem from the high fire seasons peaking in August-September (**Fig. 26**, region 4). Lower HCHO columns (<10 × 10^{15} molec. cm^{-2}s^{-1}) are observed over the rainforest. Region 1 and 2, enclosing Amazonia, exhibit a seasonal cycle with two peaks, March and August/September, in the Northern and Southern parts of Amazonia, respectively. The peaks occur during the wet (March) and dry (August/September) seasons with the wet-to-dry transition exhibiting very low levels of HCHO that were attributed to a large-scale isoprene shutdown stemming from leaf flushing (Barkley et al., 2013). On average, the model predicts well the domain-averaged continental HCHO columns in the a priori and after inversion (**Fig. 25**). Despite the bias of continental columns increasing from 0.5% to -2.5%, the distribution after the inversion is improved in the vicinity of the Pantanal region and the north (Columbia-Venezuela). Regional disparities exist though, for example in the Andes region and along

the Amazon River. The model overprediction in the Gran Chaco region by ca. 50% is largely reduced after the inversion. The model locally predicts high HCHO levels in the Roraima state (northern state of Brazil, south of Venezuela and Guyana) that are not detected by TROPOMI. In region 4 (**Fig. 26**), the distribution is improved by the inversion, but biases persist, especially during the May-July transition period. Despite the remaining model biases, the RMSE is reduced over all regions.

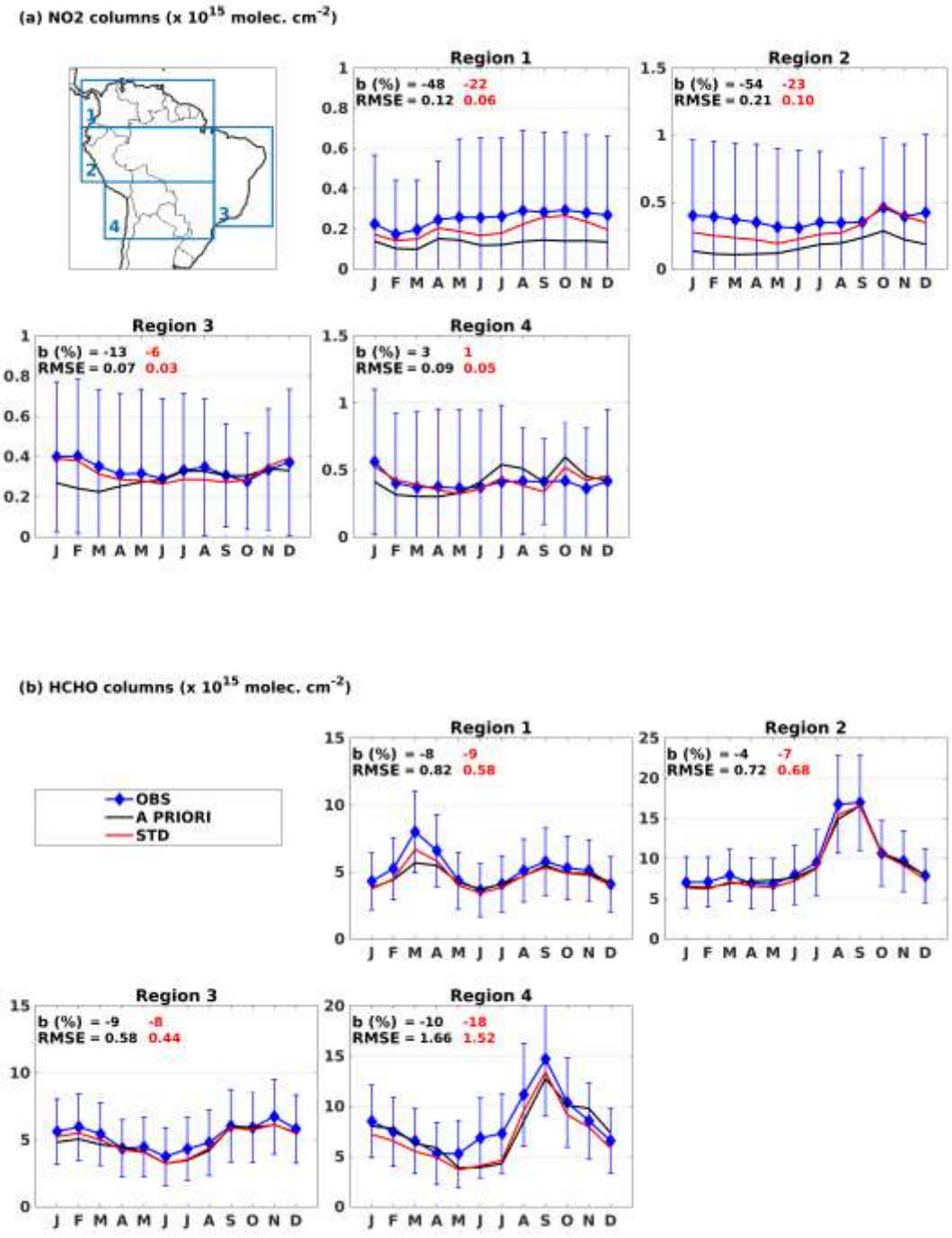

Figure 26: *Time series of continental (a) NO_2 and (b) HCHO columns (in 10^{15} molec.cm^{-2}) over the regions shown inset. TROPOMI NO_2 and bias-corrected TROPOMI HCHO columns (referred to as OBS) are depicted as blue diamonds with their corresponding retrieval errors. The a priori and optimised modelled columns are shown in black and red, respectively. The annual bias (b, in %) and the root-mean square error are calculated for the a priori (black) and the STD inversion (red) and shown inset. Regions are defined as follows: region 1 (0°-12°N, 48°-85°W), region 2 (0-14°S, 48-82°W), region 3 (0°-25°S, 33°-48°W) and region 4 (14-28°S, 48°-76°W).*

The a priori and a posteriori emission estimates are summarised in **Table 7** and their spatial distribution is illustrated in **Fig. 27** along with the emission increments. On average over the total domain, the TROPOMI observations suggest an annual enhancement in NO_X source emissions and a reduction in VOC emissions. The largest changes are inferred for lightning NO_X (+60%) and isoprene (-20%) sources.

***Table 7**: Total NO_X and VOC emissions over the entire domain are shown in TgN and TgVOC, respectively. Three NO_X categories are optimised in the STD inversion, and three VOC categories are optimised in the STD and SVOC inversions. The changes in optimised emissions relative to the a priori values are expressed as percentages.*

	NO_X (TgN yr^{-1})			VOC (Tg VOC)		
	Soil	**Lightning**	**Anthropogenic**	**Isoprene**	**Biomass burning**	**Anthropogenic**
A priori	1.1	0.52	2.31	142.1	14.7	13.6
STD	1.2 (+12%)	0.83 (+60%)	2.43 (+5%)	114.4 (-20%)	13.4 (-9%)	13.2 (-3%)

While the annual total soil emissions are only slightly increased (12%), the optimisation brings substantial changes in the spatial patterns. The a priori exhibits high emissions in savanna ecosystems (3-5×10^{10} molec.$cm^{-2}s^{-1}$) such as Caatinga, Cerrado, Chaco and northern Colombia. Conversely, the bottom-up soil NO fluxes over Amazonia and the Atlantic forest are low in the a priori (typically lower than10^{10} molec.$cm^{-2}s^{-1}$) since they represent above-canopy soil fluxes. Tropical forests have a strong canopy reduction factor (CRF) due to large deposition of nitrogen emitted from soils on leaves within the canopy and a small fraction of the soil emissions that escapes the forest canopy (Ganzeveld et al., 2002; Jacob and Wofsy, 1990; Yienger and Levy, 1995). The distribution of annual soil NO flux after inversion shows large increases in the Caatinga region, by more than a factor of 2 (**Fig. 27**). These increases are accompanied by large flux reductions in the rest of the continent, especially in the regions of Gran Chaco, Cerrado, Pampas, the Atlantic Forest, and more generally over forested regions. In particular, the hotspot (>5×10^{10} molec.$cm^{-2}s^{-1}$) in the HEMCO inventory at the border of the Cerrado and Atlantic Forest is not supported by the TROPOMI NO_2 data, which suggest a strong decrease in this region (**Fig. 27**). In Amazonia, TROPOMI infers negligible changes, which is at odds with current observation-based estimations of soil NO emissions in Amazonia, suggesting increases by a factor of 2-3 at regional scale (Lee et al., 2024; Liu et al., 2016; Wells et al., 2020). Note however that the a posteriori model remains by 20% lower than the observation in the Amazon region, which indicates that a stronger soil NO source would be required (region 2 of **Fig. 26(a)**). The inversion does not favor such a strong increase of the soil source though, most likely because of the low TROPOMI sensitivity to the boundary layer but opts for a strong increase of the lightning source. Indeed, the relative share of soil/lightning over Amazonia is 70/30 in the a priori and 30/70 after inversion. For comparison, the bottom-up soil NO emissions estimate over South America from CAMS-GLOB-SOILv2.4 (Simpson et al., 2023) is higher by 60% than the HEMCO inventory (Weng et al., 2020), used as a priori in this study. Differences between the two datasets are due to different parameterisations used, different emission factors, land-cover characteristics, and the treatment of dry conditions which are increasing in frequency and importance, among others.

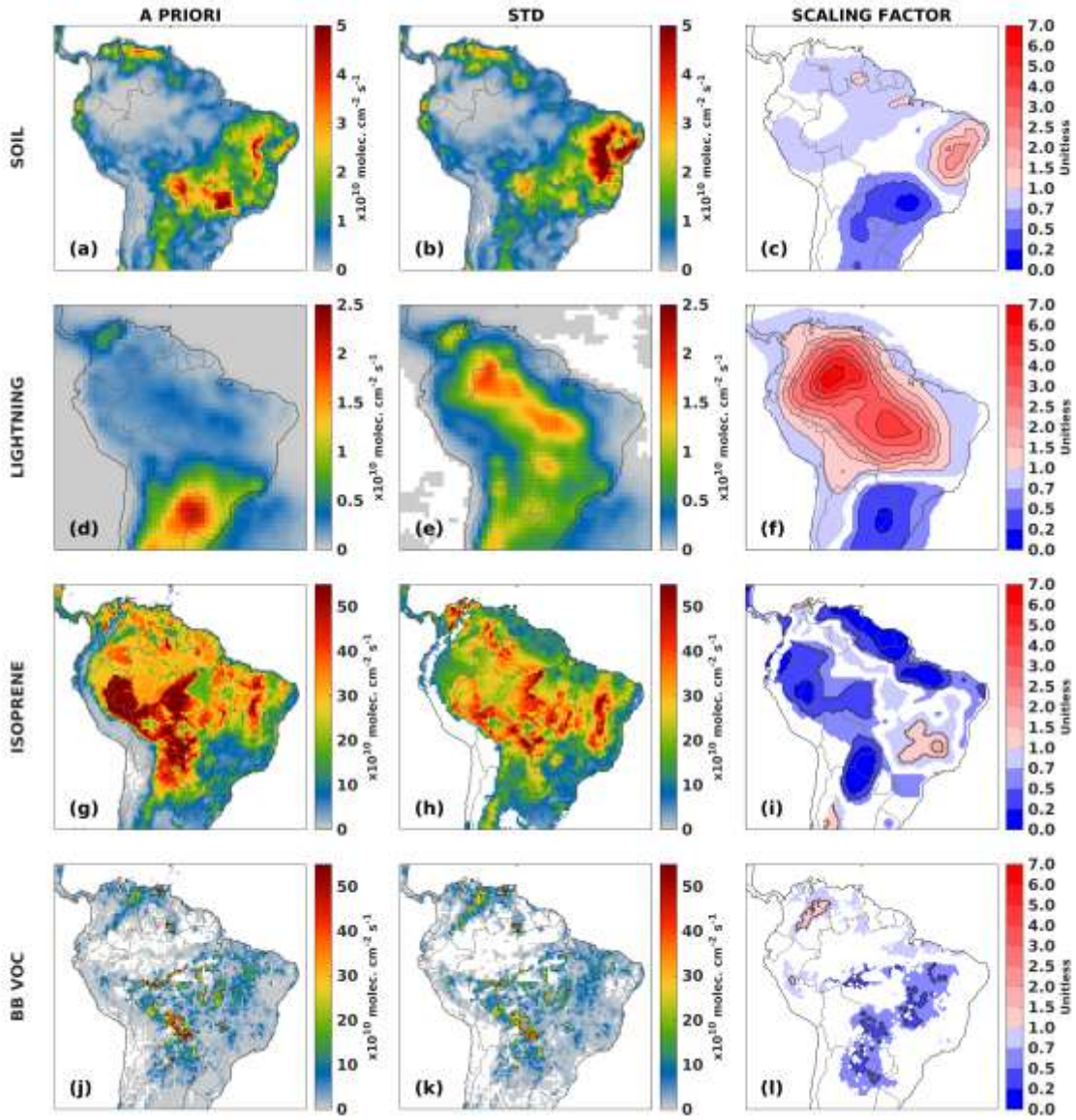

Figure 27: *Spatial distribution of annual a priori model fluxes (left column), the optimised fluxes (middle column) and the scaling factor resulting from the inversion (middle column divided by the left column) are depicted. Emissions of soil, lighting, isoprene and biomass burning VOC (BB VOC) are shown from the first to fourth row, respectively. Emissions are in 10^{10} molec.cm^{-2}s^{-1} and the scaling factor is unitless. Blanks represent regions with scaling factors lying between 0.9 and 1.1 i.e., 10% of change with respect to a priori fluxes.*

The inversion suggests substantial increases in lightning NO emissions, by 60% domain-wide (**Table 7**) and large changes in the spatial distribution (**Fig. 27**). The highest fluxes are inferred over the central part of the continent (up to a 7-fold increase) and the a priori hotspot over Paraguay is strongly decreased (by 80%). The spatial distribution after the optimisation is in closer agreement with the distribution of flash rate density observed during the austral spring (September-November) (Oda et al., 2022).

On average over the domain, the TROPOMI observations suggest an annual reduction of the isoprene emissions by 20% (**Table 7**), and modifications in the spatial patterns. Compared to the a priori, we find lower isoprene fluxes over the high-emitting Amazon rainforest, especially in Western Amazonia, and the Pantanal/Chaco, whereas higher isoprene fluxes are derived in the Brazilian Highlands of the

Cerrado. The decrease over the tropical forests (by 20% over Amazonia) likely indicates that the assumed isoprene flux capacity in the MEGAN model might be overestimated (Guenther et al., 2012a). A strong flux reduction (~80%) is also found along the Northern coast from the high savanna plains of Guianan high- and lowlands to Caatinga, as suggested by the satellite HCHO columns (**Fig. 25**). Note that the a priori inventory (**Fig. 27**) differs considerably in South America in terms of spatial distribution from the ALBERI dataset presented in Opacka et al. (2021) and **Sect. 4.1**. Its spatial patterns are similar to CAMS-GLOB-BIOv1.1 (Sindelarova et al., 2022), and are based to the gridded emission factor distributions, as opposed to the PFT-specific approach used in ALBERI. In particular, the gridded distribution of the emission factors gives rise to the hotspots in South Amazon Basin that are not present in ALBERI. Annual isoprene emissions over South America from other bottom-up inventories were estimated at about 130 Tg (Sindelarova et al., 2022) and 149 Tg (Wang et al., 2024). Using OMI HCHO columns, Bauwens et al. (2016) deduced a reduction of isoprene fluxes in South America, from 141 Tg to 97 Tg. A recent global inversion study constrained by bias-corrected OMI HCHO data (Müller et al. 2024) reported mean isoprene emissions over South America of 129 Tg yr^{-1} over 2005-2017, closer to the a posteriori estimate from this work. We further compare our results with reported isoprene and NO_X estimates by Wells et al. (2020), who performed an iterative optimisation to successively constrain NO_X, based on OMI NO_2, and isoprene fluxes, based on CrIS isoprene columns (**Table 8**). As summarised in **Table 8**, the CrIS-based optimisation leads to isoprene fluxes which are generally higher than in our study. However, the CrIS isoprene columns used in that work were found to be by about 20% higher in South America compared to the updated CrIS ROCR product described in Wells et al. (2022). The latter is used for model evaluation.

Finally, the optimised VOC emissions from biomass burning are decreased by 9% over the domain, with the largest drop taking place in southern Cerrado and Gran Chaco savannas and in Rondônia, and a small increase in Orinoquia (or Llanos) savanna.

Table 8: *Comparison of isoprene emissions (Tg) and total NO_X (TgN) for January, April and July between Wells et al. (2020) and this study over the domain defined in Wells et al. (2020).*

Months	Species	Year 2013 *Wells et al. (2020)*		Year 2019 *This study*	
		A priori	Optimised	A priori	Optimised
January	**Isoprene (Tg)**	10.4	15.4	13.1	9.5
	NO_X (TgN)	0.38	0.90	0.37	0.51
April	**Isoprene (Tg)**	8.4	11.1	10.0	6.9
	NO_X (TgN)	0.30	0.75	0.31	0.89
July	**Isoprene (Tg)**	7.3	9.2	8.1	7.0
	NO_X (TgN)	0.36	0.82	0.33	0.32

Figure 28 depicts comparisons between spatial distributions of isoprene columns from CrIS (Wells et al. 2022), and the corresponding a priori and optimised columns. Annual CrIS isoprene columns are pronounced over the Amazonia rainforest with an average of 8.4×10^{15} molec.cm^{-2}, about twice as high as the domain-wide annual average of 4.7×10^{15} molec.cm^{-2}. A hotspot is observed in the Northern

Amazonian region located between the Amazon River and the Guianan Highland in the vicinity of the Negro-Branco moist forests. One of the most abundant tree species in this region is the sweetgum and the region hosts a large part of the seasonally inundated Igapó forest. The Amazon Basin exhibits a strong seasonal variability in terms of isoprene columns. Indeed, pronounced isoprene levels are observed in March in northern Amazonia, North of the Amazon River (**Fig. 28(d)**) with local columns reaching maxima of 24×10^{15} molec.cm^{-2} and migrates to southern Amazonia, south of the Amazon River, in August (**Fig. 28(g)**). In August we observe three hotspots in Acre state (with rubber trees *Hevea brasiliensis* and Brazil nut trees *Bertholletia excelsa* being dominant), Mato Grosso and a more localised maximum over the Maranhão Bacaçu forests (with dominant trees being the oil palm called Babaçu palm *Attalea speciosa* and the Carnauba palm *Copernicia prunifera*) in eastern Brazil. The migration of the isoprene hotspots from north to south is due to the influence of the ITCZ circulation patterns.

The a priori model overestimates the isoprene column densities in the domain, in particular in the Amazon region by more than 30% annually (**Fig. 28(b)**) and by ~ca. 60% in March and August (**Fig. 28(e, h)**). The a priori isoprene columns exhibit higher densities south of the Amazon, with a strong hotspot in the south-west with an annual maximum of 44×10^{15} molec.cm^{-2}. The optimisation improves the comparison with CrIS in the Amazon, bringing the bias down to -23% annually (+33% in the a priori), 15% in March (61% in the a priori), and 45% (55% in the a priori) in August. Moreover, the top-down spatial patterns are in better agreement with the CrIS patterns for March (**Fig. 28(f)**) due to the reduction in column densities in the southern region of the Amazon. The a posteriori column overestimation might result from NO_X levels being too low in the optimised model, which in turn lead to reduced OH concentrations and a longer isoprene lifetime. At reduced NO_X levels, isoprene columns increase superlinearly with emissions (Wells et al., 2020). The a priori and optimised fluxes underpredict the relatively high columns over forested ecosystems located east of the Amazon box and in northern Venezuela, and the low column densities in regions such as the southern and eastern regions (Cerrado, Atlantic Forest, Caatinga). The a priori exhibits high column densities in the Bolivian Gran Chaco that are not observed by CrIS. The optimisation decreases strongly the annual column densities at this hotspot, except in August. Along the Northern coast, from Bolivia to Caatinga, the optimisation reduces strongly the isoprene columns. In particular, over the Guianan high- and low-lands, the suggested VOC decrease by TROPOMI HCHO (**Fig. 25(d)-(f)**) does not appear to be corroborated by CrIS data. Overall, the evaluation against CrIS data shows a better agreement of the a posteriori model relative to the a priori. The agreement in terms of spatial distribution is also significantly improved.

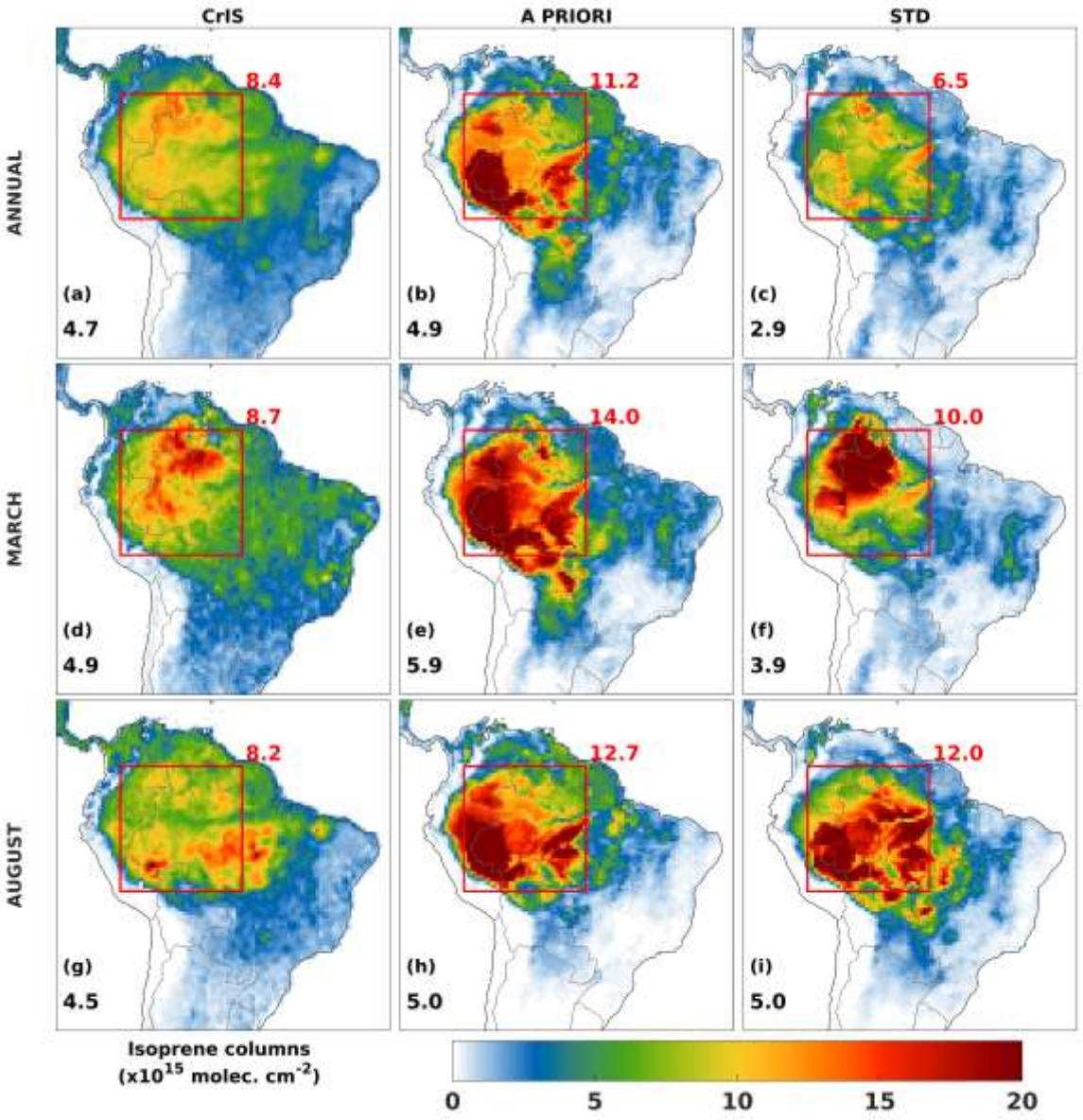

Figure 28: Spatial distribution of isoprene columns (in 10^{15} molec.cm^{-2}) from CrIS (first column), the a priori (middle column) and optimised model (right column). The figure depicts annual (top row), March (middle row) and August (bottom row) columns with the average column over the entire continental domain and the Amazon box (in red) provided inset (in 10^{15} molec.cm^{-2}s^{-1}).

Figure 29 shows monthly HCHO and isoprene columns in 2019 from FTIR measurements at Porto Velho (8.77°S, 63.87°W), Brazil. Measurements are available only during the dry season of 2019. The mean observed HCHO column is 25×10^{15} molec.cm^{-2}, peaking at 40×10^{15} molec.cm^{-2} in August. Average modelled HCHO column shows an overall good agreement although the inversion moderately underestimates the August peak. FTIR uncertainties account for a random (4.5% of the column mean) and systematic (24%) error component that are due to temperature effects and spectroscopy, respectively (Vigouroux et al., 2009). The bias-corrected TROPOMI HCHO column, used as a TD constraint, yields a fairly good agreement with the FTIR data. Porto Velho is uniquely situated for the validation of isoprene, which is detectable primarily over hotspot regions (**Fig. 28**) and these measurements are the first retrievals of isoprene from ground-based FTIR spectra (Wells et al., 2022).

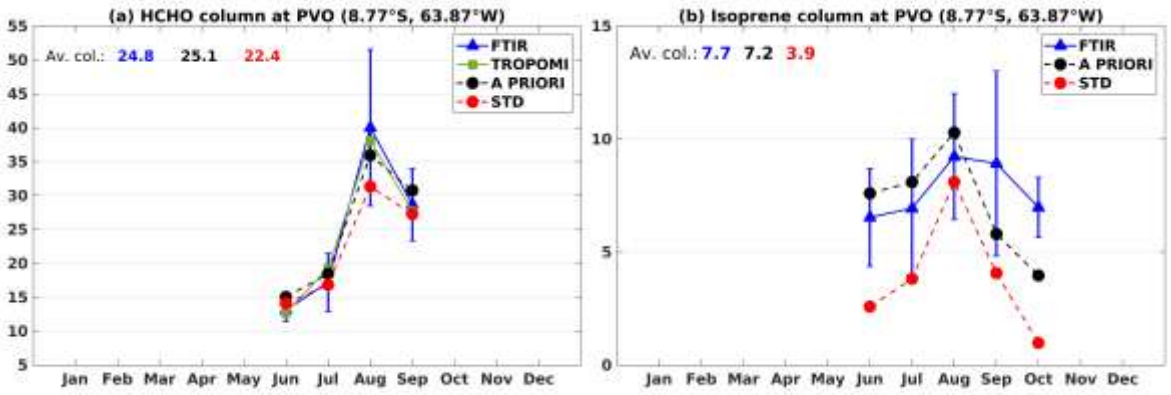

Figure 29: *Time series of monthly tropospheric columns (in 10^{15} molec.cm^{-2}) of (a) HCHO and (b) isoprene at Porto Velho (PVO in **Fig. 4(b)**; 8.77°S, 63.87°W). FTIR measurements are depicted as blue diamonds with error bars representing the standard deviation. Bias-corrected TROPOMI HCHO column is in green. The a priori and optimised modelled columns are shown in black and red, respectively. Average columns are provided inset.*

The a priori modelled isoprene column is close to the FTIR data, with a mean of 7.2×10^{15} molec.cm^{-2} over June to October, compared to the FTIR average of 7.7×10^{15} molec.cm^{-2}. During the wet-to-dry transition period (June-July), a priori isoprene columns are slightly above the FTIR data but within the observational standard errors. As a result of the decrease in isoprene emissions with respect to bottom-up inventory in this region (**Fig. 27**), isoprene columns decrease markedly in Porto Velho. Over the measurement period, the inversion infers a mean of 3.9×10^{15} molec.cm^{-2}, twice lower than the observed mean (**Fig. 29**). The August peak (~9×10^{15} molec.cm^{-2}) is well estimated by the model. However, the a posteriori model suggests a drop in isoprene columns that is too strong compared to the observations for the other months. The optimisation results in decreased isoprene and biomass burning VOC emissions at this site, by about 18% and a factor of 2, respectively. October also marks the peak month for lightning NO_X emissions at Porto Velho, with the inversion causing a factor of 4 increase relative to the a priori. Although the impact of lightning is largest in the free troposphere, it is also significant near the surface, where the bulk isoprene column resides. This impact is caused by the 'C-shaped' profile (Pickering et al., 1998) adopted in the model for lightning emissions, leading to NO_X concentration enhancements near the surface and in the upper troposphere (Ott et al., 2010; Pickering et al., 1998). Disparities in isoprene columns between the model and FTIR isoprene data may be attributed to the combination of isoprene flux decreases and lightning NO_X increases, leading to enhanced OH levels and consequently reduced isoprene columns.

The comparison between soil NO fluxes at the 14 sites for which the in-situ flux measurements were compiled and the modelled results is shown in **Fig. 30**. The mean soil NO flux over all locations is 2.15×10^{10} molec.cm^{-2}s^{-1} but the measurements show a large variability which spans two orders of magnitude, from the lowest value measured at the Ecuador site (0.12×10^{10} molec.cm^{-2}s^{-1}) to the highest at the Park 2 site in Brazil (~10×10^{10} molec.cm^{-2}s^{-1}). The second largest flux (~5×10^{10} molec.cm^{-2}s^{-1}) was measured in Calabazo, Venezuela. The simulated fluxes are on average a factor of two lower than the observations, and the inversion brings only a slight overall improvement. In particular, the a priori soil NO inventory appears to overestimate the low fluxes (<1×10^{10} molec.cm^{-2}s^{-1}) by a factor of 2, whereas it underestimates the high fluxes (>1×10^{10} molec.cm^{-2} s^{-1}) by a factor of 4. The

measurements are higher during the dry season than in the wet season, a feature well captured by the bottom-up and the TD inventory (**Fig. 30**).

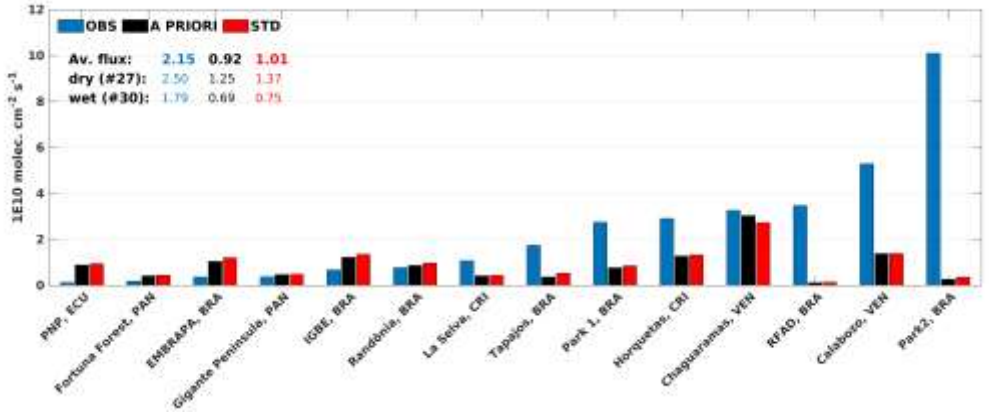

***Figure 30**: Histogram of average soil NO flux measurements (in 10^{10} molec.cm^{-2}s^{-1}) from **Table S2** and **Fig. 4(b)**. Observations are shown in blue, the a priori model in black and the inversion results in red. The average fluxes (provided inset) are calculated based on the means for all data, over wet and dry seasons (cf. **Table S2**). In parentheses are the number of available data.*

The seasonal contrast in modelled fluxes is stronger than in the measurements. It is noteworthy that the TD fluxes represent the above-canopy fluxes that account for the canopy deposition, whereas the measurements correspond to above-soil fluxes. In particular, many measurement sites are located in forested regions where the deposition is high. Earlier studies estimated the CRF in rainforests in the 0.2-0.5 range (Ganzeveld et al., 2002; Jacob and Wofsy, 1990; Yienger and Levy, 1995). Should a CRF of 0.35 be applied to the measurements over forested sites (**Table S2**), the a posteriori underprediction would decrease from 60% to 23%. In addition, by applying a CRF of 0.75 to the measurements at savanna sites (Simpson et al., 2023), the bias would further decrease from -23% to -19%. Due to the lack of observations in the Northeast Brazil, an assessment of the TD flux estimates cannot be performed for the Caatinga region.

Figure 31 shows the spatial distribution of cloud-sliced NO_2 in the upper-troposphere (UT, 180-400hPa) for seasonal concentrations (DJF, MAM, JJA and SON) averaged over 2018-2022, and corresponding modelled UT NO_2 in 2019. The comparison to UT NO_2 concentration shows an important a priori underestimation by about a factor of 4. Annual mean cloud-sliced UT NO_2 is about 45 ppt and exhibit little seasonal variability. The corresponding a priori average is estimated at ca. 10 ppt, and is significantly increased after inversion, ~18 ppt. The remaining bias suggests that the large increase in lightning NO_X emissions is insufficient to match the UT NO_2 densities estimated with the cloud-sliced technique. Multiple factors could play a role in that large negative bias.

Part of the underestimation could stem from the assumption of the vertical distribution in lightning NO_X emissions. The bottom-up inventory uses the approach of Pickering et al. (1998) that places a larger portion of lightning NO_X near the surface in tropical continental regions compared to, for instance, Ott et al. (2010) vertical profile with the majority of lightning NO_X placed in the middle and upper troposphere in a "backward C-shaped" profile. Global and regional CTMs that adopted C-shaped vertical profiles may therefore underestimate the amount of lightning NO_X in the mid- and upper troposphere and overestimate the amount near the surface (Ott et al., 2010). An improvement in the model performance could also be expected after the inclusion of the nitrate and peroxypropionyl

nitrate (PPN) photolysis in MAGRITTE, a process that can regenerate NO_X. Horner et al. (2024) showed that the inclusion of nitrate and PPN photolysis reduced the model underprediction. In particular, this process is most effective at increasing NO_2 in the two layers in the upper troposphere where it is abundant and thermally stable, so photolysis dominates its conversion to NO_2.

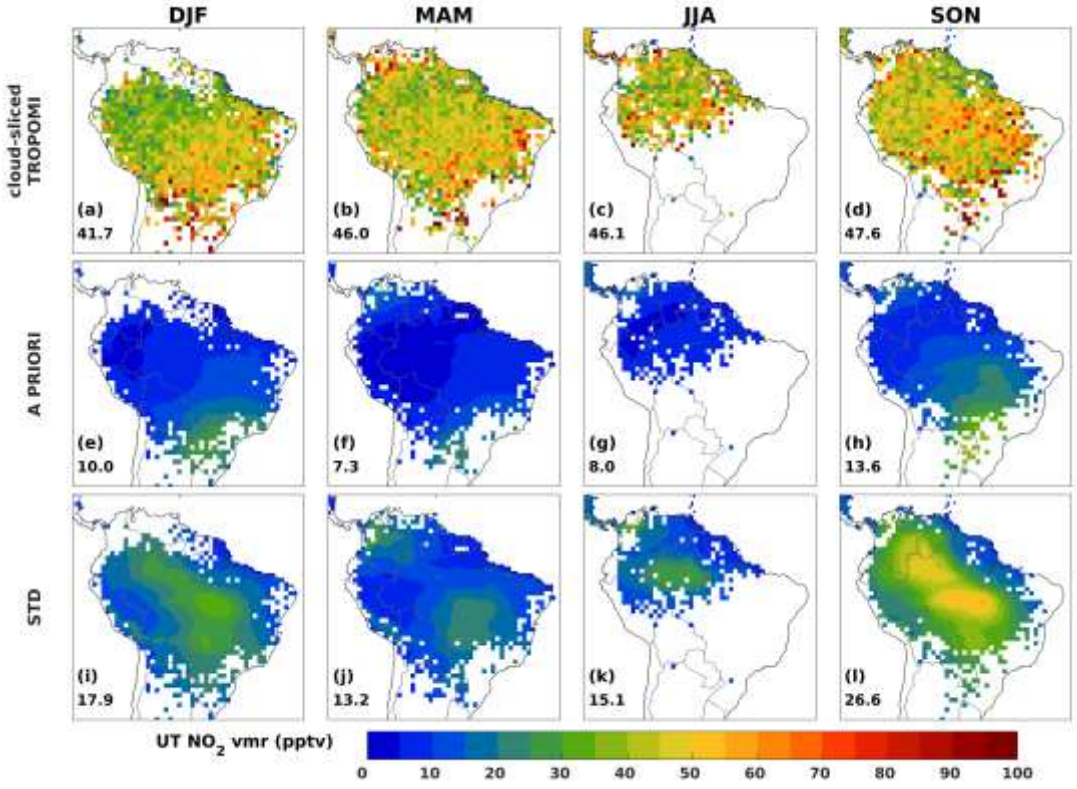

Figure 31: *Seasonal distribution of upper-troposphere NO_2 volume mixing ratios (in ppt) in December-January-February (DJF), March-April-May (MAM), June-July-August (JJA) and September-October-November (SON) for cloud-sliced TROPOMI NO_2 (Horner et al., 2024) (top-row), the a priori model (middle row) and after inversion (bottom row). Blanks are grid cells without cloud-sliced retrievals due to lack of optically thick clouds over regions of subsidence.*

In line with the a posteriori model, the seasonal maximum/minimum in the cloud-sliced concentrations occurs in SON/DJF. While the model succeeds at predicting the maximum in SON, the modelled minimum takes place later in the year, in MAM. The optimisation leads to spatial patterns that agree better with the observation and the distribution shown in Oda et al. (2022). During SON, the a posteriori agreement is better than a factor of 2. Also, the optimisation leads to a marked seasonal increase in SON (~26 ppt) compared to the model annual average (18 ppt). The disparities are largest in MAM and JJA: a factor of 6 in the a priori, and a factor of 3 after inversion. In DJF, the region of maximum concentration is observed in the southern part of the continent, in agreement with the a priori, but the inversion suggests a shift towards lower latitudes. This shift of maximal values towards the central part of South America is however in better agreement with the SON distribution. Overall, the higher lightning source derived by the inversion appears to be corroborated by the independent UT NO_2 observations, although an even larger source would be required to match the observations.

4.3.5. Recommendations

The evaluation of isoprene columns over Africa following the inversion of VOC emissions against CrIS isoprene observations points to an improved agreement when using a two-species inversion — VOC and NO_X based on HCHO and NO_2 satellite constraints— compared to the single-species relying solely on HCHO satellite data to derive VOC emissions. This highlights the importance of incorporating satellite NO_2 observations through joint NO_2-HCHO inversion framework, especially in tropical regions where the distribution and intensity of NO_X sources remain highly uncertain.

5. DISSEMINATION AND VALORISATION

5.1. PhD thesis

This project funded the PhD thesis of Opacka Beata, entitled "Emission Quantification of Atmospheric Tracers in the Tropics using Satellite Observations and Inversion Techniques." The thesis was supervised by Prof. Pierre-François Coheur (ULB) and Dr. Trissevgeni Stavrakou (BIRA-IASB) and was defended on 18 April 2025. The manuscript is publicly available at https://difusion.ulb.ac.be.

5.2. Websites

The results of the EQUATOR project and the corresponding data are available on the following websites:

- https://equator.aeronomie.be
- https://tropo.aeronomie.be
- https://emissions.aeronomie.be
- https://data.aeronomie.be

5.3. Meetings, workshops and conferences

2024: Presentations

"Simultaneous inversion of VOC and NOx emissions based on TROPOMI data in the Tropics reveals the importance of chemical feedbacks", T. Stavrakou, B. Opacka, J.-F. Müller, I. De Smedt *(invited)*, AGU Fall Meeting, Washington DC, 9-13 December 2024.

"Natural emissions in Africa: Improved quantification using a joint inversion of TROPOMI NO_2 and HCHO columns in the MAGRITTE CTM and evaluation", B. Opacka, T. Stavrakou, J.-F. Müller and A. Guenther, IGAC 2024, Kuala Lumpur, Malaysia, 9-13 September 2024.

"Improved determination of natural emissions in Africa from a joint inversion of TROPOMI NO_2 and HCHO columns in the MAGRITTE CTM", T. Stavrakou, B. Opacka, J.-F. Müller, T. Stavrakou, et al. ESA ATMOS conference, Bologna, 1-5 July 2024.

"Using satellite observations to quantify hydrocarbon emissions: advances and perspectives", T. Stavrakou, J.-F. Müller et al., *(invited)* ARGONAUT (Pollutants and greenhouse gas emission monitoring from space at high resolution) Workshop, Paris, 22-23 April 2024.

2023: Presentations

"Can we trust satellite observations to quantify VOC emissions and their spatio-temporal variability?", J.-F. Müller, T. Stavrakou et al. (invited) International Expert Workshop on Volatile Organic Compounds, Hong Kong, 27 November-4 December 2023.

"Lessons learnt and future prospects in air quality, emissions and chemical climate", T. Stavrakou, J.-F. Müller et al. (invited), 1st International Conference on Chemical Weather and Chemical Climate (CWCC), Shanghai, 16-20 October 2023.

"Assessing soil NOx emissions over Africa using TROPOMI NO2 observations and inverse modelling", B. Opacka, J.-F. Müller, G.-M. Oomen, T. Stavrakou, 20th GEIA Conference, Brussels, 21-23 June 2023.

"New remote sensing methods", T. Stavrakou, J.-F. Müller, G.-M. Oomen, B. Opacka, M. Van Damme (invited), Gordon Research Conference: Atmospheric Chemistry, Newry, Maine, 30 July-4 August 2023.

"Assessing air composition over Africa over the last two decades using satellite observations and modelling", T. Stavrakou, J.-F. Müller, B. Opacka, Workshop on a Pilot Design for aIr quality in Africa, Kigali, Rwanda, 17-19 January 2023.

2022: Presentations

"Continuous monitoring of biogenic VOC fluxes over South America by inversion of TROPOMI HCHO columns", T. Stavrakou, J.-F. Müller, B. Opacka, G.-M. Oomen and C. Vigouroux, Sentinel-5P Mission: 5 Years Anniversary, Taormina, 10-14 October 2022.

"Improved estimates of soil NO fluxes inferred by TROPOMI NO2 observations and inverse modelling ", B. Opacka, J.-F. Müller, T. Stavrakou and M. Van Damme, Sentinel-5P Mission: 5 Years Anniversary, Taormina, 10-14 October 2022.

"Tropical soil NO emissions: the view from TROPOMI NO_2 column data", B. Opacka, J.-F. Müller, and T. Stavrakou, iCACGP-IGAC Joint Conference, Manchester, 11-15 September 2022.

"Continuous monitoring of biogenic VOC fluxes over South America by inversion of TROPOMI HCHO columns", T. Stavrakou, J.-F. Müller, B. Opacka, G.-M. Oomen and C. Vigouroux, iCACGP-IGAC Joint Conference, Manchester, 11-15 September 2022.

"Towards an improved understanding of BVOC fluxes using spaceborne data", T. Stavrakou, J.-F. Müller, B. Opacka, G.-M. Oomen et al., *(invited)*, Gordon Science Conference: Biogenic Hydrocarbons and the Atmosphere, Oxnard, California, 12-17 June 2022.

"*Evaluation of soil NOx emissions in the Tropics using field data and TROPOMI NO_2 columns",* B. Opacka*,* J.-F. Müller, J. Stavrakou, EGU General Assembly, Vienna, 3-8 April 2022.

2021: Presentations

"Two-decadal (2001-2018) biogenic flux estimated over Africa based on MEGAN and satellite land cover data", B. Opacka, J.-F. Müller, T. Stavrakou, M. Bauwens, and A. Guenther, NCAR Workshop on Advancing Air Quality Science in Africa, 10-12 March 2021.

"Satellite measurements over Africa: the view from TROPOMI", M. Bauwens, T. Stavrakou, J.-F. Müller, NCAR Workshop on Advancing Air Quality Science in Africa, 10-12 March 2021.

2020: Presentations

"Effects of land cover changes on isoprene emissions evaluated using spaceborne formaldehyde data from the OMI sensor and multiyear model simulations", B. Opacka, T. Stavrakou, J.-F. Müller, A. Guenther, AGU Virtual Fall Meeting, 7-11 December 2020.

"Distribution and trends of biogenic emissions over South American ecocystems deduced by multiyear inversion of satellite formaldehyde data", T. Stavrakou, J.-F. Müller, M. Bauwens, I. De Smedt, M. Van Roozendael, 19th GEIA Virtual Science Conference, 23 June 2020.

"Evaluating the impact of different spaceborne land cover distributions on isoprene emissions and their trends using the MEGAN model", B. Opacka, J.-F. Müller, T. Stavrakou, M. Bauwens, A. Guenther, EGU Online General Assembly, 4-8 May 2020 & 19th GEIAVirtual Science Conference, 23 June 2020.

5.4. Datasets

(1) The ALBERI dataset (2001-2018) is available in NetCDF format for download from https://emissions.aeronomie.be and https://data.aeronomie.be.
- Opacka, B. & Müller, J.-F. (2021). *MEGAN-MOHYCAN global isoprene emissions accounting for space-based land cover changes* [ALBERI dataset], https://doi.org/10.18758/71021062

(2) Satellite-derived global isoprene emission estimates based on bias-corrected OMI HCHO (2005-2017) are available in NetCDF format for download from https://emissions.aeronomie.be/omi-based/isoprene-bc-omi-based.

(3) TD emission inventories of isoprene, soil NO_X, and lightning NO_X for the year 2019, derived using the two-species inversion method, are available in NetCDF format on our repository website https://emission.aeronomie.be.
- Stavrakou, T. (2025). *Top-down isoprene emissions over Africa based on TROPOMI HCHO data* (Version 1) [Data set]. Royal Belgian Institute for Space Aeronomy. https://doi.org/10.18758/OOB6AEEN
- Stavrakou, T. (2025). *Top-down soil NO emissions over Africa based on TROPOMI data* (Version 1) [Data set]. Royal Belgian Institute for Space Aeronomy. https://doi.org/10.18758/8AP1X3FW
- Stavrakou, T. (2025). *Top-down lightning NO emissions over Africa based on TROPOMI data* (Version 1) [Data set]. Royal Belgian Institute for Space Aeronomy. https://doi.org/10.18758/

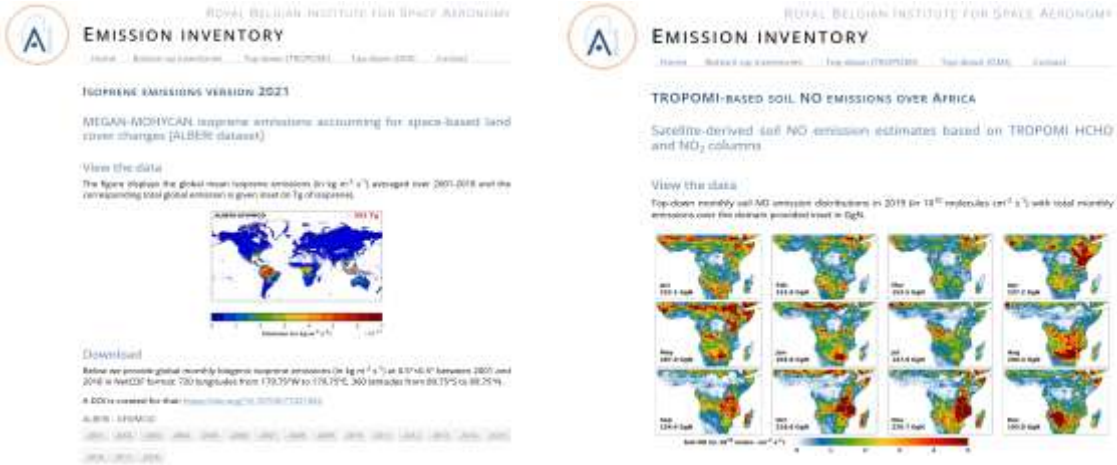

Figure 32: Emission inventories are available for download at https://emissions.aeronomie.be.

5.5. Outreach

We contributed to several outreach articles aimed at a broad, non-scientific audience:

- "Émissions de la végétation : pourquoi sont-elles importantes?", presented during the BIRA-IASB Open Days in September **2022**. Available on the BIRA-IASB website (https://www.aeronomie.be/fr/nouvelles/2022/posters-portes-ouvertes-edition-2022).

- "How do trees affect the Earth's atmosphere and climate?", published for International Forest Day on 21 March **2021** on the BIRA-IASB website (https://www.aeronomie.be/en/news/2021/how-do-trees-affect-earths-atmosphere-and-climate).

- "Les plantes n'émettent pas que de l'oxygène" by Laetitia Theunis, published on the Daily Science website in November **2022** (https://dailyscience.be/14/11/2022/les-plantes-nemettent-pas-que-de-loxygene/.).

6. PUBLICATIONS

Opacka, B., T. **Stavrakou**, J.-F. **Müller**, I. De Smedt, J. van Geffen, E. Marais, R. Horner, D. Millet, K. Wells, A. Guenther: Natural emissions of VOC and NOx over Africa constrained by TROPOMI HCHO and NO2 data using the MAGRITTEv1.1 model. *Atmos. Chem. Phys.*, 25, 2863-2894, https://doi.org/10.5194/acp-25-2863-2025, 2025.

Müller, J.-F., T. **Stavrakou**, G.-M. Oomen, B. **Opacka**, I. De Smedt, A. Guenther, C. Vigouroux, B. Langerock, C. A. Bauer Aquino, T. Blumenstock, M. Grutter, J. W. Hannigan, N. Jones, R. Kivi, E. Lutsch, E. Mahieu, M. Makarova, J.-M. Metzger, I. Morino, I. Murata, T. Nagahama, J. Notholt, I. Ortega, M. Palm, A. Röhling, D. Smale, W. Stremme, K. Strong, R. Sussmann, Y. Té, H. Winkler, A. Fried and T. Hanisco: Bias characterization of OMI HCHO columns based on FTIR columns and aircraft measurements and impact on top-down emission estimates. *Atmos. Chem. Phys.*, https://doi.org/10.5194/acp-24-2207-2024, 2024.

Opacka, B., J.F. **Müller**, T. **Stavrakou**, M. Bauwens, K. Sindelarova, J. Markova, A. Guenther: Global and regional impacts of land cover changes on isoprene emissions derived from spaceborne data and the MEGAN model, *Atmos. Chem. Phys.*, 21, 8413–8436, https://doi.org/10.5194/acp-21-8413-2021, 2021.

7. ACKNOWLEDGEMENTS

This research was carried out as part of the EQUATOR project funded by the Belgian Science Policy Office (BELSPO) through the BRAIN-be 2.0 programme (grant no. B2/202/P1/EQUATOR, 2021–2025). It was also supported by the European Space Agency's IMPALA project (grant no. 4000139771/22/I-DT-bgh, 2023–2025), TROVA-3 (2024–2026), PRODEX TROVA-E2 (2021–2023) and the PRODEX TROVA (2019–2020) projects. This research was also funded by the Belgian Science Policy Office (BELSPO) through the STEREO III programme (ALBERI project, contract no. SR/00/373 (2019–2021)).

We gratefully acknowledge the follow-up committee for their valuable insights and guidance throughout the course of the project. The committee is composed of:

- Prof. **Pierre-François Coheur** from the Spectroscopy, Quantum Chemistry and Atmospheric Remote Sensing, ULB
- Prof. **Katerina Sindelarova** from the Department of Atmospheric Physics, Charles University, Prague
- Prof. **Ronald van der A** from the R&D Satellite Observations, Royal Netherlands Meteorological Institute (KNMI)
- Dr. **Corinne Vigouroux** from the Infrared Observations and Lab Experiments, Royal Belgian Institute for Space Aeronomy.

REFERENCES

Abbot, D. S., Palmer, P. I., Martin, R. V., Chance, K. V., Jacob, D. J., and Guenther, A.: Seasonal and interannual variability of North American isoprene emissions as determined by formaldehyde column measurements from space, Geophysical Research Letters, 30, https://doi.org/10.1029/2003GL017336, 2003.

Adon, M., Galy-Lacaux, C., Yoboué, V., Delon, C., Lacaux, J. P., Castera, P., Gardrat, E., Pienaar, J., Al Ourabi, H., Laouali, D., Diop, B., Sigha-Nkamdjou, L., Akpo, A., Tathy, J. P., Lavenu, F., and Mougin, E.: Long term measurements of sulfur dioxide, nitrogen dioxide, ammonia, nitric acid and ozone in Africa using passive samplers, Atmospheric Chemistry and Physics, 10, 7467–7487, https://doi.org/10.5194/acp-10-7467-2010, 2010.

Andreae, M. O.: Emission of trace gases and aerosols from biomass burning – an updated assessment, Atmospheric Chemistry and Physics, 19, 8523–8546, https://doi.org/10.5194/acp-19-8523-2019, 2019.

Arneth, A., Schurgers, G., Lathiere, J., Duhl, T., Beerling, D. J., Hewitt, C. N., Martin, M., and Guenther, A.: Global terrestrial isoprene emission models: sensitivity to variability in climate and vegetation, Atmospheric Chemistry and Physics, 11, 8037–8052, https://doi.org/10.5194/acp-11-8037-2011, 2011.

Atkinson, R.: Atmospheric chemistry of VOCs and NOx, Atmospheric Environment, 34, 2063–2101, https://doi.org/10.1016/S1352-2310(99)00460-4, 2000.

Bakwin, P. S., Wofsy, S. C., Fan, S.-M., Keller, M., Trumbore, S. E., and Da Costa, J. M.: Emission of nitric oxide (NO) from tropical forest soils and exchange of NO between the forest canopy and atmospheric boundary layers, J. Geophys. Res., 95, 16755, https://doi.org/10.1029/JD095iD10p16755, 1990.

Barkley, M. P., Smedt, I. D., Van Roozendael, M., Kurosu, T. P., Chance, K., Arneth, A., Hagberg, D., Guenther, A., Paulot, F., Marais, E., and Mao, J.: Top-down isoprene emissions over tropical South

America inferred from SCIAMACHY and OMI formaldehyde columns, Journal of Geophysical Research: Atmospheres, 118, 6849–6868, https://doi.org/10.1002/jgrd.50552, 2013.

Bauwens, M., Stavrakou, T., Müller, J.-F., De Smedt, I., Van Roozendael, M., van der Werf, G. R., Wiedinmyer, C., Kaiser, J. W., Sindelarova, K., and Guenther, A.: Nine years of global hydrocarbon emissions based on source inversion of OMI formaldehyde observations, Atmospheric Chemistry and Physics, 16, 10133–10158, https://doi.org/10.5194/acp-16-10133-2016, 2016.

Boeke, N. L., Marshall, J. D., Alvarez, S., Chance, K. V., Fried, A., Kurosu, T. P., Rappenglück, B., Richter, D., Walega, J., Weibring, P., and Millet, D. B.: Formaldehyde columns from the Ozone Monitoring Instrument: Urban versus background levels and evaluation using aircraft data and a global model, J. Geophys. Res., 116, D05303, https://doi.org/10.1029/2010JD014870, 2011.

Carmo, J. B. do, Piccolo, M. de C., Andrade, C. A. de, Cerri, C. E. P., Feigl, B. J., Neto, E. S., and Cerri, C. C.: Short-term changes in nitrogen availability, gas fluxes (CO2, NO, N2O) and microbial biomass after tillage during pasture re-establishment in Rondônia, Brazil, Soil and Tillage Research, 96, 250–259, https://doi.org/10.1016/j.still.2007.06.002, 2007.

Cattânio, J., Davidson, E., Nepstad, D., Verchot, L., and Ackerman, I.: Unexpected results of a pilot throughfall exclusion experiment on soil emissions of CO 2 , CH 4 , N 2 O, and NO in eastern Amazonia, Biology and Fertility of Soils, 36, 102–108, https://doi.org/10.1007/s00374-002-0517-x, 2002.

Cazorla, M., Wolfe, G. M., Bailey, S. A., Swanson, A. K., Arkinson, H. L., and Hanisco, T. F.: A new airborne laser-induced fluorescence instrument for in situ detection of formaldehyde throughout the troposphere and lower stratosphere, Atmospheric Measurement Techniques, 8, 541–552, https://doi.org/10.5194/amt-8-541-2015, 2015.

Cecil, D. J., Buechler, D. E., and Blakeslee, R. J.: Gridded lightning climatology from TRMM-LIS and OTD: Dataset description, Atmospheric Research, 135–136, 404–414, https://doi.org/10.1016/j.atmosres.2012.06.028, 2014.

Claeys, M., Graham, B., Vas, G., Wang, W., Vermeylen, R., Pashynska, V., Cafmeyer, J., Guyon, P., Andreae, M., Artaxo, P., and Maenhaut, W.: Formation of Secondary Organic Aerosols Through Photooxidation of Isoprene, Science (New York, N.Y.), 303, 1173–6, https://doi.org/10.1126/science.1092805, 2004.

Compernolle, S.: Quarterly Validation Report of the Sentinel-5 Precursor Operational Data Products #23: April 2018 - May 2024, 2024.

Congalton, R. G., Gu, J., Yadav, K., Thenkabail, P., and Ozdogan, M.: Global Land Cover Mapping: A Review and Uncertainty Analysis, Remote Sensing, 6, 12070–12093, https://doi.org/10.3390/rs61212070, 2014.

Curtis, P. G., Slay, C. M., Harris, N. L., Tyukavina, A., and Hansen, M. C.: Classifying drivers of global forest loss, Science, 361, 1108–1111, https://doi.org/10.1126/science.aau3445, 2018.

Darmenov, A. S. and Da Silva, A.: The Quick Fire Emissions Dataset (QFED): Documentation of versions 2.1, 2.2 and 2.4., 2015.

Davidson, E. A., Nepstad, D. C., Ishida, F. Y., and Brando, P. M.: Effects of an experimental drought and recovery on soil emissions of carbon dioxide, methane, nitrous oxide, and nitric oxide in a moist tropical forest, Global Change Biology, 14, 2582–2590, https://doi.org/10.1111/j.1365-2486.2008.01694.x, 2008.

De Smedt, I., Stavrakou, T., Hendrick, F., Danckaert, T., Vlemmix, T., Pinardi, G., Theys, N., Lerot, C., Gielen, C., Vigouroux, C., Hermans, C., Fayt, C., Veefkind, P., Müller, J.-F., and Van Roozendael, M.: Diurnal, seasonal and long-term variations of global formaldehyde columns inferred from combined OMI and GOME-2 observations, Atmospheric Chemistry and Physics, 15, 12519–12545, https://doi.org/10.5194/acp-15-12519-2015, 2015.

De Smedt, I., Theys, N., Yu, H., Danckaert, T., Lerot, C., Compernolle, S., Van Roozendael, M., Richter, A., Hilboll, A., Peters, E., Pedergnana, M., Loyola, D., Beirle, S., Wagner, T., Eskes, H., van Geffen, J., Boersma, K. F., and Veefkind, P.: Algorithm theoretical baseline for formaldehyde retrievals from S5P TROPOMI and from the QA4ECV project, Atmospheric Measurement Techniques, 11, 2395–2426, https://doi.org/10.5194/amt-11-2395-2018, 2018.

De Smedt, I., Pinardi, G., Vigouroux, C., Compernolle, S., Bais, A., Benavent, N., Boersma, F., Chan, K.-L., Donner, S., Eichmann, K.-U., Hedelt, P., Hendrick, F., Irie, H., Kumar, V., Lambert, J.-C., Langerock, B., Lerot, C., Liu, C., Loyola, D., Piters, A., Richter, A., Rivera Cárdenas, C., Romahn, F., Ryan, R. G., Sinha, V., Theys, N., Vlietinck, J., Wagner, T., Wang, T., Yu, H., and Van Roozendael, M.: Comparative assessment of TROPOMI and OMI formaldehyde observations and validation against MAX-DOAS network column measurements, Atmos. Chem. Phys., 21, 12561–12593, https://doi.org/10.5194/acp-21-12561-2021, 2021.

Delon, C., Mougin, E., Serça, D., Grippa, M., Hiernaux, P., Diawara, M., Galy-Lacaux, C., and Kergoat, L.: Modelling the effect of soil moisture and organic matter degradation on biogenic NO emissions from soils in Sahel rangeland (Mali), Biogeosciences, 12, 3253–3272, https://doi.org/10.5194/bg-12-3253-2015, 2015.

Delon, C., Galy-Lacaux, C., Serça, D., Loubet, B., Camara, N., Gardrat, E., Saneh, I., Fensholt, R., Tagesson, T., Le Dantec, V., Sambou, B., Diop, C., and Mougin, E.: Soil and vegetation-atmosphere exchange of NO, NH3, and N2O from field measurements in a semi arid grazed ecosystem in Senegal, Atmospheric Environment, 156, 36–51, https://doi.org/10.1016/j.atmosenv.2017.02.024, 2017.

Delon, C., Galy-Lacaux, C., Serça, D., Personne, E., Mougin, E., Adon, M., Le Dantec, V., Loubet, B., Fensholt, R., and Tagesson, T.: Modelling land–atmosphere daily exchanges of NO, NH₃, and CO₂ in a semi-arid grazed ecosystem in Senegal, Biogeosciences, 16, 2049–2077, https://doi.org/10.5194/bg-16-2049-2019, 2019.

ESA-CCI-LC: nd Cover CCI Product User Guide Version 2.0, 2017.

Eskes, H. J. and Eichmann, K.-U.: S5P Mission Performance Centre Nitrogen Dioxide [L2__NO2___] Readme, 2023.

Eskes, H. J., van Geffen, J., Sneep, M., Veefkind, P., Niemeijer, S., and Zehner, C.: S5P Nitrogen Dioxide v02.03.01 intermediate reprocessing on the S5P-PAL system: Readme file, 2021.

Fried, A., Walega, J. G., Olson, J. R., Crawford, J. H., Chen, G., Weibring, P., Richter, D., Roller, C., Tittel, F. K., Heikes, B. G., Snow, J. A., Shen, H., O'Sullivan, D. W., Porter, M., Fuelberg, H., Halland, J., and Millet, D. B.: Formaldehyde over North America and the North Atlantic during the summer 2004 INTEX campaign: Methods, observed distributions, and measurement-model comparisons, Journal of Geophysical Research: Atmospheres, 113, https://doi.org/10.1029/2007JD009185, 2008.

Fried, A., Cantrell, C., Olson, J., Crawford, J. H., Weibring, P., Walega, J., Richter, D., Junkermann, W., Volkamer, R., Sinreich, R., Heikes, B. G., O'Sullivan, D., Blake, D. R., Blake, N., Meinardi, S., Apel, E., Weinheimer, A., Knapp, D., Perring, A., Cohen, R. C., Fuelberg, H., Shetter, R. E., Hall, S. R., Ullmann, K., Brune, W. H., Mao, J., Ren, X., Huey, L. G., Singh, H. B., Hair, J. W., Riemer, D., Diskin, G., and Sachse,

G.: Detailed comparisons of airborne formaldehyde measurements with box models during the 2006 INTEX-B and MILAGRO campaigns: potential evidence for significant impacts of unmeasured and multi-generation volatile organic carbon compounds, Atmospheric Chemistry and Physics, 11, 11867–11894, https://doi.org/10.5194/acp-11-11867-2011, 2011.

Fried, A., Walega, J., Weibring, P., Richter, D., Simpson, I. J., Blake, D. R., Blake, N. J., Meinardi, S., Barletta, B., Hughes, S. C., Crawford, J. H., Diskin, G., Barrick, J., Hair, J., Fenn, M., Wisthaler, A., Mikoviny, T., Woo, J. H., Park, M., Kim, J., Min, K. E., Jeong, S., Wennberg, P. O., Kim, M. J., Crounse, J. D., Teng, A. P., Bennett, R., Yang-Martin, M., Shook, M. A., Huey, G., Tanner, D., Knote, C., Kim, J. H., Park, R., and Brune, W.: Airborne formaldehyde and volatile organic compound measurements over the Daesan petrochemical complex on Korea's northwest coast during the Korea-United States Air Quality study: Estimation of emission fluxes and effects on air quality, Elementa, 8, https://doi.org/10.1525/lementa.2020.121, 2020.

Fu, D., Millet, D. B., Wells, K. C., Payne, V. H., Yu, S., Guenther, A., and Eldering, A.: Direct retrieval of isoprene from satellite-based infrared measurements, Nat Commun, 10, 3811, https://doi.org/10.1038/s41467-019-11835-0, 2019.

Fu, T.-M., Jacob, D. J., Palmer, P. I., Chance, K., Wang, Y. X., Barletta, B., Blake, D. R., Stanton, J. C., and Pilling, M. J.: Space-based formaldehyde measurements as constraints on volatile organic compound emissions in east and south Asia and implications for ozone, Journal of Geophysical Research: Atmospheres, 112, https://doi.org/10.1029/2006JD007853, 2007.

Ganzeveld, L. N., Lelieveld, J., Dentener, F. J., Krol, M. C., Bouwman, A. J., and Roelofs, G.-J.: Global soil-biogenic NOx emissions and the role of canopy processes, Journal of Geophysical Research: Atmospheres, 107, ACH 9-1-ACH 9-17, https://doi.org/10.1029/2001JD001289, 2002.

Garcia-Montiel, D. C., Steudler, P. A., Piccolo, M. C., Melillo, J. M., Neill, C., and Cerri, C. C.: Controls on soil nitrogen oxide emissions from forest and pastures in the Brazilian Amazon, Global Biogeochemical Cycles, 15, 1021–1030, https://doi.org/10.1029/2000GB001349, 2001.

van Geffen, J., Eskes, H., Compernolle, S., Pinardi, G., Verhoelst, T., Lambert, J.-C., Sneep, M., ter Linden, M., Ludewig, A., Boersma, K. F., and Veefkind, J. P.: Sentinel-5P TROPOMI NO_2 retrieval: impact of version v2.2 improvements and comparisons with OMI and ground-based data, Atmospheric Measurement Techniques, 15, 2037–2060, https://doi.org/10.5194/amt-15-2037-2022, 2022.

Granier, C., Darras, S., Denier van der Gon, H., Doubalova, J., Elguindi, N., Galle, B., Gauss, M., Guevara, M., Jalkanen, J.-P., Kuenen, J., Liousse, C., Quack, B., Simpson, D., and Sindelarova, K.: The Copernicus Atmosphere Monitoring Service global and regional emissions (April 2019 version), Copernicus Atmosphere Monitoring Service, https://doi.org/10.24380/D0BN-KX16, 2019.

Guenther, A. B., Jiang, X., Heald, C. L., Sakulyanontvittaya, T., Duhl, T., Emmons, L. K., and Wang, X.: The Model of Emissions of Gases and Aerosols from Nature version 2.1 (MEGAN2.1): an extended and updated framework for modeling biogenic emissions, Geoscientific Model Development, 5, 1471–1492, https://doi.org/10.5194/gmd-5-1471-2012, 2012a.

Guenther, A. B., Jiang, X., Heald, C. L., Sakulyanontvittaya, T., Duhl, T., Emmons, L. K., and Wang, X.: The Model of Emissions of Gases and Aerosols from Nature version 2.1 (MEGAN2.1): an extended and updated framework for modeling biogenic emissions, Geoscientific Model Development, 5, 1471–1492, https://doi.org/10.5194/gmd-5-1471-2012, 2012b.

Hansen, M. C., Potapov, P. V., Moore, R., Hancher, M., Turubanova, S. A., Tyukavina, A., Thau, D., Stehman, S. V., Goetz, S. J., Loveland, T. R., Kommareddy, A., Egorov, A., Chini, L., Justice, C. O., and

Townshend, J. R. G.: High-Resolution Global Maps of 21st-Century Forest Cover Change, Science, 342, 850–853, https://doi.org/10.1126/science.1244693, 2013.

Hersbach, H., Bell, B., Berrisford, P., Hirahara, S., Horányi, A., Muñoz-Sabater, J., Nicolas, J., Peubey, C., Radu, R., Schepers, D., Simmons, A., Soci, C., Abdalla, S., Abellan, X., Balsamo, G., Bechtold, P., Biavati, G., Bidlot, J., Bonavita, M., De Chiara, G., Dahlgren, P., Dee, D., Diamantakis, M., Dragani, R., Flemming, J., Forbes, R., Fuentes, M., Geer, A., Haimberger, L., Healy, S., Hogan, R. J., Hólm, E., Janisková, M., Keeley, S., Laloyaux, P., Lopez, P., Lupu, C., Radnoti, G., de Rosnay, P., Rozum, I., Vamborg, F., Villaume, S., and Thépaut, J.-N.: The ERA5 global reanalysis, Quarterly Journal of the Royal Meteorological Society, 146, 1999–2049, https://doi.org/10.1002/qj.3803, 2020.

Horner, R. P., Marais, E. A., Wei, N., Ryan, R. G., and Shah, V.: Vertical profiles of global tropospheric nitrogen dioxide (NO_2) obtained by cloud-slicing TROPOMI, EGUsphere [preprint], 1–29, https://doi.org/10.5194/egusphere-2024-1541, 2024.

Huang, G., Brook, R., Crippa, M., Janssens-Maenhout, G., Schieberle, C., Dore, C., Guizzardi, D., Muntean, M., Schaaf, E., and Friedrich, R.: Speciation of anthropogenic emissions of non-methane volatile organic compounds: a global gridded data set for 1970–2012, Atmospheric Chemistry and Physics, 17, 7683–7701, https://doi.org/10.5194/acp-17-7683-2017, 2017.

Hubau, W., Lewis, S. L., Phillips, O. L., Affum-Baffoe, K., Beeckman, H., Cuní-Sanchez, A., Daniels, A. K., Ewango, C. E. N., Fauset, S., Mukinzi, J. M., Sheil, D., Sonké, B., Sullivan, M. J. P., Sunderland, T. C. H., Taedoumg, H., Thomas, S. C., White, L. J. T., Abernethy, K. A., Adu-Bredu, S., Amani, C. A., Baker, T. R., Banin, L. F., Baya, F., Begne, S. K., Bennett, A. C., Benedet, F., Bitariho, R., Bocko, Y. E., Boeckx, P., Boundja, P., Brienen, R. J. W., Brncic, T., Chezeaux, E., Chuyong, G. B., Clark, C. J., Collins, M., Comiskey, J. A., Coomes, D. A., Dargie, G. C., de Haulleville, T., Kamdem, M. N. D., Doucet, J.-L., Esquivel-Muelbert, A., Feldpausch, T. R., Fofanah, A., Foli, E. G., Gilpin, M., Gloor, E., Gonmadje, C., Gourlet-Fleury, S., Hall, J. S., Hamilton, A. C., Harris, D. J., Hart, T. B., Hockemba, M. B. N., Hladik, A., Ifo, S. A., Jeffery, K. J., Jucker, T., Yakusu, E. K., Kearsley, E., Kenfack, D., Koch, A., Leal, M. E., Levesley, A., Lindsell, J. A., Lisingo, J., Lopez-Gonzalez, G., Lovett, J. C., Makana, J.-R., Malhi, Y., Marshall, A. R., Martin, J., Martin, E. H., Mbayu, F. M., Medjibe, V. P., Mihindou, V., Mitchard, E. T. A., Moore, S., Munishi, P. K. T., Bengone, N. N., Ojo, L., Ondo, F. E., Peh, K. S.-H., Pickavance, G. C., Poulsen, A. D., Poulsen, J. R., Qie, L., Reitsma, J., Rovero, F., Swaine, M. D., Talbot, J., Taplin, J., Taylor, D. M., Thomas, D. W., Toirambe, B., Mukendi, J. T., Tuagben, D., Umunay, P. M., et al.: Asynchronous carbon sink saturation in African and Amazonian tropical forests, Nature, 579, 80–87, https://doi.org/10.1038/s41586-020-2035-0, 2020.

Hudman, R. C., Moore, N. E., Mebust, A. K., Martin, R. V., Russell, A. R., Valin, L. C., and Cohen, R. C.: Steps towards a mechanistic model of global soil nitric oxide emissions: implementation and space based-constraints, Atmospheric Chemistry and Physics, 12, 7779–7795, https://doi.org/10.5194/acp-12-7779-2012, 2012.

Jacob, D. J. and Wofsy, S. C.: Budgets of reactive nitrogen, hydrocarbons, and ozone over the Amazon forest during the wet season, Journal of Geophysical Research: Atmospheres, 95, 16737–16754, https://doi.org/10.1029/JD095iD10p16737, 1990.

Jaeglé, L., Steinberger, L., Martin, R. V., and Chance, K.: Global partitioning of NOx sources using satellite observations: Relative roles of fossil fuel combustion, biomass burning and soil emissions, Faraday Discuss., 130, 407–423, https://doi.org/10.1039/B502128F, 2005.

Janssens-Maenhout, G., Crippa, M., Guizzardi, D., Dentener, F., Muntean, M., Pouliot, G., Keating, T., Zhang, Q., Kurokawa, J., Wankmüller, R., Denier van der Gon, H., Kuenen, J. J. P., Klimont, Z., Frost, G.,

Darras, S., Koffi, B., and Li, M.: HTAP_v2.2: a mosaic of regional and global emission grid maps for 2008 and 2010 to study hemispheric transport of air pollution, Atmospheric Chemistry and Physics, 15, 11411–11432, https://doi.org/10.5194/acp-15-11411-2015, 2015.

Johansson, C. and Sanhueza, E.: Emission of NO from savanna soils during rainy season, Journal of Geophysical Research: Atmospheres, 93, 14193–14198, https://doi.org/10.1029/JD093iD11p14193, 1988.

Johansson, C., Rodhe, H., and Sanhueza, E.: Emission of NO in a tropical savanna and a cloud forest during the dry season, Journal of Geophysical Research: Atmospheres, 93, 7180–7192, https://doi.org/10.1029/JD093iD06p07180, 1988.

Kaiser, J., Jacob, D. J., Zhu, L., Travis, K. R., Fisher, J. A., González Abad, G., Zhang, L., Zhang, X., Fried, A., Crounse, J. D., St. Clair, J. M., and Wisthaler, A.: High-resolution inversion of OMI formaldehyde columns to quantify isoprene emission on ecosystem-relevant scales: application to the southeast US, Atmospheric Chemistry and Physics, 18, 5483–5497, https://doi.org/10.5194/acp-18-5483-2018, 2018.

Kaplan, W. A., Wofsy, S. C., Keller, M., and Costa, J. M. D.: Emission of NO and deposition of O3 in a tropical forest system, Journal of Geophysical Research: Atmospheres, 93, 1389–1395, https://doi.org/10.1029/JD093iD02p01389, 1988.

Keller, M. and Reiners, W. A.: Soil-atmosphere exchange of nitrous oxide, nitric oxide, and methane under secondary succession of pasture to forest in the Atlantic lowlands of Costa Rica, Global Biogeochemical Cycles, 8, 399–409, https://doi.org/10.1029/94GB01660, 1994.

Keller, M., Varner, R., Dias, J. D., Silva, H., Crill, P., Oliveira, R. C. de, and Asner, G. P.: Soil–Atmosphere Exchange of Nitrous Oxide, Nitric Oxide, Methane, and Carbon Dioxide in Logged and Undisturbed Forest in the Tapajos National Forest, Brazil, Earth Interactions, 9, 1–28, https://doi.org/10.1175/EI125.1, 2005.

Koehler, B., Corre, M. D., Veldkamp, E., Wullaert, H., and Wright, S. J.: Immediate and long-term nitrogen oxide emissions from tropical forest soils exposed to elevated nitrogen input, Global Change Biology, 15, 2049–2066, https://doi.org/10.1111/j.1365-2486.2008.01826.x, 2009.

Kwon, H.-A., Park, R. J., Oak, Y. J., Nowlan, C. R., Janz, S. J., Kowalewski, M. G., Fried, A., Walega, J., Bates, K. H., Choi, J., Blake, D. R., Wisthaler, A., and Woo, J.-H.: Top-down estimates of anthropogenic VOC emissions in South Korea using formaldehyde vertical column densities from aircraft during the KORUS-AQ campaign, Elementa: Science of the Anthropocene, 9, 00109, https://doi.org/10.1525/elementa.2021.00109, 2021.

Lamarque, J.-F., Brasseur, G. P., Hess, P. G., and Müller, J.-F.: Three-dimensional study of the relative contributions of the different nitrogen sources in the troposphere, Journal of Geophysical Research: Atmospheres, 101, 22955–22968, https://doi.org/10.1029/96JD02160, 1996.

Lathière, J., Hauglustaine, D. A., Friend, A. D., De Noblet-Ducoudré, N., Viovy, N., and Folberth, G. A.: Impact of climate variability and land use changes on global biogenic volatile organic compound emissions, Atmospheric Chemistry and Physics, 6, 2129–2146, https://doi.org/10.5194/acp-6-2129-2006, 2006.

Le Roux, X., Abbadie, L., Lensi, R., and Serça, D.: Emission of nitrogen monoxide from African tropical ecosystems: Control of emission by soil characteristics in humid and dry savannas of West Africa, J. Geophys. Res., 100, 23133, https://doi.org/10.1029/95JD01923, 1995.

Lee, B. H., Munger, J. W., Wofsy, S. C., Rizzo, L. V., Yoon, J. Y. S., Turner, A. J., Thornton, J. A., and Swann, A. L. S.: Sensitive Response of Atmospheric Oxidative Capacity to the Uncertainty in the Emissions of Nitric Oxide (NO) From Soils in Amazonia, Geophysical Research Letters, 51, e2023GL107214, https://doi.org/10.1029/2023GL107214, 2024.

Levine, J. S., Winstead, E. L., Parsons, D. A. B., Scholes, M. C., Scholes, R. J., Cofer, W. R., Cahoon, D. R., and Sebacher, D. I.: Biogenic soil emissions of nitric oxide (NO) and nitrous oxide (N2O) from savannas in South Africa: The impact of wetting and burning, Journal of Geophysical Research: Atmospheres, 101, 23689–23697, https://doi.org/10.1029/96JD01661, 1996.

Liu, Y., Brito, J., Dorris, M. R., Rivera-Rios, J. C., Seco, R., Bates, K. H., Artaxo, P., Duvoisin, S., Keutsch, F. N., Kim, S., Goldstein, A. H., Guenther, A. B., Manzi, A. O., Souza, R. A. F., Springston, S. R., Watson, T. B., McKinney, K. A., and Martin, S. T.: Isoprene photochemistry over the Amazon rainforest, Proceedings of the National Academy of Sciences, 113, 6125–6130, https://doi.org/10.1073/pnas.1524136113, 2016.

Luhar, A. K., Galbally, I. E., Woodhouse, M. T., and Abraham, N. L.: Assessing and improving cloud-height-based parameterisations of global lightning flash rate, and their impact on lightning-produced NO_x and tropospheric composition in a chemistry–climate model, Atmospheric Chemistry and Physics, 21, 7053–7082, https://doi.org/10.5194/acp-21-7053-2021, 2021.

Marais, E. A., Jacob, D. J., Kurosu, T. P., Chance, K., Murphy, J. G., Reeves, C., Mills, G., Casadio, S., Millet, D. B., Barkley, M. P., Paulot, F., and Mao, J.: Isoprene emissions in Africa inferred from OMI observations of formaldehyde columns, Atmospheric Chemistry and Physics, 12, 6219–6235, https://doi.org/10.5194/acp-12-6219-2012, 2012.

Marais, E. A., Jacob, D. J., Guenther, A., Chance, K., Kurosu, T. P., Murphy, J. G., Reeves, C. E., and Pye, H. O. T.: Improved model of isoprene emissions in Africa using Ozone Monitoring Instrument (OMI) satellite observations of formaldehyde: implications for oxidants and particulate matter, Atmospheric Chemistry and Physics, 14, 7693–7703, https://doi.org/10.5194/acp-14-7693-2014, 2014.

Martin, R. V., Jacob, D. J., Chance, K., Kurosu, T. P., Palmer, P. I., and Evans, M. J.: Global inventory of nitrogen oxide emissions constrained by space-based observations of NO2 columns, Journal of Geophysical Research: Atmospheres, 108, https://doi.org/10.1029/2003JD003453, 2003.

Martin, R. V., Sauvage, B., Folkins, I., Sioris, C. E., Boone, C., Bernath, P., and Ziemke, J.: Space-based constraints on the production of nitric oxide by lightning, Journal of Geophysical Research: Atmospheres, 112, https://doi.org/10.1029/2006JD007831, 2007.

Matandirotya, Newton. R. and Burger, Roelof. P.: Spatiotemporal variability of tropospheric NO2 over four megacities in Southern Africa: Implications for transboundary regional air pollution, Environmental Challenges, 5, 100271, https://doi.org/10.1016/j.envc.2021.100271, 2021.

Meixner, F. X., Fickinger, Th., Marufu, L., Serça, D., Nathaus, F. J., Makina, E., Mukurumbira, L., and Andreae, M. O.: Preliminary results on nitric oxide emission from a southern African savanna ecosystem, Nutrient Cycling in Agroecosystems, 48, 123–138, https://doi.org/10.1023/A:1009765510538, 1997.

Messina, P., Lathière, J., Sindelarova, K., Vuichard, N., Granier, C., Ghattas, J., Cozic, A., and Hauglustaine, D. A.: Global biogenic volatile organic compound emissions in the ORCHIDEE and MEGAN models and sensitivity to key parameters, Atmospheric Chemistry and Physics, 16, 14169–14202, https://doi.org/10.5194/acp-16-14169-2016, 2016.

Millet, D. B., Jacob, D. J., Boersma, K. F., Fu, T.-M., Kurosu, T. P., Chance, K., Heald, C. L., and Guenther, A.: Spatial distribution of isoprene emissions from North America derived from formaldehyde column measurements by the OMI satellite sensor, Journal of Geophysical Research: Atmospheres, 113, https://doi.org/10.1029/2007JD008950, 2008.

Millet, D. B., Guenther, A., Siegel, D. A., Nelson, N. B., Singh, H. B., de Gouw, J. A., Warneke, C., Williams, J., Eerdekens, G., Sinha, V., Karl, T., Flocke, F., Apel, E., Riemer, D. D., Palmer, P. I., and Barkley, M.: Global atmospheric budget of acetaldehyde: 3-D model analysis and constraints from in-situ and satellite observations, Atmospheric Chemistry and Physics, 10, 3405–3425, https://doi.org/10.5194/acp-10-3405-2010, 2010.

Miyazaki, K., Eskes, H. J., and Sudo, K.: Global NO_x emission estimates derived from an assimilation of OMI tropospheric NO_2 columns, Atmospheric Chemistry and Physics, 12, 2263–2288, https://doi.org/10.5194/acp-12-2263-2012, 2012.

Müller, J.-F. and Brasseur, G.: IMAGES: A three-dimensional chemical transport model of the global troposphere, Journal of Geophysical Research: Atmospheres, 100, 16445–16490, https://doi.org/10.1029/94JD03254, 1995.

Müller, J.-F. and Stavrakou, T.: Inversion of CO and NO_x emissions using the adjoint of the IMAGES model, Atmospheric Chemistry and Physics, 5, 1157–1186, https://doi.org/10.5194/acp-5-1157-2005, 2005.

Müller, J.-F., Stavrakou, T., Wallens, S., De Smedt, I., Van Roozendael, M., Potosnak, M. J., Rinne, J., Munger, B., Goldstein, A., and Guenther, A. B.: Global isoprene emissions estimated using MEGAN, ECMWF analyses and a detailed canopy environment model, Atmospheric Chemistry and Physics, 8, 1329–1341, https://doi.org/10.5194/acp-8-1329-2008, 2008.

Müller, J.-F., Stavrakou, T., and Peeters, J.: Chemistry and deposition in the Model of Atmospheric composition at Global and Regional scales using Inversion Techniques for Trace gas Emissions (MAGRITTE v1.1) – Part 1: Chemical mechanism, Geoscientific Model Development, 12, 2307–2356, https://doi.org/10.5194/gmd-12-2307-2019, 2019.

Müller, J.-F., Stavrakou, T., Oomen, G.-M., Opacka, B., De, I., Guenther, A., Vigouroux, C., Langerock, B., Aquino, C. A. B., Grutter, M., Hannigan, J., Hase, F., Kivi, R., Lutsch, E., Mahieu, E., Makarova, M., Metzger, J.-M., Morino, I., Murata, I., Nagahama, T., Notholt, J., Ortega, I., Palm, M., Röhling, A., Stremme, W., Strong, K., Sussmann, R., Té, Y., and Fried, A.: Bias correction of OMI HCHO columns based on FTIR and aircraft measurements and impact on top-down emission estimates, Atmos. Chem. Phys., 2024.

Murray, L. T.: Lightning NOxand Impacts on Air Quality, Curr Pollution Rep, 2, 115–133, https://doi.org/10.1007/s40726-016-0031-7, 2016.

Naik, V., Delire, C., and Wuebbles, D. J.: Sensitivity of global biogenic isoprenoid emissions to climate variability and atmospheric CO2, Journal of Geophysical Research: Atmospheres, 109, https://doi.org/10.1029/2003JD004236, 2004.

Oda, P. S. S., Enoré, D. P., Mattos, E. V., Gonçalves, W. A., and Albrecht, R. I.: An initial assessment of the distribution of total Flash Rate Density (FRD) in Brazil from GOES-16 Geostationary Lightning Mapper (GLM) observations, Atmospheric Research, 270, 106081, https://doi.org/10.1016/j.atmosres.2022.106081, 2022.

Oomen, G.-M., Müller, J.-F., Stavrakou, T., De Smedt, I., Blumenstock, T., Kivi, R., Makarova, M., Palm, M., Röhling, A., Té, Y., Vigouroux, C., Friedrich, M. M., Frieß, U., Hendrick, F., Merlaud, A., Piters, A., Richter, A., Van Roozendael, M., and Wagner, T.: Weekly derived top-down volatile-organic-compound fluxes over Europe from TROPOMI HCHO data from 2018 to 2021, Atmospheric Chemistry and Physics, 24, 449–474, https://doi.org/10.5194/acp-24-449-2024, 2024.

Opacka, B. and Müller, J.-F.: MEGAN-MOHYCAN global isoprene emissions accounting for space-based land cover changes [ALBERI dataset], https://doi.org/10.18758/71021062, 2021, 2021.

Opacka, B., Müller, J.-F., Stavrakou, T., Bauwens, M., Sindelarova, K., Markova, J., and Guenther, A. B.: Global and regional impacts of land cover changes on isoprene emissions derived from spaceborne data and the MEGAN model, Atmospheric Chemistry and Physics, 21, 8413–8436, https://doi.org/10.5194/acp-21-8413-2021, 2021.

Ossohou, M., Hickman, J. E., Clarisse, L., Coheur, P.-F., Van Damme, M., Adon, M., Yoboué, V., Gardrat, E., Alvès, M. D., and Galy-Lacaux, C.: Trends and seasonal variability in ammonia across major biomes in western and central Africa inferred from long-term series of ground-based and satellite measurements, Atmospheric Chemistry and Physics, 23, 9473–9494, https://doi.org/10.5194/acp-23-9473-2023, 2023.

Ott, L. E., Pickering, K. E., Stenchikov, G. L., Allen, D. J., DeCaria, A. J., Ridley, B., Lin, R.-F., Lang, S., and Tao, W.-K.: Production of lightning NO and its vertical distribution calculated from three-dimensional cloud-scale chemical transport model simulations, Journal of Geophysical Research: Atmospheres, 115, https://doi.org/10.1029/2009JD011880, 2010.

Pacifico, F., Delon, C., Jambert, C., Durand, P., Morris, E., Evans, M. J., Lohou, F., Derrien, S., Donnou, V. H. E., Houeto, A. V., Reinares Martínez, I., and Brilouet, P.-E.: Measurements of nitric oxide and ammonia soil fluxes from a wet savanna ecosystem site in West Africa during the DACCIWA field campaign, Atmospheric Chemistry and Physics, 19, 2299–2325, https://doi.org/10.5194/acp-19-2299-2019, 2019.

Palmer, P. I., Jacob, D. J., Fiore, A. M., Martin, R. V., Chance, K., and Kurosu, T. P.: Mapping isoprene emissions over North America using formaldehyde column observations from space, Journal of Geophysical Research: Atmospheres, 108, https://doi.org/10.1029/2002JD002153, 2003.

Palmer, P. I., Abbot, D. S., Fu, T.-M., Jacob, D. J., Chance, K., Kurosu, T. P., Guenther, A., Wiedinmyer, C., Stanton, J. C., Pilling, M. J., Pressley, S. N., Lamb, B., and Sumner, A. L.: Quantifying the seasonal and interannual variability of North American isoprene emissions using satellite observations of the formaldehyde column, Journal of Geophysical Research: Atmospheres, 111, https://doi.org/10.1029/2005JD006689, 2006.

Pan, X., Ichoku, C., Chin, M., Bian, H., Darmenov, A., Colarco, P., Ellison, L., Kucsera, T., da Silva, A., Wang, J., Oda, T., and Cui, G.: Six global biomass burning emission datasets: intercomparison and application in one global aerosol model, Atmospheric Chemistry and Physics, 20, 969–994, https://doi.org/10.5194/acp-20-969-2020, 2020.

Parsons, D. A. B., Scholes, M. C., Scholes, R. J., and Levine, J. S.: Biogenic NO emissions from savanna soils as a function of fire regime, soil type, soil nitrogen, and water status, Journal of Geophysical Research: Atmospheres, 101, 23683–23688, https://doi.org/10.1029/95JD02140, 1996.

Passianoto, C. C., Ahrens, T., Feigl, B. J., Steudler, P. A., do Carmo, J. B., and Melillo, J. M.: Emissions of CO2, N2O, and NO in conventional and no-till management practices in Rondônia, Brazil, Biol Fertil Soils, 38, 200–208, https://doi.org/10.1007/s00374-003-0653-y, 2003.

Peeters, J., Nguyen, T. L., and Vereecken, L.: HOx radical regeneration in the oxidation of isoprene, Phys. Chem. Chem. Phys., 11, 5935–5939, https://doi.org/10.1039/B908511D, 2009.

Peeters, J., Müller, J.-F., Stavrakou, T., and Nguyen, V. S.: Hydroxyl Radical Recycling in Isoprene Oxidation Driven by Hydrogen Bonding and Hydrogen Tunneling: The Upgraded LIM1 Mechanism, J. Phys. Chem. A, 118, 8625–8643, https://doi.org/10.1021/jp5033146, 2014.

Pickering, K. E., Wang, Y., Tao, W.-K., Price, C., and Müller, J.-F.: Vertical distributions of lightning NOx for use in regional and global chemical transport models, Journal of Geophysical Research: Atmospheres, 103, 31203–31216, https://doi.org/10.1029/98JD02651, 1998.

Possell, M. and Hewitt, C. N.: Isoprene emissions from plants are mediated by atmospheric CO2 concentrations, Global Change Biology, 17, 1595–1610, https://doi.org/10.1111/j.1365-2486.2010.02306.x, 2011.

Price, C. and Rind, D.: A simple lightning parameterization for calculating global lightning distributions, Journal of Geophysical Research: Atmospheres, 97, 9919–9933, https://doi.org/10.1029/92JD00719, 1992.

Ramankutty, N., Evan, A. T., Monfreda, C., and Foley, J. A.: Farming the planet: 1. Geographic distribution of global agricultural lands in the year 2000, Global Biogeochemical Cycles, 22, https://doi.org/10.1029/2007GB002952, 2008.

Richter, D., Weibring, P., Walega, J. G., Fried, A., Spuler, S. M., and Taubman, M. S.: Compact highly sensitive multi-species airborne mid-IR spectrometer, Appl. Phys. B, 119, 119–131, https://doi.org/10.1007/s00340-015-6038-8, 2015.

Sanhueza, E., Cárdenas, L., Donoso, L., and Santana, M.: Effect of plowing on CO2, CO, CH4, N2O, and NO fluxes from tropical savannah soils, Journal of Geophysical Research: Atmospheres, 99, 16429–16434, https://doi.org/10.1029/94JD00265, 1994.

Schumann, U. and Huntrieser, H.: The global lightning-induced nitrogen oxides source, Atmospheric Chemistry and Physics, 7, 3823–3907, https://doi.org/10.5194/acp-7-3823-2007, 2007.

Serca, D., Delmas, R., Jambert, C., and Labroue, L.: Emissions of nitrogen oxides from equatorial rain forest in central Africa:, Tellus B, 46, 243–254, https://doi.org/10.1034/j.1600-0889.1994.t01-3-00001.x, 1994.

Serça, D., Delmas, R., Le Roux, X., Parsons, D. a. B., Scholes, M. C., Abbadie, L., Lensi, R., Ronce, O., and Labroue, L.: Comparison of nitrogen monoxide emissions from several African tropical ecosystems and influence of season and fire, Global Biogeochemical Cycles, 12, 637–651, https://doi.org/10.1029/98GB02737, 1998.

Sha, M. K., Langerock, B., Blavier, J.-F. L., Blumenstock, T., Borsdorff, T., Buschmann, M., Dehn, A., De Mazière, M., Deutscher, N. M., Feist, D. G., García, O. E., Griffith, D. W. T., Grutter, M., Hannigan, J. W., Hase, F., Heikkinen, P., Hermans, C., Iraci, L. T., Jeseck, P., Jones, N., Kivi, R., Kumps, N., Landgraf, J., Lorente, A., Mahieu, E., Makarova, M. V., Mellqvist, J., Metzger, J.-M., Morino, I., Nagahama, T., Notholt, J., Ohyama, H., Ortega, I., Palm, M., Petri, C., Pollard, D. F., Rettinger, M., Robinson, J., Roche, S., Roehl, C. M., Röhling, A. N., Rousogenous, C., Schneider, M., Shiomi, K., Smale, D., Stremme, W., Strong, K., Sussmann, R., Té, Y., Uchino, O., Velazco, V. A., Vigouroux, C., Vrekoussis, M., Wang, P., Warneke, T., Wizenberg, T., Wunch, D., Yamanouchi, S., Yang, Y., and Zhou, M.: Validation of methane and carbon monoxide from Sentinel-5 Precursor using TCCON and NDACC-IRWG stations, Atmospheric Measurement Techniques, 14, 6249–6304, https://doi.org/10.5194/amt-14-6249-2021, 2021.

Simpson, D. and Segers, A.: Transboundary particulate matter, photo-oxidants, acidifying and eutrophying components. EMEP Status Report 1/2024, The Norwegian Meteorological Institute, Oslo, Norway, 2024.

Simpson, D., Benedictow, A., and Darras, S.: The CAMS soil emissions: CAMS-GLOB-SOIL, in: CAMS2_61 – Global and European emission inventories., in: Documentation of CAMS emission inventory products, vol. Chap. 9, 59–70, 2023.

Sindelarova, K., Granier, C., Bouarar, I., Guenther, A., Tilmes, S., Stavrakou, T., Müller, J.-F., Kuhn, U., Stefani, P., and Knorr, W.: Global data set of biogenic VOC emissions calculated by the MEGAN model over the last 30 years, Atmospheric Chemistry and Physics, 14, 9317–9341, https://doi.org/10.5194/acp-14-9317-2014, 2014.

Sindelarova, K., Markova, J., Simpson, D., Huszar, P., Karlicky, J., Darras, S., and Granier, C.: High-resolution biogenic global emission inventory for the time period 2000–2019 for air quality modelling, Earth System Science Data, 14, 251–270, https://doi.org/10.5194/essd-14-251-2022, 2022.

Soulie, A., Granier, C., Darras, S., Zilbermann, N., Doumbia, T., Guevara, M., Jalkanen, J.-P., Keita, S., Liousse, C., Crippa, M., Guizzardi, D., Hoesly, R., and Smith, S. J.: Global anthropogenic emissions (CAMS-GLOB-ANT) for the Copernicus Atmosphere Monitoring Service simulations of air quality forecasts and reanalyses, 2024.

Souri, A. H., Nowlan, C. R., Wolfe, G. M., Lamsal, L. N., Chan Miller, C. E., Abad, G. G., Janz, S. J., Fried, A., Blake, D. R., Weinheimer, A. J., Diskin, G. S., Liu, X., and Chance, K.: Revisiting the effectiveness of HCHO/NO2 ratios for inferring ozone sensitivity to its precursors using high resolution airborne remote sensing observations in a high ozone episode during the KORUS-AQ campaign, Atmospheric Environment, 224, 117341, https://doi.org/10.1016/j.atmosenv.2020.117341, 2020.

Souri, A. H., González Abad, G., Wolfe, G. M., Verhoelst, T., Vigouroux, C., Pinardi, G., Compernolle, S., Langerock, B., Duncan, B. N., and Johnson, M. S.: Feasibility of robust estimates of ozone production rates using satellite observations, EGUsphere, 1–36, https://doi.org/10.5194/egusphere-2024-1947, 2024.

Stavrakou, T. and Müller, J.-F.: Grid-based versus big region approach for inverting CO emissions using Measurement of Pollution in the Troposphere (MOPITT) data, Journal of Geophysical Research: Atmospheres, 111, https://doi.org/10.1029/2005JD006896, 2006.

Stavrakou, T., Müller, J.-F., De Smedt, I., Van Roozendael, M., van der Werf, G. R., Giglio, L., and Guenther, A.: Global emissions of non-methane hydrocarbons deduced from SCIAMACHY formaldehyde columns through 2003–2006, Atmospheric Chemistry and Physics, 9, 3663–3679, https://doi.org/10.5194/acp-9-3663-2009, 2009.

Stavrakou, T., Müller, J.-F., Peeters, J., Razavi, A., Clarisse, L., Clerbaux, C., Coheur, P.-F., Hurtmans, D., De Mazière, M., Vigouroux, C., Deutscher, N. M., Griffith, D. W. T., Jones, N., and Paton-Walsh, C.: Satellite evidence for a large source of formic acid from boreal and tropical forests, Nature Geosci, 5, 26–30, https://doi.org/10.1038/ngeo1354, 2012.

Stavrakou, T., Müller, J.-F., Boersma, K. F., van der A, R. J., Kurokawa, J., Ohara, T., and Zhang, Q.: Key chemical NO_x sink uncertainties and how they influence top-down emissions of nitrogen oxides, Atmospheric Chemistry and Physics, 13, 9057–9082, https://doi.org/10.5194/acp-13-9057-2013, 2013.

Stavrakou, T., Müller, J.-F., Bauwens, M., De Smedt, I., Van Roozendael, M., De Mazière, M., Vigouroux, C., Hendrick, F., George, M., Clerbaux, C., Coheur, P.-F., and Guenther, A.: How consistent are top-down hydrocarbon emissions based on formaldehyde observations from GOME-2 and OMI?, Atmospheric Chemistry and Physics, 15, 11861–11884, https://doi.org/10.5194/acp-15-11861-2015, 2015.

Stavrakou, T., Müller, J.-F., Bauwens, M., De Smedt, I., Lerot, C., Van Roozendael, M., Coheur, P.-F., Clerbaux, C., Boersma, K. F., van der A, R., and Song, Y.: Substantial Underestimation of Post-Harvest Burning Emissions in the North China Plain Revealed by Multi-Species Space Observations, Sci Rep, 6, 32307, https://doi.org/10.1038/srep32307, 2016.

Stavrakou, T., Müller, J.-F., Bauwens, M., and De Smedt, I.: Sources and Long-Term Trends of Ozone Precursors to Asian Pollution, in: Air Pollution in Eastern Asia: An Integrated Perspective, edited by: Bouarar, I., Wang, X., and Brasseur, G. P., Springer International Publishing, Cham, 167–189, https://doi.org/10.1007/978-3-319-59489-7_8, 2017.

Stavrakou, T., Müller, J.-F., Bauwens, M., De Smedt, I., Van Roozendael, M., and Guenther, A.: Impact of Short-Term Climate Variability on Volatile Organic Compounds Emissions Assessed Using OMI Satellite Formaldehyde Observations, Geophysical Research Letters, 45, 8681–8689, https://doi.org/10.1029/2018GL078676, 2018.

Steinkamp, J. and Lawrence, M. G.: Improvement and evaluation of simulated global biogenic soil NO emissions in an AC-GCM, Atmospheric Chemistry and Physics, 11, 6063–6082, https://doi.org/10.5194/acp-11-6063-2011, 2011.

Varella, R., Bustamante, M., Pinto, A., Kisselle, K., Santos, R., Burke, R., Zepp, R., and Viana, L.: Soil fluxes of CO2, CO, NO, and N2O from an old pasture and from native Savanna in Brazil, Ecological Applications, 14, 221–231, https://doi.org/10.1890/01-6014, 2004.

Veldkamp, E., Keller, M., and Nuñez, M.: Effects of pasture management on N2O and NO emissions from soils in the humid tropics of Costa Rica, Global Biogeochemical Cycles, 12, 71–79, https://doi.org/10.1029/97GB02730, 1998.

Verhoelst, T., Compernolle, S., Pinardi, G., Lambert, J.-C., Eskes, H. J., Eichmann, K.-U., Fjæraa, A. M., Granville, J., Niemeijer, S., Cede, A., Tiefengraber, M., Hendrick, F., Pazmiño, A., Bais, A., Bazureau, A., Boersma, K. F., Bognar, K., Dehn, A., Donner, S., Elokhov, A., Gebetsberger, M., Goutail, F., Grutter de la Mora, M., Gruzdev, A., Gratsea, M., Hansen, G. H., Irie, H., Jepsen, N., Kanaya, Y., Karagkiozidis, D., Kivi, R., Kreher, K., Levelt, P. F., Liu, C., Müller, M., Navarro Comas, M., Piters, A. J. M., Pommereau, J.-P., Portafaix, T., Prados-Roman, C., Puentedura, O., Querel, R., Remmers, J., Richter, A., Rimmer, J., Rivera Cárdenas, C., Saavedra de Miguel, L., Sinyakov, V. P., Stremme, W., Strong, K., Van Roozendael, M., Veefkind, J. P., Wagner, T., Wittrock, F., Yela González, M., and Zehner, C.: Ground-based validation of the Copernicus Sentinel-5P TROPOMI NO_2 measurements with the NDACC ZSL-DOAS, MAX-DOAS and Pandonia global networks, Atmospheric Measurement Techniques, 14, 481–510, https://doi.org/10.5194/amt-14-481-2021, 2021.

Vigouroux, C., Hendrick, F., Stavrakou, T., Dils, B., De Smedt, I., Hermans, C., Merlaud, A., Scolas, F., Senten, C., Vanhaelewyn, G., Fally, S., Carleer, M., Metzger, J.-M., Müller, J.-F., Van Roozendael, M., and De Mazière, M.: Ground-based FTIR and MAX-DOAS observations of formaldehyde at Réunion Island and comparisons with satellite and model data, Atmospheric Chemistry and Physics, 9, 9523–9544, https://doi.org/10.5194/acp-9-9523-2009, 2009.

Vigouroux, C., Bauer Aquino, C. A., Bauwens, M., Becker, C., Blumenstock, T., De Mazière, M., García, O., Grutter, M., Guarin, C., Hannigan, J., Hase, F., Jones, N., Kivi, R., Koshelev, D., Langerock, B., Lutsch, E., Makarova, M., Metzger, J.-M., Müller, J.-F., Notholt, J., Ortega, I., Palm, M., Paton-Walsh, C., Poberovskii, A., Rettinger, M., Robinson, J., Smale, D., Stavrakou, T., Stremme, W., Strong, K., Sussmann, R., Té, Y., and Toon, G.: NDACC harmonized formaldehyde time series from 21 FTIR stations covering a wide range of column abundances, Atmospheric Measurement Techniques, 11, 5049–5073, https://doi.org/10.5194/amt-11-5049-2018, 2018.

Vigouroux, C., Langerock, B., Bauer Aquino, C. A., Blumenstock, T., Cheng, Z., De Mazière, M., De Smedt, I., Grutter, M., Hannigan, J. W., Jones, N., Kivi, R., Loyola, D., Lutsch, E., Mahieu, E., Makarova, M., Metzger, J.-M., Morino, I., Murata, I., Nagahama, T., Notholt, J., Ortega, I., Palm, M., Pinardi, G., Röhling, A., Smale, D., Stremme, W., Strong, K., Sussmann, R., Té, Y., van Roozendael, M., Wang, P., and Winkler, H.: TROPOMI–Sentinel-5 Precursor formaldehyde validation using an extensive network of ground-based Fourier-transform infrared stations, Atmospheric Measurement Techniques, 13, 3751–3767, https://doi.org/10.5194/amt-13-3751-2020, 2020.

Vinken, G. C. M., Boersma, K. F., Maasakkers, J. D., Adon, M., and Martin, R. V.: Worldwide biogenic soil NO_x emissions inferred from OMI NO₂ observations, Atmos. Chem. Phys., 14, 10363–10381, https://doi.org/10.5194/acp-14-10363-2014, 2014.

Wang, H., Liu, X., Wu, C., and Lin, G.: Regional to global distributions, trends, and drivers of biogenic volatile organic compound emission from 2001 to 2020, Atmospheric Chemistry and Physics, 24, 3309–3328, https://doi.org/10.5194/acp-24-3309-2024, 2024.

Weibring, P., Richter, D., Walega, J. G., and Fried, A.: First demonstration of a high performance difference frequency spectrometer on airborne platforms, Opt. Express, OE, 15, 13476–13495, https://doi.org/10.1364/OE.15.013476, 2007.

Weitz, A. M., Veldkamp, E., Keller, M., Neff, J., and Crill, P. M.: Nitrous oxide, nitric oxide, and methane fluxes from soils following clearing and burning of tropical secondary forest, Journal of Geophysical Research: Atmospheres, 103, 28047–28058, https://doi.org/10.1029/98JD02144, 1998.

Wells, K. C., Millet, D. B., Payne, V. H., Deventer, M. J., Bates, K. H., de Gouw, J. A., Graus, M., Warneke, C., Wisthaler, A., and Fuentes, J. D.: Satellite isoprene retrievals constrain emissions and atmospheric oxidation, Nature, 585, 225–233, https://doi.org/10.1038/s41586-020-2664-3, 2020.

Wells, K. C., Millet, D. B., Payne, V. H., Vigouroux, C., Aquino, C. a. B., De Mazière, M., de Gouw, J. A., Graus, M., Kurosu, T., Warneke, C., and Wisthaler, A.: Next-Generation Isoprene Measurements From Space: Detecting Daily Variability at High Resolution, Journal of Geophysical Research: Atmospheres, 127, e2021JD036181, https://doi.org/10.1029/2021JD036181, 2022.

Weng, H., Lin, J., Martin, R., Millet, D. B., Jaeglé, L., Ridley, D., Keller, C., Li, C., Du, M., and Meng, J.: Global high-resolution emissions of soil NO x , sea salt aerosols, and biogenic volatile organic compounds, Scientific Data, 7, 148, https://doi.org/10.1038/s41597-020-0488-5, 2020.

van der Werf, G. R., Randerson, J. T., Giglio, L., van Leeuwen, T. T., Chen, Y., Rogers, B. M., Mu, M., van Marle, M. J. E., Morton, D. C., Collatz, G. J., Yokelson, R. J., and Kasibhatla, P. S.: Global fire emissions estimates during 1997–2016, Earth System Science Data, 9, 697–720, https://doi.org/10.5194/essd-9-697-2017, 2017.

Wolf, K., Veldkamp, E., Homeier, J., and Martinson, G.: Nitrogen availability links forest productivity, soil nitrous oxide and nitric oxide fluxes of a tropical montane forest in Southern Ecuador, Global Biogeochemical Cycles, 25, GB4009, https://doi.org/10.1029/2010GB003876, 2011.

Wolfe, G. M., Kaiser, J., Hanisco, T. F., Keutsch, F. N., de Gouw, J. A., Gilman, J. B., Graus, M., Hatch, C. D., Holloway, J., Horowitz, L. W., Lee, B. H., Lerner, B. M., Lopez-Hilifiker, F., Mao, J., Marvin, M. R., Peischl, J., Pollack, I. B., Roberts, J. M., Ryerson, T. B., Thornton, J. A., Veres, P. R., and Warneke, C.: Formaldehyde production from isoprene oxidation across NOx regimes, Atmos Chem Phys, 16, 2597–2610, https://doi.org/10.5194/acp-16-2597-2016, 2016.

Yan, X., Ohara, T., and Akimoto, H.: Statistical modeling of global soil NOx emissions, Global Biogeochemical Cycles, 19, https://doi.org/10.1029/2004GB002276, 2005.

Yáñez-Serrano, A. M., Bourtsoukidis, E., Alves, E. G., Bauwens, M., Stavrakou, T., Llusià, J., Filella, I., Guenther, A., Williams, J., Artaxo, P., Sindelarova, K., Doubalova, J., Kesselmeier, J., and Peñuelas, J.: Amazonian biogenic volatile organic compounds under global change, Global Change Biology, 26, 4722–4751, https://doi.org/10.1111/gcb.15185, 2020.

Yienger, J. J. and Levy, H.: Empirical model of global soil-biogenic NOχ emissions, Journal of Geophysical Research: Atmospheres, 100, 11447–11464, https://doi.org/10.1029/95JD00370, 1995.

Yuan, H., Dai, Y., Xiao, Z., Ji, D., and Shangguan, W.: Reprocessing the MODIS Leaf Area Index products for land surface and climate modelling, Remote Sensing of Environment, 115, 1171–1187, https://doi.org/10.1016/j.rse.2011.01.001, 2011.

Zhu, L., Jacob, D. J., Mickley, L. J., Marais, E. A., Cohan, D. S., Yoshida, Y., Duncan, B. N., Abad, G. G., and Chance, K. V.: Anthropogenic emissions of highly reactive volatile organic compounds in eastern Texas inferred from oversampling of satellite (OMI) measurements of HCHO columns, Environ. Res. Lett., 9, 114004, https://doi.org/10.1088/1748-9326/9/11/114004, 2014.

Zhu, L., Jacob, D. J., Kim, P. S., Fisher, J. A., Yu, K., Travis, K. R., Mickley, L. J., Yantosca, R. M., Sulprizio, M. P., De Smedt, I., González Abad, G., Chance, K., Li, C., Ferrare, R., Fried, A., Hair, J. W., Hanisco, T. F., Richter, D., Jo Scarino, A., Walega, J., Weibring, P., and Wolfe, G. M.: Observing atmospheric formaldehyde (HCHO) from space: validation and intercomparison of six retrievals from four satellites (OMI, GOME2A, GOME2B, OMPS) with SEAC^{4}RS aircraft observations over the southeast US, Atmospheric Chemistry and Physics, 16, 13477–13490, https://doi.org/10.5194/acp-16-13477-2016, 2016.

Zhu, L., González Abad, G., Nowlan, C. R., Chan Miller, C., Chance, K., Apel, E. C., DiGangi, J. P., Fried, A., Hanisco, T. F., Hornbrook, R. S., Hu, L., Kaiser, J., Keutsch, F. N., Permar, W., St. Clair, J. M., and Wolfe, G. M.: Validation of satellite formaldehyde (HCHO) retrievals using observations from 12 aircraft campaigns, Atmospheric Chemistry and Physics, 20, 12329–12345, https://doi.org/10.5194/acp-20-12329-2020, 2020.

Ziemke, J. R., Chandra, S., and Bhartia, P. K.: “Cloud slicing”: A new technique to derive upper tropospheric ozone from satellite measurements, Journal of Geophysical Research: Atmospheres, 106, 9853–9867, https://doi.org/10.1029/2000JD900768, 2001.

ANNEXES

Table S1: *Compilation of in situ flux measurements of soil NO in Africa from the literature. The mean fluxes are given in 10^{10} molec.cm^{-2} s^{-1}, with distinction between the dry (D) and wet (W) season. Also given is the type of biome at the measurement site: savannah (S), forest (F) or mixed (M). Notes: (a) average of forests and/or savannah ecosystems mean fluxes weighted by the number of individual chamber measurements, (b) arithmetic average over three unburned sites, (c) arithmetic average of uncorrected NO fluxes at dry control sites of Shabeni 6 and Kambeni 1, and (d) arithmetic average of measurements over grasslands, forests, fertilised and unfertilised crops and fallow fields.*

	Location	Lon.	Lat.	Mean Flux	Month	Season	Biome	Reference
1	Mayombe, Congo	12.50°E	4.50°S	1.74	6	W	F	Serça et al. (1994)
				0.78	7	D		
				0.50	2	W		
2	Teke Plateau, Congo	12.45°E	4.2°S	0.03	4	W	S	Serça et al. (1998)
3	Lamto, Ivory Coast	5.03°W	6.22°N	1.02[a]	1	D	M	Le Roux et al. (1995)
				0.74[a]	5	W		Serça et al. (1998)
4	Nylsvley, South Africa	22.42°E	30.83°S	2.98[a]	3	W	S	Serça et al. (1998)
5	Krüger N.P., South Africa	22.42°E	30.83°S	0.97[b]	10	W	S	Parsons et al. (1996)
				2.13[b]	11	W		
				1.01[b]	12	W		
				3.17[a]	8	D		Serça et al. (1998)
6	Transvaal, South Africa	22.42°E	30.53°S	1.99[c]	9	D	S	Levine et al. (1996)
7	Marondera, Zimbabwe	31.74°E	18.18°S	4.85[d]	10-12	W	S	Meixner et al. (1997)
8	Savè, Benin	2.49°E	8.03°N	2.06	6-7	W	S	Pacifico et al. (2019)
9	Banizoumbou, Niger	2.40°E	13.30°N	2.62	8	W	S	Le Roux et al. (1995)
10	Agoufou, Mali	1.48°W	15.34°N	2.88	7	W	S	Delon et al. (2015)
				0.98	8	W	S	
11	Dahra, Senegal	15.43°W	15.40°N	2.45	7	W	S	Delon et al. (2017, 2019)
				1.72	11	D		

Table S2: *Compilation of reported in situ flux measurements of soil NO (in 10^{10} molec.cm^{-2}s^{-1}) in South America. The data are separated between the dry (D) and wet (W) season, or annual (A). The biome type at the measurement site is forest (F), pasture (P), savanna (S) or mixed (M). Explanatory notes are provided at the end of the table.*

	Location	Lon. (W)	Lat.	Mean Flux	Month	Season	Biome	Reference
1	Park 1, Brazil	47.53°	2.98°S	1.00[a]	6	W	F	Cattânio et al. (2002)
				1.28[a]	7	D	F	
				0.62[a]	8	D	F	
				1.74[a]	9	D	F	
				6.37[a]	10	D	F	
				3.57[a]	11	D	F	
				4.61[a]	12	W	F	
2	Park 2, Brazil	54.95°	3.04°S	5.97[b]	1-6	W	F	Keller et al. (2005)
				14.21[b]	7-12	D	F	
				10.11[b]	1-12	A	F	
3	Rondônia, Brazil	62.50°	10.50°S	1.17[c]	10	W		Carmo et al. (2007)
				0.68[d]	2-3	W	F	Garcia-Montiel et al. (2001)
				0.79[d]	8-9	D	F	
				0.43[d]	3	W	F	
4	Adolfo Ducke Forest Reserve (RFAD), Manaus, Brazil	60.02°	3.10°S	5.23	7-8	D	F	Kaplan et al. (1988)
				1.71[e]	4-5	W	F	Bakwin et al. (1990)
5	Tapajos, Brazil	54.95°	2.90°S	0.99[f]	2	W	F	Davidson et al. (2008)
				1.28[f]	3	W		
				0.37[f]	4	W		
				0.23[f]	5	W		
				1.42[f]	6	W		
				0.38[f]	7	D		
				1.94[f]	8	D		
				3.16[f]	9	D		
				3.63[f]	10	D		
				2.68[f]	11	D		
				3.03[f]	12	D		
6	Instituto Brasileiro de Geografia e Estatica (IGBE), Brazil	47.85°	15.93°S	0.64[g]	7	D	S	Varella et al. (2004)
				1.17[g]	8	D		
				0.68[g]	9	D		
				0.61[g]	10	W		
				0.83[g]	2	W		
				0.44[g]	3	W		
				0.27[g]	4	W		
				1.22[g]	5	D		
				0.16[g]	6	D		
7	Empresa Brasileira de	47.75°	15.65°S	1.11[g]	7	D	P	Varella et al. (2004)
				0.55[g]	8	D		

	Pesquisa Agropecuaria (EMPRAPA), Brazil			0.49[g]	10	W		
				0.33[g]	2	W		
				0.01[g]	3	W		
				0.19[g]	4	W		
				0.10[g]	5	D		
				0.09[g]	6	D		
8	Chaguaramas, Venezuela	66.25°	9.38°N	3.12[h]	10	W	S	Johansson and Sanhueza (1988)
				3.40[i]	2	D	S	Johansson et al. (1988)
9	Calabozo, Venezuela	67.32°	8.88°N	5.29[j]	5-6	W	S	Sanhueza et al. (1994)
10	La Selva, Costa Rica	84.00°	10.43°N	1.07[k]	1-12	A	M	Keller and Reiners (1994); Weitz et al., (1998)
11	Horquetas, Costa Rica	84.92°	10.03°N	3.42[l]	1	D	P	Veldkamp et al. (1998)
				3.60[l]	2	D		
				2.62[l]	3	D		
				2.65[l]	5	W		
				1.44[l]	6	W		
				1.29[l]	7	W		
				1.82[l]	8	W		
				6.45[l]	9	W		
				3.17[l]	10	W		
				2.31[l]	11	W		
				3.23[l]	12	W		
12	Podocarpus National Park (PNP), Ecuador	79°	4.00°S	0.12[m]	1-12	A	F	Wolf et al. (2011)
13	Gigante Peninsula, Panama	79.98°	9.10°N	0.37[n]	1-12	A	F	Koehler et al. (2009)
14	Fortuna Forest, Panama	82.25°	8.75°N	0.18[n]	1-12	A	F	Koehler et al. (2009)

Notes: (a) Monthly mean value of the control treatment; (b) Arithmetic average of undisturbed forest sites for clay and sandy loam in 2000 and 2001; (c) Arithmetic average from the control experiment (Carmo et al., 2007; Fig. 4a); (d) Arithmetic average over the seven sites i.e., one forest and six pastures or less if data was not available (Garcia-Montiel et al., 2001, Fig. 2); (e) Weighted average for clay and sandy soils; (f) Arithmetic average over the five years from the control treatment (Davidson et al., 2008, Fig. 2); (g) Arithmetic average for the pasture and Cerrado (Varella et al., 2004, Fig. 4); (h) Weighted average calculated based on site 1 (Johansson and Sanhueza, 1988, Table 2). In site 2, the occurrence of a heavy rain episode triggered very high emissions on October 28; (i) Median fluxes calculated based on the six studied savanna plots; (j) Fluxes from unplowed savanna. Model estimates are calculated based on the average of two grid cells (8.75°N, 67.25°W) and (9.25°N,67.32°W) because of the site coordinates are found in between and estimates exhibit large disparity; (k) Similar annual averages in both references. For Keller and Reiners (1994), arithmetic average was calculated for the forest and pasture sites (Keller and Reiners, 1994, Tab. 3); (l) Arithmetic averages are calculated based on the three pastures (Veldkamp et al., 1998, Fig 1b); (m) Arithmetic average over two elevations (1000 and 2000 m) and topographic positions (lower- and mid-slope). Measurements at 3000 m and at ridges are not considered in the comparisons. Model estimates are averaged over the two grid cells: (4.1°S, 78.97°W) and (3.97°S, 79.07°W) for the 1000 m and 2000 m sites; (n) Arithmetic average over 2006-2007 for the control treatment.